Physics Area - Ph.D. course in
Theory and Numerical Simulation of Condensed Matter

ADVANCES IN LATTICE THERMAL TRANSPORT IN CRYSTALS AND GLASSES

Candidate:
Alfredo Fiorentino

Supervisor:
Prof. Stefano Baroni

Academic year 2023/2024

Alfredo Fiorentino: *Advances in Lattice Thermal Transport in Crystals and Glasses,* Ph.D. Defense, December 2024

ABSTRACT

Thermal conductivity is a fundamental property for describing the non-equilibrium phenomenon of thermal transport. In solid insulators, whether disordered or crystalline, heat is primarily carried by lattice vibrations, emphasizing the need to accurately understand and compute the *lattice thermal conductivity*. This computation remains a central challenge in condensed matter physics, and lattice dynamical approaches have long been favored for this purpose. Despite being limited to (quasi-) harmonic dynamics, these methods can address key challenges in Molecular Dynamics, such as incorporating nuclear quantum effects and avoiding the sampling problems.

Historically, separate lattice dynamical approaches were applied to glasses and crystals, creating a division in the field. However, recent advances, such as the development of unified frameworks like the Quasi-Harmonic Green-Kubo theory, have revolutionized the study of lattice thermal conductivity. This theory, derived by solving the Green-Kubo expression in the quasi-harmonic regime, provides a common theoretical framework for modeling heat transport across both ordered and disordered systems. Nevertheless, simplifying assumptions and computational scaling issues have limited its broad application.

This thesis addresses these challenges through two main advancements. First, the theory is extended beyond the single-mode relaxation time approximation, enabling the accurate modeling of the low-temperature thermal conductivity of crystals. Second, the computational limitations, particularly relevant for glasses, are mitigated by combining hydrodynamic insights with efficient algorithms to achieve the bulk limit. This investigation of the bulk limit not only provides a quantitative correction but also reveals new insights into the behavior of glasses, highlighting the critical role of anharmonicity. While the inclusion of anharmonicity hardly brings significant changes to the thermal conductivity of typical glass samples containing only a few thousand atoms, the harmonic model typically exhibits a singular behavior in the bulk limit, which is then regularized by anharmonic effects.

The ability to compute lattice thermal conductivity in large disordered systems is essential for designing materials with impactful applications. The theoretical and numerical tools developed here have been applied to spatially correlated silicon-germanium alloys, studied from first principles. These results suggest that correlated disorder may significantly enhance thermoelectric efficiency compared to standard SiGe alloys, highlighting the potential of these materials for thermoelectric applications.

PUBLICATIONS

This Thesis is based on the following publications:

1. Alfredo Fiorentino and Stefano Baroni. "From Green-Kubo to the full Boltzmann kinetic approach to heat transport in crystals and glasses." In: *Phys. Rev. B* 107 (5 2023), p. 054311. DOI: 10.1103/PhysRevB.107.054311.

   We extend the Quasi-Harmonic Green-Kubo formula beyond the relaxation time approximation, leading to a generalization of the conductivity expression derived from the linearized Boltzmann equation when the full scattering matrix is accounted for. This work connects two recently proposed unified approaches to heat transport in insulating crystals and glasses.

2. Alfredo Fiorentino, Paolo Pegolo, and Stefano Baroni. "Hydrodynamic finite-size scaling of the thermal conductivity in glasses." In: *npj Computational Materials* 9.1 (2023). ISSN: 2057-3960. DOI: 10.1038/s41524-023-01116-2.

   Estimating the thermal conductivity of glasses via the Quasi-Harmonic Green-Kubo theory is computationally demanding due to its poor scaling with system size. Leveraging hydrodynamic arguments, we propose a simple formula to extrapolate reliable bulk thermal conductivity estimates from finite glass models of moderate size.

3. Alfredo Fiorentino, Enrico Drigo, Stefano Baroni, and Paolo Pegolo. "Unearthing the foundational role of anharmonicity in heat transport in glasses." In: *Physical Review B* 109.22 (2024), p. 224202. DOI: 10.1103/PhysRevB.109.224202.

   Under the general assumption of Rayleigh-like disorder scattering, harmonic theories of heat transport in glasses fail in the bulk limit, predicting a diverging thermal conductivity. The presence of Rayleigh scattering is numerically investigated in three paradigmatic glasses, highlighting the crucial regularizing effect of anharmonicity.

4. Alfredo Fiorentino, Paolo Pegolo, Stefano Baroni, and Davide Donadio. "Effects of colored disorder on the heat conductivity of SiGe alloys from first principles." In: *arXiv preprint arXiv:2408.05155* (2024). URL: https://arxiv.org/abs/2408.05155.

   The thermal conductivity of spatially correlated silicon-germanium alloys is studied from first principles. Our findings indicate up to

a fourfold enhancement in the thermoelectric figure of merit compared to alloys with uncorrelated disorder.

CONTENTS

ACRONYMS

GK Green-Kubo

LTE Local Thermal Equilibrium

BO Born-Oppenheimer

MD Molecular Dynamics

DFT Density Functional Theory

QH Quasi-Harmonic

QHGK Quasi-Harmonic Green-Kubo

BTE linearized Peierls-Boltzmann Transport Equation

WBTE Wigner-Boltzmann Transport Equation

MBPT Many-Body Perturbation Theory

AF Allen-Feldman

RTA Relaxation Time Approximation

BTE-RTA linearized Peierls-Boltzmann Transport Equation in the Relaxation Time Approximation

Full-BTE Full solution of the linearized Peierls-Boltzmann Transport Equation

MZ Mori-Zwanzig memory-function

GKMZ Green-Kubo Mori-Zwanzig

SM Single-Mode

FGR Fermi's Golden Rule

IFC Interatomic Force Constants

PBCs Periodic Boundary Conditions

BZ Brillouin Zone

FLT Fourier-Laplace transform

FT Fourier transform

VDOS Vibrational Density of States

VDSF Vibrational Dynamical Structure Factor

GKMD Green-Kubo Molecular Dynamics

TE Thermoelectric

eVCA electronic Virtual Crystal Approximation

vVCA vibrational Virtual Crystal Approximation

MLPs Machine Learning Potentials

DFPT Density Functional Perturbation Theory

IPR Inverse Participation Ratio

If I have seen further it is by standing on the shoulders of Giants.

— Isaac Newton —

INTRODUCTION

Thermal transport is a non-equilibrium phenomenon, closely tied to fundamental physical principles, such as the second law of thermodynamics, and is essential in a wide range of technological applications. Encompassing thermal insulation of habitations, thermal management of electrochemical and electronic devices, and thermoelectric conversion for powering space probes, the study of thermal transport is crucial across various fields.

Thermal conductivity is the transport coefficient that relates, in the absence of convective processes, the system's response to a weak thermal inhomogeneity. Under these hypotheses, thermal transport is described by Fourier's law, which for an isotropic medium reads:

$$\mathbf{J} = -\kappa \nabla T,$$

where $\mathbf{J}$ is the heat current, ∇T is the temperature gradient, and κ is the *thermal conductivity*.

In typical solid insulators and semiconductors, heat transport primarily occurs via atomic vibrations near equilibrium positions. In these materials, the *lattice thermal conductivity* constitutes a significant, if not the dominant, contribution to the overall thermal conductivity.

Far from melting, atomic displacements from equilibrium are much smaller than interatomic distances, making their dynamics well-suited for lattice dynamical approaches. These involve numerically solving the equations of motion derived from a Taylor expansion of the Born-Oppenheimer potential, assuming the dominance of the second-order *harmonic* term. Despite atomic vibrations being present in both disordered and ordered systems, lattice dynamical approaches have distinguished between these two classes of systems for a long time. Until recent years, the two primary, yet distinct, lattice dynamics methods, lattice dynamics methods to compute thermal conductivity were the linearized Peierls-Boltzmann Transport Equation (BTE) and the Allen-Feldman (AF) approach, respectively for crystals and disordered systems like glasses. The former approach, commonly used also for charge transport, is a semi-classical treatment that requires a quasi-particle framework for the heat carriers. The periodicity of the crystal plays a fundamental role in its applicability, as it allows one to associate a (crystal) momentum to the eigenstates of the harmonic Hamiltonian, the *phonons* quasi-particles. On the other hand, the latter method does not assume any periodicity for the system. However, as a purely harmonic theory, it can yield a diverging thermal conductivity. This issue is particularly evident for crystals,

where, in the absence of anharmonic scattering, phonons with non-zero group velocity propagate ballistically. Even for glasses, a harmonic model can prove inadequate. While it may produce finite results for finite samples, under general assumptions, a harmonic theory of heat transport in glasses exhibits a singular behavior in the bulk limit.

In recent years, two unified approaches have been proposed: the Quasi-Harmonic Green-Kubo (QHGK) method and the Wigner-Boltzmann Transport Equation (WBTE), the former being the solution of the Green-Kubo formula in the quasi-harmonic regime, while the latter being the generalization through Wigner transformations of the BTE. Despite their different origin, these two quantitatively equivalent approaches bridge and extend the two previously separated methods, developing a unified framework for both disordered and ordered solids. The QHGK method plays a fundamental role in this thesis, as the main focus of the author during the Ph.D. course has been the theoretical and numerical development of such method, although most of the results could be straightforwardly extended to WBTE.

The thesis is organized as follows. Ch. 1 provides a brief summary of the theory of transport processes, focusing on the Green-Kubo theory of linear response for calculating transport coefficients and the recently formulated invariance principles of these coefficients. Then, Ch. 2 revisits the derivation of the QHGK formula in both its original and extended forms. The extended version, which describes the dynamics of lattice vibrations beyond the typical single-mode relaxation time approximation, is essential for capturing the properties of crystals at low temperatures and further clarifies the interconnection between the Boltzmann and Green-Kubo approaches, as exemplified by studying the antiperovskite Li_3ClO.

Ch. 3 addresses the challenging problem of evaluating the bulk limit of the thermal conductivity of glasses. This problem is approached by leveraging hydrodynamic arguments along with efficient algorithms. This chapter includes a critical analysis of the differences in the bulk limits of the AF and QHGK thermal conductivities, with particular emphasis on the often underestimated divergence of the Allen-Feldman method. Many of the tools developed in Ch. 3 are applied in Ch. 4, where, in the pursuit of devising enhanced thermoelectric devices, the thermal conductivity of spatially correlated silicon-germanium alloys is studied from first principles. Finally, Ch. 5 presents the conclusions.

If someone points out to you that your pet theory of the universe is in disagreement with Maxwell's equations—then so much the worse for Maxwell's equations. If it is found to be contradicted by observation—well, these experimentalists do bungle things sometimes. But if your theory is found to be against the second law of thermodynamics I can give you no hope; there is nothing for it but to collapse in deepest humiliation.

— Arthur Eddington, The Nature of the Physical World (1928) —

1

LINEAR-RESPONSE THEORY OF TRANSPORT PROCESSES

Transport theory describes the response of a macroscopic current to a thermodynamic force, representing one of the most fundamental mechanisms of entropy production and a key manifestation of the arrow of time: "Heat flows from a higher to a lower temperature as time flows from the past to the future". This chapter introduces the theoretical framework for understanding transport phenomena in macroscopic systems. The Green-Kubo linear-response theory is detailed, covering both classical and quantum regimes, and its application to thermal transport is explored. Invariance principles for transport coefficients, including gauge invariance and their application to multi-component systems, are thoroughly analyzed.

1.1 EXTENSIVE VARIABLES AND LOCAL THERMAL EQUILIBRIUM

Transport phenomena involve conserved extensive variables $\{A\}$ and their conjugate intensive variables, defined through the microcanonical entropy $\alpha = \frac{\partial S}{\partial A}$. For instance, if the set of extensive variables consists of $A = E, V, N_i$, representing energy, volume, and the number of molecules of species i, respectively, then the corresponding intensive variables are $\alpha = \{\frac{1}{T}, \frac{p}{T}, -\frac{\mu_i}{T}\}$, where T is the temperature, p the pressure, and μ_i the chemical potential of the i-th species. At thermodynamic equilibrium, the intensive variables are spatially uniform. This can be demonstrated by maximizing the entropy at equilibrium and using the additivity of extensive variables. Consider an isolated system decomposed into two arbitrary subsystems with volumes V_1 and V_2. Maximizing the total entropy with respect to A_1 under the constraint of $A = A_1 + A_2$ yields:

$$\frac{\partial S}{\partial A_1} = \frac{\partial S(A_1, V_1)}{\partial A_1} + \frac{\partial S(A - A_1, V_2)}{\partial A_1} \qquad = \alpha_1 - \alpha_2 \ = 0,$$

which implies that at equilibrium, $\alpha_1 = \alpha_2 = \alpha$. Since the choice of subsystem division is arbitrary, it follows that α must be homogeneous throughout the system.

On the other hand, if the intensive variables are not homogeneous there is a flow of the extensive quantities to restore the equilibrium. Let us consider a partition of the system of volume V into n subvolumes $\{V_1, \dots, V_n\}$. Then, the rate of entropy change is:

$$\begin{aligned} \dot{S}(V,t) &= \sum_i \frac{\partial S}{A_i} \dot{A}_i \\ &= \sum_i \alpha_i \dot{A}_i \\ &\geqslant 0 \end{aligned} \tag{1.1}$$

where the last line is a reminder of the second principle of thermodynamics. Let us take the continuous limit. Due to their additivity, it is natural to define the density of the extensive quantities:

$$A = \int_V d\mathbf{r}\ a(\mathbf{r}).$$

Moreover, in a framework of Local Thermal Equilibrium (LTE) where each position $\mathbf{r}$ indicates a subsystem that locally satisfies an equation of state, the local value of the intensive variable can be meaningfully defined: $\alpha(\mathbf{r})$. Then, Eq. (1.1) in the continuous limit becomes:

$$\dot{S}(V,t) = \int d\mathbf{r}\ \alpha(\mathbf{r},t)\dot{a}(\mathbf{r},t) \tag{1.2}$$

Furthermore, if the extensive quantity is locally conserved, it means its *conserved density* satisfies a continuity equation:

$$\dot{a}(\mathbf{r},t) + \nabla \cdot \mathbf{j}(\mathbf{r},t) = 0 \tag{1.3}$$

where $\langle\cdot\rangle$ is the time derivative and j is the associated *conserved current*. Substituting Eq. (1.3) into Eq. (1.2), yields to

$$\begin{aligned} \dot{S}(V,t) &= -\int d\mathbf{r}\ \alpha(\mathbf{r},t)\nabla \cdot \mathbf{j}(\mathbf{r},t) \\ &= \int d\mathbf{r}\ \nabla\alpha(\mathbf{r},t)\mathbf{j}(\mathbf{r},t) \end{aligned}$$

where the integration by parts has been used. The above expression can be further simplified in the linear response regime, where $|\nabla\alpha|$ is small and weakly depends on space. Indeed, as explained in detail below, in such conditions the following relation holds:

$$\mathbf{J} = \sigma\mathbf{F},$$

where σ defines a transport coefficient, and $J = \frac{1}{V}\int d\mathbf{r}\ \mathbf{j}(\mathbf{r})$ and $F = \frac{1}{V}\int d\mathbf{r}\ \nabla\alpha(\mathbf{r})$ are respectively the *conserved flux* (macroscopic average of the conserved current) and the *thermodynamic force*. It is worth noticing that, if the process is irreversible and the production of entropy must be positive, then $\sigma > 0$. Indeed, heat goes spontaneously from warm to cool.

1.2 HYDRODYNAMIC VARIABLES

To understand the linearity between conserved fluxes and thermodynamic forces, and their decoupling from other local degrees of freedom, the continuity equation plays a fundamental role.

The continuity equation shows that the time derivative of an extensive variable is a surface term, which becomes negligible for a large enough volume. Indeed, applying a spatial Fourier transform (FT), the continuity equation yields

$$\dot{\tilde{a}}(\mathbf{k}, t) = -i\mathbf{k} \cdot \tilde{j}_a(\mathbf{k}, t), \tag{1.4}$$

where the FT is defined as $\tilde{f}(\mathbf{k}) = \int d\mathbf{r}\ f(\mathbf{r}) e^{-i\mathbf{k}\cdot\mathbf{r}}$, and $\mathbf{k} \sim \frac{2\pi}{\lambda}, \lambda$ are the wavevector and wavelength, respectively. Eq. (1.4) shows that for sufficiently large wavelengths, $\dot{\tilde{a}}(\mathbf{k}, t)$ approaches zero, assuming $\tilde{j}_a(\mathbf{k}, t)$ is bounded. Therefore, *hydrodynamic variables* ($\mathbf{k} \to 0$) are adiabatically decoupled from the dynamics of the (zillions of) fast atomic degrees of freedom.

Let us consider a system with M conserved densities. For instance, in a one-component fluid, the number of conserved quantities is 5: mass (or particle number), energy, and the three components of momentum. Without loss of generality, let us set to zero the equilibrium value of the conserved densities, therefore $\tilde{a}_j(\mathbf{k}, \omega)$ already indicates the deviation from equilibrium. Due to the mentioned decoupling, it can be assumed that, to first order, the time derivative of conserved densities involves only deviations from the equilibrium of conserved densities. Moreover, in a macroscopically homogeneous material, different $\mathbf{k}$ components are independent of each other. In the domain of a space and time FT ($\tilde{f}(\mathbf{k}, \omega) = \int d\mathbf{r}\ f(\mathbf{r}, t) e^{i(\omega t - \mathbf{k}\cdot\mathbf{r})}$), this reads:

$$-i\omega \tilde{a}_i(\mathbf{k}, \omega) = \sum_j \tilde{\Lambda}_{ij}(\mathbf{k}, \omega) \tilde{a}_j(\mathbf{k}, \omega),$$

where $\tilde{\Lambda}_{ij}(\mathbf{k}, \omega)$ are suitable defined coefficients. Combining this equation with the space-time FT of the continuity equation

$$-i\omega \tilde{a}_i(\mathbf{k}, \omega) = -i\mathbf{k} \cdot \tilde{j}_i(\mathbf{k}, \omega),$$

one finds the *constitutive equations*:

$$-i\mathbf{k} \cdot \tilde{j}_i(\mathbf{k}, \omega) = \sum_j \tilde{\Lambda}_{ij}(\mathbf{k}, \omega) \tilde{a}_j(\mathbf{k}, \omega).$$

Assuming that the conserved currents are chosen irrotational, the following equation holds:

$$\tilde{j}_i(\mathbf{k}, \omega) = \frac{i\mathbf{k}}{k^2} \sum_j \tilde{\Lambda}_{ij}(\mathbf{k}, \omega) \tilde{a}_j(\mathbf{k}, \omega)$$

In isotropic media, $\tilde{\Lambda}_{ij}$ are spherically symmetric functions of $\mathbf{k}$, and their $\mathbf{k} = (0, 0, 0)$ value is null because a non-vanishing value would imply a non-physical long-range correlation between conserved densities,

which would contradict LTE assumptions. Therefore, its long-wavelength limit is $\lim_{\mathbf{k}\to 0} \tilde{\Lambda}_{ij} \sim k^2 \lambda_{ij}$, where k is the modulus of the wavevector. Thus, the macroscopic, $\mathbf{k} = (0,0,0)$, and stationery, $\omega = 0$, components of the conserved currents $J_i = \frac{1}{V}\int j(\mathbf{r})$ (the conserved fluxes) are related to the density gradients $D_i = \frac{1}{V}\int \nabla q(\mathbf{r})$ through the equation:

$$J_i = \sum_j \lambda_{ij} D_j.$$

Finally, the gradients of the densities can be expressed as a linear combination of local intensive variables through the macroscopic susceptibilities $\chi_{ij} = \frac{1}{V}\frac{\partial A_i}{\partial \alpha_j}$. Therefore:

$$J_i = \sum_j L_{ij} F_j, \tag{1.5}$$

where $F_j = \frac{1}{V}\int \nabla \alpha_j(\mathbf{r})$ is the j-th thermodynamic force, and $L_{ij} = \sum_l \lambda_{il}\chi_{lj}$ are the Onsager's coefficients. Notably, L_{ij} is a symmetric matrix, as demonstrated by Onsager's celebrated reciprocity relations $L_{ij} = L_{ji}$, which were proven under the hypothesis of microscopic reversibility [1–3].

1.3 GREEN-KUBO LINEAR-RESPONSE THEORY

The Onsager's coefficients L_{ij} can be evaluated at equilibrium using the Green-Kubo (GK) linear-response theory [4–6]. In his seminal papers [5, 6], Kubo derives the linear-response theory for systems subject to external perturbations. In Ref. [5], the author focuses on mechanical perturbations and the corresponding conductivities, such as electrical and magnetic conductivities. In Ref.[6], he extends this framework to derive analogous formulas for the thermo-(electrical) case, where not all thermodynamic forces are mechanical. In the following section, the GK theory is reviewed for both classical and quantum regimes, beginning with the former.

1.3.1 *Classical regime*

Let us consider a system with N particles whose *natural motion* is described by the Hamiltonian:

$$H(\Gamma) = \sum_i \frac{\mathbf{P}_i^2}{2M_i} + U(\{\mathbf{R}_i\})$$

where $\mathbf{P}_i$, $\mathbf{R}_i$ are, respectively, the momentum and position of the i-th atom, M_i its mass, U is a many-body potential and Γ is a point in phase space. For each observable $B(\Gamma)$, the average with respect to the instantaneous distribution function $\rho(t)$ is defined as:

$$\langle B\rangle_{\rho(t)} = \int d\Gamma \rho(\Gamma, t) B(\Gamma),$$

while for simplicity the average with respect to the equilibrium distribution is indicated with the short-hand $\langle\cdot\rangle = \langle\cdot\rangle_{\rho_{eq}}$

The time-dependence is due to the evolution of the ρ, whose equation of motion is:

$$\frac{d\rho}{dt} = \{H, \rho\} \tag{1.6}$$

$$= iL\rho \tag{1.7}$$

where L is the Liouvillian operator defined as $iL\cdot = \{H, \cdot\}$ and $\{,\}$ indicates the Poisson brackets

$$\{A, B\} = \sum_{i\alpha} \frac{\partial A}{\partial R_i^\alpha}\frac{\partial B}{\partial P_i^\alpha} - \frac{\partial B}{\partial R_i^\alpha}\frac{\partial A}{\partial P_i^\alpha}$$

and α indicates the Cartesian direction. At thermal equilibrium, the distribution $\rho = \rho_{eq}$ is stationary, i.e. $\{H, \rho\} = 0$, and no steady flow can arise. Therefore, let us consider an external perturbation in the Hamiltonian which drives the system out of equilibrium:

$$H' = -AF(t)$$

where $F(t)$ is an explicitly time-dependent force and $A = A(\Gamma)$. Thus, the equation of motion for $\rho'(t) = \rho(t) - \rho_{eq}$, at first order in the perturbation, becomes:

$$\frac{d\rho'}{dt} = \{H, \rho'\} - F(t)\{H', \rho\}.$$

Assuming that the perturbation is switched one adiabatically in the infinite past, i.e. $\rho'(t \to -\infty) = 0$, the above equation is formally solved as:

$$\rho' = -\int_{-\infty}^{t} dt' e^{iL(t-t')} F(t)\{A, \rho_{eq}\}. \tag{1.8}$$

Therefore:

$$\begin{aligned}
\Delta\langle B\rangle_{\rho(t)} &= \langle B\rangle_{\rho(t)} - \langle B\rangle \\
&= \int d\Gamma_0 \rho'(t, \Gamma_0) B(\Gamma_0) \\
&= -\int d\Gamma_0 \int_{-\infty}^{t} dt' e^{iL(t-t')} F(t')\{A, \rho_{eq}\}(\Gamma_0) B(\Gamma_0) \\
&= -\int d\Gamma_0 \int_{-\infty}^{t} dt' F(t')\{A, \rho_{eq}\}(\Gamma_0) B(\Gamma_{t-t'}) \\
&= -\int d\Gamma_0 \int_{-\infty}^{t} dt' F(t')\{A, \rho_{eq}\}(0) B(t-t')
\end{aligned} \tag{1.9}$$

where $B(t-t') = e^{-iL(t-t')}B(0)$ indicates the formal solution of the equation of motion for B, i.e. $\dot{B} = \{B, H\}$, under the effect of the unperturbed Hamiltonian. As somewhat pedantically remarked in Eq. (1.9), B depends on time only through the dynamics of Γ.

From Eq. (1.9) one obtains an expression for the *response function* $\phi_{AB}(t)$. Indeed, by definition:

$$\Delta\langle B\rangle_{\rho(t)} = \int_{-\infty}^{t} dt' \phi_{AB}(t-t')F(t')$$

and by comparison with Eq. (1.9), one obtains that:

$$\phi_{AB}(t) = -\int d\Gamma\{A,\rho_{eq}\}(0)B(t) \tag{1.10}$$

Applying Eq. (1.9) for a perturbation $F(t) = F\Theta(-t)$ continuously applied from the infinite past to $t = 0$ and then switched off, where Θ is the Heaviside function, one obtains:

$$\Delta\langle B\rangle_{\rho(0^+)} = F\int_0^\infty dt' \phi_{AB}(t')$$

which coincides with the $\omega \to 0$ limit of the so-called *admittance* $\chi_{AB}(\omega) = \int_0^\infty e^{i\omega t}\phi_{AB}(t)$.

While the previous expressions are formally correct for any thermodynamical ensemble, their computation is simplified in the canonical one, where ρ_{eq} has a handy expression:

$$\begin{aligned}\rho_{eq}(\Gamma) &= \frac{e^{-\beta H(\Gamma)}}{Z}\\ &= e^{-\beta(H(\Gamma)-\mathcal{F})},\end{aligned}$$

where Z is the partition function, $\mathcal{F} = -k_B T\log(Z)$ is the free energy, and k_B is the Boltzmann's constant. Moreover, the computation of ϕ_{AB} is simplified by the identity:

$$\{A,\rho_{eq}\} = -\beta\rho_{eq}\dot{A}.$$

Thus,

$$\phi_{AB}(t) = \beta\int d\Gamma\rho_{eq}\dot{A}(0)B(t). \tag{1.11}$$

A simple application of the formulas above is the computation of electrical conductivity σ for a system of ions with charges Z_i. Assuming as perturbation a (spatially) homogeneous electric field, $H' = -\sum_i Z_i E\mathbf{r}_i\Theta(-t)$, and as observable the conserved current $J = \frac{1}{V}\sum_i Z_i\dot{\mathbf{r}}_i$ the resulting out of equilibrium flux is:

$$\begin{aligned}\langle J^\alpha\rangle_{\rho(0^+)} &= \sum_\beta \frac{V}{k_B T}\int_0^\infty dt\langle J^\beta(t)J^\alpha(0)\rangle E\\ &= \sigma E\end{aligned}$$

More generally, Onsager's coefficients can be computed by considering an external perturbation which is a linear combination of the conserved densities:

$$H' = \sum_i \int d\mathbf{r}\, v(\mathbf{r},t)a(\mathbf{r}).$$

and $\nu(\mathbf{r}, t) = \Theta(t)\nu(\mathbf{r})$. Combining this expression with Eq. (1.11) and the continuity equation ,Eq. (1.3), yields to:

$$\begin{aligned}\langle J_i^\alpha \rangle_{\rho(0^+)} &= \frac{1}{Vk_BT} \sum_j \int_0^\infty dt' \int d\mathbf{r} \int d\mathbf{r}' \langle \dot{a}_j(\mathbf{r}', 0) j_i^\alpha(\mathbf{r}, t') \rangle \nu(\mathbf{r}') \\ &= -\frac{1}{Vk_BT} \sum_{j\beta} \int_0^\infty dt' \int d\mathbf{r} \int d\mathbf{r}' \langle \partial_{r'_\beta} j_j^\beta(\mathbf{r}', 0) j_i^\alpha(\mathbf{r}, t') \rangle \nu(\mathbf{r}') \\ &= \frac{1}{Vk_BT} \sum_{j\beta} \int_0^\infty dt' \int d\mathbf{r} \int d\mathbf{r}' \langle j_j^\beta(\mathbf{r}', 0) j_i^\alpha(\mathbf{r}, t') \rangle \partial_{r'_\beta} \nu(\mathbf{r}')\end{aligned}$$

where the second and third lines are connected by an integration by parts. Assuming spatial homogeneity and that $\partial_{r_\beta}\nu$ weakly depends on space, one recovers Eq. (1.5) and therefore the expression [4–6] for Onsager's coefficients:

$$L_{ij}^{\alpha\beta} = \frac{V}{k_BT} \sum_{j\beta} \int_0^\infty dt' \langle J_j^\beta(0) J_i^\alpha(t') \rangle. \tag{1.12}$$

It is worth noticing that here the volume V appears at the numerator and not at the denominator, as in Ref. [5], because we are considering as J the macroscopic average of the current, not its integral.

1.3.2 *Quantum regime*

The quantum formulation of Green-Kubo (GK) can be straightforwardly obtained by the classical one with the following few rules of correspondence. The classical observables $A(\Gamma)$ are now substituted by operators $\hat{A}$, indicated by a hat symbol $\hat{\cdot}$, and their average is defined through the density operator $\hat{\rho}$:

$$\langle A \rangle_\rho = \mathrm{Tr}(\hat{\rho}\hat{A})$$

The equations of motion become:

$$\begin{aligned} i\hbar\dot{\hat{\rho}} &= [\hat{H}, \hat{\rho}] \\ i\hbar\dot{\hat{A}} &= [\hat{A}, \hat{H}] \end{aligned}$$

where the $\hbar$ is the Planck constant and the Poisson brackets have been formally replaced by the commutation operation $[\hat{A}, \hat{B}] = \hat{A}\hat{B} - \hat{B}\hat{A}$ (times a factor $\frac{1}{i\hbar}$). Then, Eq. (1.10) becomes:

$$\phi_{AB}(t) = \frac{1}{i\hbar} \mathrm{Tr}([\hat{\rho}, \hat{A}]\hat{B}(t)). \tag{1.13}$$

As in the classical case, the response function computation is simplified in the canonical ensemble. Indeed, using the following identity

$$\begin{aligned}[\hat{A}, \exp(-\beta\hat{H})] &= \exp(-\beta\hat{H}) \int_0^\beta d\lambda \exp(\lambda\hat{H})[\hat{H}, \hat{A}] \exp(-\lambda\hat{H}) \\ &= -i\hbar \exp(-\beta\hat{H}) \int_0^\beta d\lambda \exp(\lambda\hat{H})\dot{\hat{A}} \exp(-\lambda\hat{H}) \\ &= -i\hbar \exp(-\beta\hat{H}) \int_0^\beta d\lambda \dot{\hat{A}}(-i\hbar\lambda)\end{aligned}$$

where $\dot{\hat{A}}(-i\hbar\lambda) = \exp(\lambda\hat{H})\dot{\hat{A}} \exp(-\lambda\hat{H})$ indicates the evolution in imaginary time, Eq. (1.11) becomes:

$$\phi_{AB}(t) = \int_0^\beta d\lambda \langle \dot{\hat{A}}(-i\hbar\lambda)\hat{B}(t)\rangle. \tag{1.14}$$

Thus, the quantum GK formula for Onsager'scoefficients is:

$$L_{ij}^{\alpha\beta} = V \int_0^\infty dt' \int_0^{1/k_B T} d\lambda \langle \hat{J}_j^\beta(-i\hbar\lambda)\hat{J}_i^\alpha(t')\rangle \tag{1.15}$$

1.4 THERMAL TRANSPORT

The GK formula of Eq. (1.15) is valid for any Onsager coefficient, despite being proven, here, only for mechanical perturbations. For instance, for thermal transport, the thermodynamic force depends on $\nabla(1/T(\mathbf{r}))$ which is not trivially associated with a perturbation H'. An alternative proof to Ref. [6] for thermal transport can be obtained by considering the distribution at local equilibrium at $t = 0$ that relaxes towards global thermal equilibrium driven by H. Since the proof is similar to the mechanical case, only the classical case is reported here, as the quantum version can be effortlessly obtained as in the previous case.

Let us consider a canonical-like distribution with a local temperature $\beta(\mathbf{r}) = 1/k_B T(\mathbf{r}) \approx \beta - \nabla T(\mathbf{r}) \cdot \mathbf{r}/k_B T^2$, where β, T without the position label are, with a slight abuse of notation, the average values. Thus:

$$\rho_{loc}(\Gamma) = \frac{1}{Z_{loc}} \exp\left\{ \left(-\beta H(\Gamma) + \frac{\nabla T}{k_B T^2} \cdot \int d\mathbf{r}\, \mathbf{r}\varepsilon(\mathbf{r}, \Gamma) \right) \right\}$$

where $\varepsilon(r, \Gamma)$ is the energy density (one of the many equivalent possible definitions, as explained below). At first order in the temperature gradient:

$$\rho'(\Gamma) = \rho_{loc}(\Gamma) - \rho_{eq}(\Gamma) \tag{1.16}$$

$$= \rho_{eq}(\Gamma) \left(1 + \frac{\nabla T}{k_B T^2} \cdot \int d\mathbf{r}\, \mathbf{r}\delta\varepsilon(\mathbf{r}, \Gamma) \right) + o(\nabla T^2), \tag{1.17}$$

where $\delta\varepsilon$ indicates the deviation from equilibrium. Applying Eq. (1.8), one obtains:

$$\begin{aligned}\rho'(t,\Gamma) &= \rho'(t=0,\Gamma) + \int_0^t dt'\ \Delta\dot{\rho}(t',\Gamma) \\ &= \rho'(t=0,\Gamma) + \int_0^t dt'\ e^{iLt'}\Delta\dot{\rho}(0,\Gamma).\end{aligned}$$

Since $\Delta\rho(t\to\infty)=0$, then:

$$\begin{aligned}\rho'(t=0,\Gamma) &= -\int_0^\infty dt'\ e^{iLt'}\Delta\dot{\rho}(0,\Gamma) \\ &= +V\frac{\nabla T}{k_B T^2}\cdot\int_0^\infty dt'\ \mathbf{J}_E(\Gamma_{-t'})\rho_{eq}(\Gamma) \\ &= -V\frac{\nabla T}{k_B T^2}\cdot\int_0^\infty dt'\ \mathbf{J}_E(\Gamma_{t'})\rho_{eq}(\Gamma)\end{aligned} \tag{1.18}$$

where J_E is the energy flux defined as [7]

$$\begin{aligned}\mathbf{J}_E(\Gamma) &= \frac{1}{V}\int d\mathbf{r}\ \mathbf{r}\dot{\varepsilon}(\mathbf{r},\Gamma) \\ &= \frac{1}{V}\int d\mathbf{r}\ \mathbf{r}\delta\dot{\varepsilon}(\mathbf{r},\Gamma),\end{aligned} \tag{1.19}$$

where $\dot{\varepsilon} = \delta\dot{\varepsilon}$ since the equilibrium value is time-independent and the third line of Eq. (1.18) is obtained by taking into account that $\mathbf{J}_E$ is odd under time reversal and, as an observable, it evolves according to e^{-iLt}. Finally, by computing the average current at $t = 0^+$ one obtains:

$$\begin{aligned}\langle J_E^\alpha\rangle_{\rho(0^+)} &= \frac{V}{k_B}\sum_\beta \nabla_\beta\left(\frac{1}{T}\right)\int_0^\infty dt'\langle J_E^\beta(0)J_E^\alpha(t')\rangle \\ &= \sum_\beta L_{EE}^{\alpha\beta}\nabla_\beta\left(\frac{1}{T}\right).\end{aligned}$$

Therefore, the classical GK formula for the energy-energy Onsager's coefficient is

$$L_{EE}^{\alpha\beta} = \frac{V}{k_B}\int_0^\infty dt'\langle J_E^\beta(0)J_E^\alpha(t')\rangle, \tag{1.20}$$

which, in the quantum regime, becomes:

$$L_{EE}^{\alpha\beta} = VT\int_0^\infty dt'\int_0^{1/k_BT} d\lambda\langle\hat{J}_E^\beta(-i\hbar\lambda)\hat{J}_E^\alpha(t')\rangle. \tag{1.21}$$

This expression is consistent with Eq. (1.15) minus a prefactor T, which is needed for dimensional reasons: $\sim T\nabla(1/T)\int d\mathbf{r}\ \mathbf{r}\varepsilon(\mathbf{r})$ has the dimension of a mechanical perturbation H'.

1.5 INVARIANCE PRINCIPLES OF TRANSPORT COEFFICIENTS

1.5.1 *Thermal transport in multi-component systems*

For an isotropic material, the thermal conductivity κ is the linear transport coefficient that relates $-\nabla T$ to the nonequilibrium steady-state heat flux, in the *absence of convection*, i.e., when the nonequilibrium particle fluxes are zero. This definition presents two challenges. First, for a system with K components, the heat flux is defined as

$$J_Q = J_E - \sum_{s=1}^{K} h_s J_s,$$

where h_s are the partial enthalpies [8], and J_s are the particle fluxes. For a monoatomic system, due to momentum conservation, the heat and energy fluxes coincide, and $\kappa = \frac{L_{EE}}{T^2}$. However, in general, they differ. To calculate the Onsager coefficients related to heat flux, the heat flux should be used, but this requires the cumbersome computation of partial enthalpies [9–11]. Second, the zero net particle flux condition couples κ with other Onsager coefficients beyond L_{EE} or L_{QQ}.

Both challenges can be addressed as follows. Consider a multicomponent system with K components. Since total momentum is conserved, there are generally $K-1$ independent mass fluxes. Including the energy flux, there are up to K independent conserved fluxes. For an isotropic system, in the case where $K = 2$, the phenomenological equations are:

$$\langle \mathbf{J}_E \rangle_{\rho(0^+)} = L_{EE}\nabla(1/T) + L_{EM}\nabla(\mu/T),$$

$$\langle \mathbf{J}_M \rangle_{\rho(0^+)} = L_{ME}\nabla(1/T) + L_{MM}\nabla(\mu/T),$$

where $\mathbf{J}_E$ is the energy flux, $\mathbf{J}_M$ is the mass flux of any of the two species ($J_1 = -J_2$ due to the conservation of total momentum). The out-of-equilibrium average is defined in the Green-Kubo theoretical framework. Imposing the condition of zero convection gives:

$$\begin{aligned} \langle \mathbf{J}_E \rangle_{\rho(0^+)} &= (L_{EE} - L_{EM}^2/L_{MM})\nabla(1/T) \\ &= -\frac{1}{(\mathbf{L}^{-1})_{EE}T^2}\nabla T \\ &= -\kappa\nabla T \end{aligned} \tag{1.22}$$

where $\mathbf{L}^{-1}$ is the inverse of the Onsager matrix, and $L_{ME} = L_{EM}$ due to Onsager's reciprocity relation. It can be shown via linear algebra that the relationship between κ and $\mathbf{L}^{-1}$ holds for any number of components [12]. Furthermore, the thermal conductivity computed from Eq. (1.22) is invariant under the transformation $J_E \to J_E + \sum_l^{K-1} c_l J_l$, where c_l are arbitrary coefficients. This property is known as the *convective invariance* of thermal conductivity [12, 13]. One important consequence of convective invariance is that the thermal conductivities computed from the heat flux and energy flux are identical, thereby eliminating the need to compute partial enthalpies.

However, while the above discussion is general and fundamental in computing the thermal conductivity of multi-component fluids [7, 12], there are systems where the number of relevant fluxes is smaller than the number of components. For instance, in a molecular fluid like water, the hydrogen and oxygen mass fluxes strongly depend on each other due to the molecular bond. Solids are generally characterized by the absence of atomic diffusions of any species, therefore energy flux becomes the only relevant conserved flux involving the atomic nuclei. Indeed, if there is no atomic diffusion, the mass flux becomes the time derivative of a bounded vector. For instance the mass flux of the first component would be $J_1(t) \propto \frac{d}{dt}\frac{1}{V} m_1 \sum_i (\mathbf{R}_i^1(t) - \mathbf{R}_i^1(0)) = \frac{1}{V}\sum_i \mathbf{P}_i^1$, where the maximum displacement per atom is bounded $\max(|R_i(t) - R_i(0)|) < \infty$ since there is no diffusion. As it is proved in the next section, such *not-diffusive* fluxes can not give a significant contribution to the computation of transport coefficients, $L_{ij} = 0\ \forall (i,j) \neq (E,E)$. As a consequence, the energy flux is the only relevant flux for the computation of thermal conductivity of solids.

1.5.2 *Gauge invariance of transport coefficients*

Green-Kubo formulas provide a formally simple relation between fluxes and the corresponding transport coefficients. However, challenges in uniquely defining conserved densities and associated fluxes have limited their use in computer simulations. For example, the inherent indeterminacy of quantum mechanical energy density prevented the evaluation of thermal conductivity using *ab initio* molecular dynamics for a long time [14]. This difficulty has been recently overcome [13, 15, 16] with the realization that conserved fluxes and densities possess a certain degree of arbitrariness, which does not affect the transport coefficients, as these are *gauge invariant*.

From a macroscopic point of view, two conserved densities $a(\mathbf{r})$ and $a'(\mathbf{r})$ should be considered equivalent if they have the same macroscopic average $\frac{1}{V}\int d\mathbf{r}\ a(\mathbf{r})$ in the bulk limit $V \to \infty$. For instance, the two conserved densities could differ for the divergence of a bounded vector field $\mathbf{p}(\mathbf{r})$. Therefore, applying the continuity equation, both the conserved density and current would transform under the following *gauge*:

$$
\begin{aligned}
a'(\mathbf{r}) &= a(\mathbf{r}) - \nabla \cdot p(\mathbf{r}) \\
\mathbf{j}'(\mathbf{r}) &= \mathbf{j}(\mathbf{r}) + \dot{\mathbf{p}}(\mathbf{r})
\end{aligned}
$$

While the macroscopic average of the two conserved densities have a vanishing difference in the infinite volume limit $O(V^{-1/3})$, the macroscopic flux changes by a total time derivative:

$$
\begin{aligned}
\mathbf{J}'(t) &= \mathbf{J}(t) + \frac{1}{V}\int d\mathbf{r}\ \dot{\mathbf{p}}(\mathbf{r},t) \\
&= \mathbf{J}(t) + \dot{\mathbf{P}}(t).
\end{aligned}
$$

The gauge can transform the macroscopic flux and its autocorrelation, as it has been shown with Molecular Dynamics (MD) simulations [15]. However, the transport coefficients are invariant [13]. For diagonal Onsager's coefficients in the quantum case, the proof can be straightforwardly obtained following Ref. [17]. By performing a spectral decomposition in the basis of the (full) Hamiltonian eigenstates $\{|n\rangle\}$ of $\hat{H}|n\rangle = E_n|n\rangle$, Eq. (1.15) becomes:

$$\begin{aligned} L &= V \sum_{nm} \frac{e^{-\beta E_n}}{Z} \int_0^\beta d\lambda \, \pi\delta((E_n - E_m)/\hbar) e^{\lambda(E_n - E_m)} |\langle n|J|m\rangle|^2 \\ &= \beta V \pi \sum_{nm} \frac{e^{-\beta E_n}}{Z} \delta((E_n - E_m)/\hbar) |\langle n|J|m\rangle|^2, \end{aligned}$$

where the time integral has been extended to $\int_0^\infty \to \frac{1}{2}\int_{-\infty}^\infty$ due to time-reversal symmetry. Since

$$\begin{aligned} \langle n|\dot{\hat{P}}|m\rangle &= \frac{1}{i\hbar}\langle n|[\hat{P}, \hat{H}]|m\rangle \\ &= \frac{E_m - E_n}{i\hbar}\langle n|\hat{P}|m\rangle \end{aligned}$$

and $\hat{P}$ is bounded by hypothesis, the difference between the Onsager's coefficient in the two gauges is proportional to terms like $(E_n - E_m)^l \delta(E_n - E_m) = 0$, where $l = 1, 2$. Therefore,

$$\begin{aligned} L' - L &= V \int_0^\infty dt' \int_0^\beta d\lambda \langle \hat{J}(-i\hbar\lambda)\dot{\hat{P}}(t') + \dot{\hat{P}}(-i\hbar\lambda)\hat{J}(t') + \dot{\hat{P}}(-i\hbar\lambda)\dot{\hat{P}}(t')\rangle \\ &= 0, \end{aligned} \tag{1.23}$$

which concludes our proof.

2 THEORY OF LATTICE THERMAL CONDUCTIVITY

Heat transport in solid insulators, both disordered and crystalline, is dominated by the dynamics of lattice vibrations. This chapter delves into the derivation and application of the unified QHGK approach to lattice thermal conductivity. This approach bridges methodologies for crystals and glasses, highlighting their conceptual differences. Additionally, I present the generalization of the QHGK approach beyond the Single-Mode (SM) and Relaxation Time Approximation (RTA) for the lattice vibrations correlation functions [18]. The connection and differences between the formulations of QHGK and the BTE approach are showcased using the Li_3ClO anti-perovskite as a case study.

2.1 LATTICE DYNAMICAL APPROACHES FOR THERMAL CONDUCTIVITY

In solid insulators, in the absence of other significant transport mechanisms such as atomic diffusion and electron transport, heat is primarily carried by atomic vibrations around their equilibrium positions. Far from melting, the atomic displacements from equilibrium positions are much smaller than the interatomic distances, and their dynamics are well described within a Quasi-Harmonic (QH) framework. This framework involves a Taylor expansion of the Born-Oppenheimer (BO) potential around the equilibrium positions, where the harmonic term dominates, and higher-order terms are treated perturbatively. Compared to MD methods, whether in equilibrium or non-equilibrium forms [7, 19], lattice dynamics approaches cannot fully account for the anharmonic potential. However, while MD methods are inherently classical and affected by sampling problems [20], lattice dynamics models can be solved numerically and can effortlessly account for the quantum nature of nuclei vibrations. Such quantum corrections are fundamental below the Debye temperature when quantities like the specific heat significantly differ from their classical counterpart predicted by the equipartition law.

Until recent years, the two main, and separated, lattice dynamics methods to compute thermal conductivity were: the BTE [21, 22] and the AF method [23, 24], for crystals and disordered systems like glasses, respectively. The BTE approach, commonly used also for charge transport, is a semiclassical treatment that requires a quasi-particle framework for the carriers of heat or charge. The periodicity of the crystal plays a fundamental role in its applicability, as it allows one to associate a (crystal) momentum to the eigenstates of the harmonic Hamiltonian, the *phonon* quasi-particles. On the other hand, the AF method does not assume any periodicity in the system. However, as a purely harmonic theory, its ap-

plication to a typical crystal would result in a diverging thermal conductivity, and even for glasses, it can exhibit singular behavior in the bulk limit [25].

Recently, the two approaches have been unified by two, quantitatively equivalent [17, 18], methods: the QHGK approach [26] and the WBTE [27, 28]. The former is a implementation of GK formula under the hypothesis of a quasi-harmonic system, while the latter is a generalization of the BTE using Wigner transformations [28, 29]. By accounting for anharmonicity perturbatively and going beyond the quasi-particle framework, these two approaches bridge and extend the AF and BTE methods.

In principle, the evaluation of thermal conductivity through GK formulas can involve other fluxes apart from the energy one. Yet, in solid insulators only the latter is relevant, due to the absence of atomic diffusion and charge transport. Therefore, thermal conductivity can be computed by GK theory as $L^{\alpha\beta}_{EE}/T^2$, as discussed in Sec.1.5.1. By using Eqs. (1.20)-(1.21), one obtains, respectively the classical and quantum formula for heat conductivity:

$$\kappa^{\alpha\beta} = \frac{V}{k_B T^2} \int_0^\infty dt' \langle J^\beta(0) J^\alpha(t') \rangle. \tag{2.1}$$

and

$$\kappa^{\alpha\beta} = \frac{V}{T} \int_0^\infty dt' \int_0^{1/k_B T} d\lambda \langle \hat{J}^\beta_E(-i\hbar\lambda) \hat{J}^\alpha_E(t') \rangle. \tag{2.2}$$

where J is the energy flux in its classical and quantum version, the latter indicated with the hat symbol $\hat{\cdot}$.

2.2 HARMONIC ENERGY FLUX

The energy flux in the GK formula is associated with the energy density of the full, anharmonic, Hamiltonian. However, in the quasi-harmonic regime, the leading contribution to thermal conductivity can be obtained by considering only the harmonic part of the flux, while accounting for anharmonicity in its time-evolution[18, 26].

2.2.1 *Classical regime*

Let us obtain an expression for the harmonic energy flux, starting from the classical case. Following the derivation of Refs. [26, 30], let us consider the harmonic Hamiltonian:

$$\begin{aligned} H^\circ &= \sum_{i\alpha} \frac{M_i (\dot{u}_i^\alpha)^2}{2} + \frac{1}{2} \sum_{ij\alpha\beta} \Phi_{ij}^{\alpha\beta} u_i^\alpha u_j^\beta \\ &= \sum_{i\alpha} \frac{(\dot{p}_i^\alpha)^2}{2M_i} + \frac{1}{2} \sum_{ij\alpha\beta} \Phi_{ij}^{\alpha\beta} u_i^\alpha u_j^\beta, \end{aligned} \tag{2.3}$$

where $\mathbf{u}_i = \mathbf{R}_i - \mathbf{R}_i^\circ$ is the displacement of the i-th particle from its equilibrium position, M_i its mass, and

$$\Phi_{ij}^{\alpha\beta} = \frac{\partial^2 U}{\partial R_i^\alpha \partial R_j^\beta}$$

are the second derivatives of the BO potential U computed at mechanical equilibrium, i.e. $\mathbf{R} = \mathbf{R}^\circ$. Then, the local energy density can be defined as

$$\varepsilon(\mathbf{r}) = \sum_i \delta(\mathbf{r} - \mathbf{R}_i)\varepsilon_i,$$

where ε_i are the local atomic energies

$$\varepsilon_i = \sum_\alpha \frac{M_i(\dot{u}_i^\alpha)^2}{2} + \frac{1}{2}\sum_{ij\alpha\beta} \Phi_{ij}^{\alpha\beta} u_i^\alpha u_j^\beta.$$

Such definition immediately satisfies the condition $H^\circ(\Gamma) = \int d\mathbf{r}\ \varepsilon(\mathbf{r}, \Gamma)$. Taking into account that $\mathbf{u}_i$ and $\mathbf{p}_i = M_i\dot{\mathbf{u}}_i$ are phase-space elements that evolve under the effect of H°, the energy flux can be obtained by Eq. (1.19):

$$\begin{aligned}
\mathbf{J} &= \frac{1}{V}\sum_i \int d\mathbf{r}\ \mathbf{r}\left(\dot{\varepsilon}_i \delta(\mathbf{r} - \mathbf{R}_i) + \varepsilon_i \frac{d\mathbf{R}_i}{dt} \cdot \nabla_{\mathbf{R}_i}\delta(\mathbf{r} - \mathbf{R}_i)\right) \\
&= \frac{1}{V}\sum_i \mathbf{R}_i\dot{\varepsilon}_i + \varepsilon_i\dot{\mathbf{u}}_i \\
&= \frac{1}{V}\sum_i \mathbf{R}_i^\circ\dot{\varepsilon}_i + \frac{d}{dt}(\mathbf{u}_i\varepsilon_i)
\end{aligned} \tag{2.4}$$

where the differentiation properties of the delta distribution have been used, assuming that the surface integrals are negligible. In the last line, it appears a total time derivative of a bounded vector, in the absence of atomic diffusion. Thanks to the gauge invariance explained in Sec. 1.5.2, such a term can be neglected in the computation of the transport coefficient. Thus, the expression for the harmonic energy flux reads [23, 24]:

$$\begin{aligned}
J^\alpha &= \frac{1}{V}\sum_{i\alpha} R_i^{\circ,\alpha}\dot{\varepsilon}_i \\
&= \frac{1}{2V}\sum_{ij\beta\gamma} \Phi_{ij}^{\beta\gamma}(\mathbf{R}_i^\circ - \mathbf{R}_j^\circ)^\alpha u_i^\beta \dot{u}_j^\gamma,
\end{aligned}$$

where the minimum-image convection is intended for the computation of the interatomic distances, therefore obtaining a well-defined expression in Periodic Boundary Conditions (PBCs).

For a harmonic system, it is convenient to move to the basis of the normal coordinates ξ and momenta π. Indeed, it allows, among other simplifications, to efficiently compute thermal averages using Wick (see

for instance Ref. [31]) or Isserlis's theorems, respectively for the quantum and classical case. The normal variables are defined as:

$$\xi_\mu = \sum_{i\alpha} e_\mu^{i\alpha} \sqrt{M_i} u_i^\alpha \tag{2.5}$$

$$\pi_\mu = \sum_{i\alpha} e_\mu^{i\alpha} \sqrt{M_i} \dot{u}_i^\alpha \tag{2.6}$$

where e_μ is the μ-th eigenvector of the dynamical matrix $D_{ij}^{\alpha\beta} = \frac{1}{\sqrt{M_i M_j}} \Phi_{ij}^{\alpha\beta}$:

$$\sum_{j\beta} D_{ij}^{\alpha\beta} e_\mu^{j\beta} = \omega_\mu^2 e_\mu^{i\alpha}$$

and ω_μ is the (positive) angular frequency associated with the normal mode amplitude

$$a_\mu = \sqrt{\frac{\omega_\mu}{2}} \xi_\mu + i \frac{1}{\sqrt{2\omega_\mu}} \pi_\mu, \tag{2.7}$$

whose equation of motion is:

$$\begin{aligned} \dot{a}_\mu &= \{a_\mu, H^\circ\} \\ &= -i\omega_\mu a_\mu \end{aligned}$$

In this basis, the harmonic Hamiltonian and the energy flux become, respectively,

$$H^\circ = \sum_\mu \frac{1}{2} \omega_\mu (a_\mu^* a_\mu + a_\mu a_\mu^*)$$

and

$$\begin{aligned} J^\alpha &= J_R^\alpha + J_A^\alpha \\ &= -\frac{i}{2V} \sum_{\mu\mu'} v_{\mu\mu'}^\alpha \left(\frac{\omega_\mu + \omega_{\mu'}}{2} \right) (a_\mu^* a_{\mu'} - a_{\mu'}^* a_\mu) \\ &+ \frac{i}{2V} \sum_{\mu\mu'} v_{\mu\mu'}^\alpha \left(\frac{\omega_\mu - \omega_{\mu'}}{2} \right) (a_\mu^* a_{\mu'}^* - a_{\mu'} a_\mu) \end{aligned} \tag{2.8}$$

where $v_{\mu\mu}^\alpha$ is a generalized velocity matrix

$$v_{\mu\mu'}^\alpha = \frac{1}{2\sqrt{\omega_\mu \omega_\mu'}} \sum_{ij\beta\gamma} \frac{\Phi_{ij}^{\beta\gamma} (\mathbf{R}_i^\circ - \mathbf{R}_j^\circ)^\alpha}{\sqrt{M_i M_j}} (e_\mu^{i\beta})^* e_{\mu'}^{j\gamma}, \tag{2.9}$$

which is anti-Hermitian and it becomes anti-symmetric if the eigenvectors are chosen real. $\mathbf{J}_R$ and $\mathbf{J}_A$ are, respectively, the so-called *resonant* and *anti-resonant* components of the energy flux. As shown in Refs. [17, 26], the anti-resonant one in the quasi-harmonic approximation gives a negligible contribution to the thermal conductivity. In a nutshell, the resonant

and anti-resonant terms in QHGK would lead, respectively, to terms proportional to $\sim \delta(\omega_\mu - \omega_{\mu'})$ and $\sim \delta(\omega_\mu + \omega'_\mu)$, in the limit of vanishing linewidths. Since the angular frequencies are defined as positive, even taking into account a small anharmonic smearing, the second condition is far more restrictive than the first one.

A more straightforward justification for neglecting the anti-resonant term in the quasi-harmonic approximation, without actually computing its contribution, can be obtained by observing that

$$J^\alpha_A = \frac{1}{2V}\frac{d}{dt}\bigg|_{H=H^\circ} \sum_{\mu\mu'} v^\alpha_{\mu\mu'} \frac{\omega_\mu - \omega_{\mu'}}{2(\omega_\mu + \omega_{\mu'})}(a^*_\mu a^*_{\mu'} + a_{\mu'} a_\mu),$$

i.e. the antiresonant term is the total time derivative of a bounded vector, therefore the gauge invariance prevents it from affecting the thermal conductivity. However, it must be stressed that such a term is a total time derivative only if the Hamiltonian is purely harmonic, contrary to the total time derivative of Eq. (2.4). Therefore, while its contribution could be significant in strongly anharmonic solids, in the limit of small anharmonicity the energy flux can be approximated with its resonant part $J^\alpha \to J^\alpha_R$.

2.2.2 *Quantum regime*

Finally, the quantum energy flux operator can be obtained analogously, as shown by Refs. [17, 30]. The quantum version of the harmonic Hamiltonian and of the energy flux, already restricted to the resonant term, read:

$$\hat{H}^\circ = \sum_\mu \hbar\omega_\mu \left(\hat{a}^\dagger_\mu \hat{a}_\mu + \frac{1}{2}\right)$$

$$\hat{J}^\alpha = -\frac{i\hbar}{2V} \sum_{\mu\mu'} v^\alpha_{\mu\mu'} \left(\frac{\omega_\mu + \omega_{\mu'}}{2}\right)(\hat{a}^\dagger_\mu \hat{a}_{\mu'} - \hat{a}^\dagger_{\mu'} \hat{a}_\mu), \tag{2.10}$$

where the normal mode amplitudes have been substituted by $a \to \sqrt{\hbar}\hat{a}$, $\hat{a}, \hat{a}^\dagger$ being, respectively, the corresponding bosonic annihilation and creation operators. The following equations summarize the main corresponding rules between the classic and quantum regimes:

$$\begin{cases} \text{(classic)} \\ \dot{a}_\mu = \{a_\mu, H^\circ\} \\ \langle a^*_{\mu'} a_\mu \rangle^\circ = \delta_{\mu\mu'} \dfrac{k_B T}{\omega_\mu} \end{cases} \iff \begin{cases} \text{(quantum)} \\ \dot{\hat{a}}_\mu = \dfrac{1}{i\hbar}[\hat{a}_\mu, \hat{H}^\circ] \\ \langle \hat{a}^\dagger_{\mu'} \hat{a}_\mu \rangle^\circ = \delta_{\mu\mu'} n_\mu \\ [\hat{a}_\mu, \hat{a}^\dagger_\mu] = 1 \end{cases}$$

where $n_\mu = n(\omega_\mu) = (e^{\hbar\omega_\mu/k_B T} - 1)^{-1}$ is the Bose-Einstein distribution.

2.2.3 *Energy flux in the crystalline basis*

Up to this point, no assumption of periodicity has been made. However, when discussing crystals it is convenient to operate with the Bloch basis. In such basis, each normal mode is labeled with $\mu = (\mathbf{q}, s)$, where $\mathbf{q}$ and s are, respectively, the wavevector in the Brillouin Zone (BZ) and the band index. Due to the periodicity, both the dynamical matrix and the generalized velocity matrix have a block structure, with the standard phonon group velocity on the diagonal:

$$\mathbf{v}_{\mathbf{q}\mathbf{q}'ss'} = -i\delta_{\mathbf{q}\mathbf{q}'}\mathbf{v}_{\mathbf{q}ss'}$$
$$\mathbf{v}_{\mathbf{q}ss} = \mathbf{v}_{\mathbf{q}s} = \nabla_{\mathbf{q}}\omega_{\mathbf{q}s},$$

where the $-i$ factor has been used to recover the group velocity and therefore simplify the comparison with the BTE [21] and WBTE [17, 27, 28] approaches. $\mathbf{v}_{\mathbf{q}ss'}$ is not anti-Hermitian as $\mathbf{v}_{\mathbf{q}\mathbf{q}'ss'}$, due to the imaginary multiplicative factor, but it has the following properties [17]: $\mathbf{v}_{\mathbf{q}ss'} = (\mathbf{v}_{\mathbf{q}s's})^*$. Moreover, for a lattice with inversion symmetry $\mathbf{v}_{-\mathbf{q}ss'} = -\mathbf{v}_{\mathbf{q}s's}$.

Recently, Ref. [28] raised questions about which convention for the Bloch basis should be used in thermal transport evaluations. The eigenvectors corresponding to different conventions are related by a unitary transformation,

$$U_{bb'}(\mathbf{q}) = \delta_{bb'}e^{i\mathbf{q}\cdot\boldsymbol{\varphi}(b)},$$

where b denotes the index of the atom in the unit basis, and $\boldsymbol{\varphi}(b)$ is a phase vector that defines the convention. For example, two commonly used conventions are the "step-like" convention, where $\boldsymbol{\varphi}(b) = 0$, and the "smooth" convention, where $\boldsymbol{\varphi}(b) = \mathbf{r}_b$, with $\mathbf{r}_b$ representing the position of the b-th atom in the unit basis. Surprisingly, Ref. [28] observed that the WBTE generalized velocity matrix and, more importantly, their thermal conductivity depend on the convention. In particular, the $s \neq s'$ elements of WBTE generalized velocity matrix are affected, since the diagonal elements (the group velocities) depend only on the eigenvalues. Despite the similarity between the two theories, it is worth highlighting that the generalized velocity matrix in QHGK does not depend on this transformation. For details on this invariance see Appendix A.1.

2.3 THE QUASI-HARMONIC GREEN-KUBO APPROACH

Following Eq. 2.2, the thermal conductivity is computed by evaluating the autocorrelation of the energy flux operator. To unclutter the notation the Cartesian indices are omitted in the rest of the discussion. Unless otherwise specified, we indicate as $\kappa = \frac{1}{3}\sum_\alpha \kappa^{\alpha\alpha}$, the isotropic average of Eq. 2.2. Since the operator is quadratic in the creation/annihilation operator, its autocorrelation requires the computation of 4–point correlation functions, i.e. two-body Green's functions in many-body parlance. To compute this quantity, the QHGK theory relies on two, related, approximations: the SM and the RTA.

The former SM approximation amounts to factorizing four-point correlation functions into linear combinations of products of two-point ones, such as, *e.g.*,

$$\langle \hat{a}^\dagger_{\mu_1}(t)\hat{a}_{\mu_2}(t)\hat{a}^\dagger_{\mu_3}\hat{a}_{\mu_4}\rangle \approx \langle \hat{a}^\dagger_{\mu_1}\hat{a}_{\mu_1}\rangle\langle \hat{a}_{\mu_3}\hat{a}^\dagger_{\mu_3}\rangle\delta_{\mu_1\mu_2}\delta_{\mu_3\mu_4} + \langle \hat{a}^\dagger_{\mu_1}(t)\hat{a}_{\mu_1}(0)\rangle\langle \hat{a}_{\mu_2}(t)\hat{a}^\dagger_{\mu_2}(0)\rangle\delta_{\mu_1\mu_4}\delta_{\mu_2\mu_3}, \quad (2.11)$$

where $\langle\cdot\rangle$ indicates the equilibrium average with respect to the full (weakly) anharmonic Hamiltonian.

In the parlance of Many-Body Perturbation Theory (MBPT), this factorization, which would be correct in the harmonic case, is described as the neglect of vertex corrections to the correlation function and referred to as the *dressed-bubble approximation* [17]. Physically, vertex corrections describe the decay channels of different normal modes, and their neglect amounts to expressing the propagation and decay of each of them independently from all the others, as if determined by the interaction with a common, mean-field-like, heat bath.

The latter approximation, RTA, consists of assuming a weakly damped exponential dependence on time as ansatz for the single-mode *greater* and *lesser* Green's functions,

$$\begin{aligned} g^>_\mu(t) &= -i\langle \hat{a}_\mu(t)\hat{a}^\dagger_\mu\rangle \\ &\approx -i(n_\mu+1)e^{-i\omega_\mu t-\gamma_\mu|t|} \\ g^<_\mu(t) &= i\langle \hat{a}^\dagger_\mu\hat{a}_\mu(t)\rangle \\ &\approx i n_\mu e^{-i\omega_\mu t-\gamma_\mu|t|} \end{aligned} \quad (2.12)$$

where, in the quasi-harmonic limit, $\gamma/\omega \ll 1$. Equivalently, it can be said that the $g^{\lessgtr}_\mu$ spectral function (the imaginary part of its Laplace-Fourier transform) is Lorentzian. In a MBPT framework, this roughly corresponds to neglecting the frequency dependence of the phonon self-energies. Physically, this second approximation assumes that the common heat bath is essentially a white noise so that its interaction with the normal modes is Markovian, *i.e.* unaffected by any memory effects.

For each normal mode, the RTA's *ansatz* introduces a characteristic lifetime, whose inverse is twice the anharmonic linewidth $\tau_\mu^{-1} = 2\gamma_\mu$. Its computation depends on the different kinds of scattering sources considered and it is generally computed with Fermi's Golden Rule (FGR).

Let us apply the first approximation. Since the equilibrium average of the flux is null, only the second term of Eq. (2.11) contributes. Thus, Eq. (2.2) becomes:

$$\kappa = \frac{1}{3VT}\sum_{\mu\mu'}\frac{\hbar^2(\omega_\mu+\omega_{\mu'})^2}{4}|v_{\mu\mu'}|^2 \times \int_0^\infty dt' \int_0^{1/k_BT} d\lambda\, g^>_\mu(-t'-i\hbar\lambda)g^<_{\mu'}(t'+i\hbar\lambda).$$

Then, by using the time inversion symmetry of the correlation function and the convolution properties of the Fourier Transform, one obtains the following expression [17, 32]:

$$\kappa = \frac{1}{3V}\sum_{\mu\mu'}\frac{\hbar^2(\omega_\mu+\omega_{\mu'})^2}{4}|v_{\mu\mu'}|^2(I_{\mu\mu'}+I_{\mu'\mu}), \tag{2.13}$$

where

$$I_{\mu\mu'} = \frac{1}{8\pi k_B T^2}\int d\omega \tilde{g}^{>}_{\mu}(\omega)\tilde{g}^{<}_{\mu'}(\omega). \tag{2.14}$$

Finally, plugging the RTA's ansatz into Eq. (2.14) yields to:

$$\kappa = \frac{1}{3V}\sum_{\mu\mu'}\frac{n_\mu(n_{\mu'}+1)+n_{\mu'}(n_\mu+1)}{2k_BT^2}\frac{(\omega_\mu+\omega_{\mu'})^2}{4}|v_{\mu\mu'}|^2\tau_{\mu\mu'}, \tag{2.15}$$

where

$$\tau_{\mu\mu'} = \frac{\gamma_\mu+\gamma_{\mu'}}{(\omega_\mu-\omega_{\mu'})^2+(\gamma_\mu+\gamma_{\mu'})^2}, \tag{2.16}$$

is the generalized lifetime matrix, whose diagonal $\mu = \mu'$ contains the lifetimes of the normal modes.

Due to the Lorentzian definition of the generalized lifetime, only quasi-degenerate pair of normal modes, i.e. $|\omega_\mu - \omega_{\mu'}| \lesssim \gamma_\mu + \gamma_{\mu'}$, can contribute to the thermal conductivity. This allows for further simplification, defining the generalized modal specific heat as in Ref. [26]:

$$\begin{aligned} C_{\mu\mu'} &= \frac{\hbar^2\omega_\mu\omega_{\mu'}}{T}\frac{n_\mu - n_{\mu'}}{\hbar(\omega_{\mu'}-\omega_\mu)} \\ &\approx \frac{n_\mu(n_{\mu'}+1)+n_{\mu'}(n_\mu+1)}{2k_BT^2}\frac{(\omega_\mu+\omega_{\mu'})^2}{4}, \end{aligned}$$

which reduces to the modal contribution to the isochoric specific heat $C_\mu = \hbar\omega_\mu\frac{\partial n_\mu}{\partial T}$ when $\omega_\mu = \omega_{\mu'}$. Finally, one obtains the QHGK formula for lattice thermal conductivity:

$$\kappa^{QHGK} = \frac{1}{3V}\sum_{\mu\mu'}C_{\mu\mu'}|v_{\mu\mu'}|^2\tau_{\mu\mu'}. \tag{2.17}$$

The QHGK formula simplifies in the case of crystals due to the aforementioned block properties of $v_{\mu\mu'}$. In the Bloch basis, it reads:

$$\kappa^{QHGK} = \frac{1}{3V}\left[\sum_{\mathbf{q}s}C_{\mathbf{q}s}|v_{\mathbf{q}s}|^2\tau_{\mathbf{q}s} + \sum_{\mathbf{q}s\neq s'}C_{\mathbf{q}ss'}|v_{\mathbf{q}ss'}|^2\tau_{\mathbf{q}ss'}\right], \tag{2.18}$$

where $C_{\mathbf{q}s} = C_{\mathbf{q}ss}$ is the mode specific heat. For a crystal, it is common to separate the thermal conductivity into the two contributions expressed above. While in the first sum, each phonon appears to contribute independently, the second sum accounts for the contribution of a pair of phonons

with the *same wavevector but different band index*. The two contributions are respectively dubbed *intraband* and *interband* [18, 26]. It is worth mentioning, that in the WBTE framework, borrowing the terminology from quantum optics, they are called respectively *population* and *coherence* contributions [27, 28].

Since Eqs.(2.17)-(2.18) involve either a sum over the modes or a sum over quasi-degenerate pairs of modes, it is useful to resolve the modes' contributions by frequency. Let us define for future discussions the frequency-resolved differential thermal conductivity [26]:

$$\frac{d\kappa}{d\omega} = \frac{1}{3V}\sum_{\mu\mu'} C_{\mu\mu'}|v_{\mu\mu'}|^2\tau_{\mu\mu'}\Delta(\omega-\omega_\mu) \tag{2.19}$$

where $\Delta(\omega)$ is a suitable smearing function, e.g. a Gaussian.

2.4 BRIDGING BETWEEN GLASSES AND CRYSTALS

The QHGK formula expressed by Eq. (2.17) bridges and generalize two time-honored theories which have been used, respectively, for glasses and crystals: the Allen-Feldman theory [23, 24] and the linearized Peierls-Boltzmann Transport Equation in the Relaxation Time Approximation (BTE-RTA).

2.4.1 *Allen-Feldman approach*

The Allen-Feldman approach is the purely harmonic solution of the Green-Kubo equation. As such, it can be obtained as the QHGK limit for vanishing anharmonic linewidths:

$$\kappa^{AF} = \frac{1}{3V}\sum_{\mu} C_\mu D_\mu, \tag{2.20}$$

where D_μ is the mode diffusivity:

$$\begin{aligned} D_\mu &= \pi\sum_{\mu'}|v_{\mu\mu'}|^2\delta(\omega_\mu-\omega_{\mu'}) \\ &= \lim_{\eta\to 0}\sum_{\mu'}|v_{\mu\mu'}|^2\frac{\eta}{(\omega_\mu-\omega_{\mu'})^2+\eta^2} \end{aligned}$$

where η is a positive smearing.

2.4.2 *Peierls-Boltzmann transport equation*

The Peierls-Boltzmann theory is only applied to crystals since it heavily relies on the concept of quasi-particles, the phonons, and their crystal momentum $\mathbf{q}$. In the BTE framework [21, 33], the goal is to find the out-of-equilibrium quasi-particle distribution at the linear order in ∇T

$$\tilde{n}^{\alpha}_{\mathbf{q}s} \approx n_{\mathbf{q}s} + \nabla_\alpha T \psi^{\alpha}_{\mathbf{q}s}$$

and consequently, compute the out-of-equilibrium heat flux defined as in a gas of (quasi-)particles:

$$\begin{aligned} J^{\alpha}_{BTE} &= \frac{1}{V}\sum_{\mathbf{q}s} \hbar\omega_{\mathbf{q}s} v^{\alpha}_{\mathbf{q}s}(\tilde{n}^{\alpha}_{\mathbf{q}s} - n_{\mathbf{q}s}) \\ &= -\sum_{\beta} \kappa^{\alpha\beta}\nabla_{\beta} T. \end{aligned}$$

The Boltzmann Transport Equation allows one to compute the nonequilibrium statistics of the population numbers. At linear order in the perturbation, it reads [21]:

$$\begin{aligned} v^{\alpha}_{\mathbf{q}s}\nabla_{\alpha} T\frac{\partial n_{\mathbf{q}s}}{\partial T} &= \frac{\partial n_{\mathbf{q}s}}{\partial t}|_{\text{scatt.}} \\ &= -\nabla_{\alpha} T\sum_{\mathbf{q}'s'} S_{\mathbf{q}s\mathbf{q}'s'}\psi^{\alpha}_{\mathbf{q}'s'}, \end{aligned}$$

where $S_{\mathbf{q}s\mathbf{q}'s'}$ is the so-called scattering matrix. Combining the previous equations, one obtains the Full solution of the linearized Peierls-Boltzmann Transport Equation (Full-BTE) [33, 34]:

$$\begin{aligned} \kappa^{Full-BTE} &= \frac{1}{3V}\sum_{\mathbf{q}s} C_{\mathbf{q}s} v_{\mathbf{q}s}\lambda_{\mathbf{q}s} \\ &= \frac{1}{3V}\sum_{\mathbf{q}s\mathbf{q}'s'} C_{\mathbf{q}s} v_{\mathbf{q}s} v_{\mathbf{q}'s'} S^{-1}_{\mathbf{q}s\mathbf{q}'s'} \end{aligned} \tag{2.21}$$

where $\lambda_{\mathbf{q}s}$ is the *mean free path* of the associated phonon. If the scattering matrix is assumed to be diagonal $S_{\mathbf{q}s\mathbf{q}'s'} = \delta_{\mathbf{q}\mathbf{q}'}\delta_{ss'}2\gamma_{\mathbf{q}s}$, one obtains the BTE-RTA:

$$\kappa^{BTE-RTA} = \frac{1}{3V}\sum_{\mathbf{q}s} C_{\mathbf{q}s}|v_{\mathbf{q}s}|^2\tau_{\mathbf{q}s}, \tag{2.22}$$

and the mean free path is given by $\lambda_{\mathbf{q}s} = v_{\mathbf{q}s}\tau_{\mathbf{q}s}$.

By direct comparison, it can be observed $\kappa^{BTE-RTA}$ coincides with the so-called intraband term in Eq. (2.18). Intuitively, the intraband term gives the contribution of (quasi-)particles that propagate ballistically between two consecutive scattering events.

Despite their outstanding success, these two approaches are limited to glasses and crystals, respectively. Indeed, the AF theory, being purely harmonic, would diverge when applied to a crystal with a sufficiently dense mesh of wavevectors, also known as q-mesh. The anharmonicity is fundamental to scatter the quasi-particles which otherwise would be able to propagate ballistically indefinitely. On the other hand, the interband term missing from $\kappa^{BTE-RTA}$ is fundamental when disorder breaks down the quasi-particle picture. In particular, when BTE-RTA is applied on glasses, which is commonly done by simulating a disordered supercell with PBCs but including only the Γ point [35] ($\mathbf{q} = (0,0,0)$), the group velocity is null and consequently also $\kappa^{BTE-RTA} = 0$.

The QHGK formula unifies both theories and it is valid for both glasses and crystals. Moreover, the success and the limits of the two theories in their respective fields can be understood in terms of the relative importance between the intraband and interband terms. For a *simple* crystal with few phononic bands, whose separation is on average much greater than the linewidths, the intraband term is dominant. On the other hand, for crystals with a more *complex* band structure, which is generally associated with a large unit cell, the two contributions can be comparable. For instance, this condition has been observed for many perovskites [28, 36]. Finally, in glasses, which can be thought of in principle as a crystal with a diverging number of atoms in the unit cell, only the interband term contributes.

The qualitative and quantitative differences between the AF, BTE, and QHGK approaches are illustrated in Fig. 2.1, through the computation of lattice thermal conductivity for two phases of silicon: amorphous (aSi) and diamond-like (cSi). The atomic configurations and Interatomic Force Constants (IFC) for aSi and cSi are generated following Ref. [26] and Ref. [37], respectively. Specifically, the amorphous sample is prepared using a melt-quench procedure with an empirical Tersoff potential [38], while cSi is studied from first principles using Density Functional Theory (DFT). Additional computational details are provided in App. C.

The anharmonic linewidths γ_μ, used both in the QHGK and BTE formulas, are computed including anharmonicity $\Delta\hat{H} = \hat{H} - \hat{H}^\circ$ up to the third order

$$\begin{aligned}\Delta\hat{H} &= \frac{\hbar^{3/2}}{6}\sum_{\mu\mu'\mu''} K_{\mu\mu'\mu''}(\hat{a}^\dagger_\mu + \hat{a}_\mu)(\hat{a}^\dagger_{\mu'} + \hat{a}_{\mu'})(\hat{a}^\dagger_{\mu''} + \hat{a}_{\mu''}) \\ &= \frac{\hbar^{3/2}}{6}\sum_{\mu\mu'\mu''} \frac{\partial^3 U}{\partial\xi_\mu\partial\xi_{\mu'}\partial\xi_{\mu'}}\hat{\xi}_\mu\hat{\xi}_{\mu'}\hat{\xi}_{\mu''} \end{aligned} \tag{2.23}$$

and using FGR [39]:

$$\begin{aligned}\gamma_\mu = \pi\hbar\sum_{\mu'\mu''}|K_{\mu\mu'\mu''}|^2\Big[\frac{1}{2}(n_{\mu''}+n_{\mu'}+1)\delta(\omega_\mu-\omega_{\mu''}-\omega_{\mu'}) \\ +(n_{\mu''}-n_{\mu'})\delta(\omega_\mu+\omega_{\mu'}-\omega_{\mu''})\Big],\end{aligned} \tag{2.24}$$

where $K_{\mu\mu'\mu''} = \frac{1}{\sqrt{8\omega_\mu\omega_{\mu'}\omega_{\mu''}}}\frac{\partial^3 U}{\partial\xi_\mu\partial\xi_{\mu'}\partial\xi_{\mu'}}$ contains the third derivatives of the potential computed at mechanical equilibrium along the normal mode coordinates ξ.

Fig. 2.1 presents, in the top panel, a comparison between the QHGK and AF approaches for aSi. Both the QHGK and AF results exhibit an increasing trend in lattice thermal conductivity with temperature, which saturates above room temperature. Such a trend is experimentally found for most glasses [40–42], and it is reflected in the mathematical structure of AF theory. Indeed, in Eq. (2.20) only the specific heat depends on the temperature, and in the classical limit, $k_B T \gg \hbar\omega$, it becomes constant $\lim_{T\to\infty} C_\mu \to k_B$. The AF lattice thermal conductivity depends on the artificial smearing parameter η. Due to numerical reasons, if the smearing

is much smaller than the spacing between frequencies, no pair of modes satisfies the condition of the delta function in Eq. (2.20). However, this parameter introduces an unwanted artificial bias in the computation. As better discussed in the next chapters, the magnitude of this bias increases for larger glasses, due to the singular behavior of the AF approach in the bulk limit [37].

On the other hand, the lower panel shows the thermal conductivity of cSi computed using both the QHGK and BTE-RTA approaches. For the crystalline case, κ appears as a decreasing function of temperature, and above 200K it agrees with the phenomenological "Eucken's law" $\kappa \sim 1/T$. Indeed, Eucken's law is the classical limit of BTE-RTA when computed with third-order anharmonicity, Eq (2.24), since in the classical limit $\gamma_\mu \propto T$ and $C_\mu \sim k_B$.

Overall, for a simple crystal as cSi with few, well-separated, bands, the two approaches are practically indistinguishable. The dominance of the intraband term over the interband one for this and other commonly studied crystals could explain the success and longevity of the BTE-RTA approach.

2.5 BEYOND THE SINGLE-MODE RELAXATION TIME APPROXIMATION

Despite its usefulness and success, there are known limits to the validity of the SM and RTA hypotheses. For the former, it is well known [43] that for some crystals, especially but not only in 2D materials, the BTE-RTA underestimates the lattice thermal conductivity at low temperature with respect to the full solution of BTE, Eq. (2.21), as hinted by the lower panel of Fig. 2.1. Regarding the latter, it has been shown that using a better approximation for the greater/lesser Green's function has a non-negligible impact on the thermal conductivity of a ferroelectric material near the critical temperature [32].

2.5.1 *Green-Kubo-Mori-Zwanzig theory of lattice heat conductivity*

The limitations of the SM-RTA can be overcome [18] by Mori-Zwanzig memory-function (MZ) formalism [44, 45] to treat the anharmonic decay of the vibrational normal modes. This approach is referred to as the Green-Kubo Mori-Zwanzig (GKMZ) approach.

The following algebra is considerably simplified by introducing the Kubo inner product [46, 47] between quantum mechanical operators, defined as:

$$\left(\hat{A}, \hat{B}\right) \doteq \int_0^{\frac{1}{k_B T}} d\lambda \, \langle \hat{A}^\dagger(-i\hbar\lambda)\hat{B}\rangle - \langle \hat{A}^\dagger(-i\hbar\lambda)\rangle\langle\hat{B}\rangle, \tag{2.25}$$

where the second product can be dropped if the operators have zero average and the time evolution of operators in the Heisenberg representation can be formally expressed in terms of the exponential of the Liouvillian

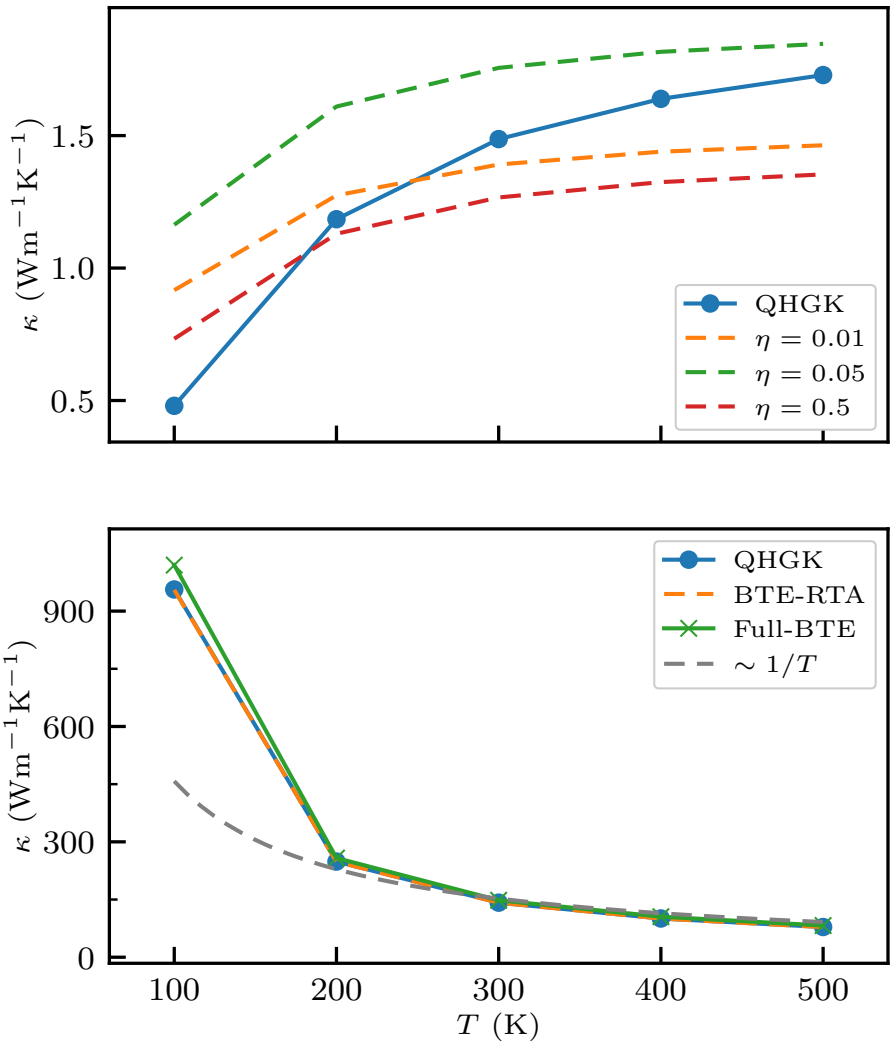

Figure 2.1: Top panel: lattice thermal conductivity of a sample of aSi with $N_{atoms} = 1728$ as a function of temperature. The computation is performed with both the QHGK and AF approaches, the latter repeated for different values of the smearing parameter η in units of rad ps^{-1}. Bottom panel: lattice thermal conductivity of cSi as a function of temperature, using both the QHGK, BTE-RTA and Full-BTE approaches with a dense q-mesh.

super-operator [48], $\mathcal{L}$, defined as $\hat{A}(t) = e^{i\hat{H}t/\hbar}\hat{A}e^{-i\hat{H}t/\hbar} \doteq e^{i\mathcal{L}t}\hat{A}$, and $\mathcal{L}\hat{A} \doteq [\hat{H}, \hat{A}]/\hbar = -i\dot{\hat{A}}$. In terms of this scalar product, the quantum heat conductivity, Eq. (2.2), simply reads

$$\kappa = \frac{1}{3VT}\int_0^\infty dt\ \left(\hat{J}(t), \hat{J}(0)\right),$$

in close formal analogy with its classical counterpart. Moreover, in Hamiltonians invariant under time reversal, it is both convenient and always possible to choose a real basis for the eigenvectors. Indeed, the consequent antisymmetry of the generalized velocity matrix makes the

ordering of equal-time products of bosonic operators —such as, *e.g.*, $\hat{a}^\dagger_\mu(t)\hat{a}_{\mu'}(t)$—irrelevant.

By applying the GK formula, Eq. (2.2), one obtains:

$$\kappa = \frac{\hbar^2}{3VT}\sum_{IJ} v_I v_J \overline{\omega}_I \overline{\omega}_J \overline{G}_{IJ}(0), \tag{2.26}$$

where the indices in capital font $I = (\mu_1, \mu_2)$ and $J = (\mu_3, \mu_4)$ label pairs of normal modes, $\overline{\omega}_I = (\omega_{\mu_1} + \omega_{\mu_2})/2$, $\hat{A}_I = \hat{a}^\dagger_{\mu_1}\hat{a}_{\mu_2}$, and $\overline{G}_{IJ}(0)$ is the zero-frequency value of the Fourier-Laplace transform (FLT), indicated by the $\bar{\cdot}$ symbol, of the two-mode correlation function:

$$\begin{aligned} \overline{G}_{IJ}(z) &= \int_0^\infty dt\, e^{izt} G_{IJ}(t), \text{ and} \\ G_{IJ}(t) &= \left(\hat{A}_I(t), \hat{A}_J\right). \end{aligned} \tag{2.27}$$

Within this framework, the hurdle of solving Eq. (2.2) is mapped into finding an expression for $\overline{G}_{IJ}(z)$, a task that can be effectively tackled by leveraging the MZ memory-function formalism. Indeed, Mori showed in his celebrated 1965 paper [45] that $\overline{G}_{IJ}(z)$ can be formally expressed as:

$$\overline{G}_{IJ}(z) = i\sum_K \overline{\Lambda}^{-1}_{IK}(z) G_{KJ}, \text{ where} \tag{2.28}$$

$$G_{IJ} = G_{IJ}(0), \tag{2.29}$$

$$\overline{\Lambda}_{IK}(z) = z\delta_{IK} - \Omega_{IK} + i\overline{\Gamma}_{IK}(z), \tag{2.30}$$

$$\Omega_{IJ} = i\sum_K \left(\dot{\hat{A}}_I, \hat{A}_K\right) G^{-1}_{KJ}, \tag{2.31}$$

$$\overline{\Gamma}_{IJ}(z) = \sum_K \left(\dot{\hat{A}}_I, \mathfrak{Q}(z - \mathfrak{Q}\mathcal{L}\mathfrak{Q})^{-1}\mathfrak{Q}\dot{\hat{A}}_K\right) G^{-1}_{KJ}, \tag{2.32}$$

and $\mathfrak{Q}$ is the projector over the operator manifold orthogonal to $\mathrm{span}\left(\{\hat{A}_I\}\right)$, defined by its action onto a generic operator, $\hat{B}$, as:

$$\mathfrak{Q}\hat{B} = \hat{B} - \sum_{IJ} \hat{A}_I \left(\hat{A}_J, \hat{B}\right) G^{-1}_{IJ}. \tag{2.33}$$

Intuitively, the MZ formalism separates the evolution of an operator into two distinct parts: one part that preserves the operator's direction (up to a phase factor), and another part that projects the operator onto an orthogonal space, responsible for the loss of correlation (or "decorrelation"). This concept is best understood by considering the time-domain equivalent of Eq. (2.28) for a single operator [45] for $t > 0$:

$$\partial_t G(t) = i\Omega G(t) - \int_0^t dt'\, \Gamma(t - t') G(t'),$$

where the memory function $\Gamma(t - t')$ accounts for the decay of correlation. In the Markovian limit, where $\Gamma(t) \propto \delta(t)$, this decay becomes exponential and resembles the RTA.

2.5.1.1 *The quasi-harmonic limit*

To proceed further, it is necessary to evaluate $\overline{G}_{IJ}(z)$, Eq. (2.28), in the QH approximation, i.e. to leading order in the strength of the anharmonic interactions $\Delta\hat{H}$.

Let us start with G_{IJ}, Eq. (2.29), and Ω_{IJ}, Eq. (2.31), whose leading order in $\Delta\hat{H}$ is $\mathcal{O}(1)$. In the harmonic approximation, one has:

$$\begin{aligned} G^{\circ}_{IJ} &= \int_0^{\frac{1}{k_B T}} d\lambda \langle \hat{a}^{\dagger}_{\mu_2} \hat{a}_{\mu_4} \rangle^{\circ} \langle \hat{a}_{\mu_1} \hat{a}^{\dagger}_{\mu_3} \rangle^{\circ} e^{\hbar\lambda(\omega_{\mu_2} - \omega_{\mu_1})} \delta_{\mu_2\mu_4} \delta_{\mu_1\mu_3} \\ &= \frac{n_{\mu_1} - n_{\mu_2}}{\hbar(\omega_{\mu_2} - \omega_{\mu_1})} \delta_{IJ}, \end{aligned} \tag{2.34}$$

and

$$\Omega^{\circ}_{IJ} = (\omega_{\mu} - \omega_{\mu'})\delta_{IJ}, \tag{2.35}$$

where $\langle\cdot\rangle^{\circ}$ indicates a thermal average in the canonical ensemble of the purely harmonic system. Analogously, $(,)^{\circ}$ defines the "harmonic" Kubo inner product.

From Eq. (2.35) is clear that the harmonic Hamiltonian does not project $\hat{A}$ into the orthogonal space, therefore $\mathfrak{Q}\dot{\hat{A}} \sim O(\Delta\hat{H})$ and the memory matrix $\Gamma \sim O(\Delta\hat{H}^2)$. Consequently, the Λ matrix in Eq. (2.30) has a singularity for degenerate modes $\sim O((\Delta\hat{H})^{-2})$, which is consistent with divergence of the bulk lattice thermal conductivity of harmonic crystals and glasses [25].

To summarize, in the QH limit G_{IJ}, Ω_{IJ} are calculated in the purely harmonic approximation, and the anharmonicity up to order $O(\Delta H^2)$ it must be considered only for Γ_{IJ} [49–52]. Since G°_{IJ} is diagonal in the I, J indices, Eq. (2.28) becomes

$$\begin{aligned} \kappa &= \frac{i\hbar^2}{3VT} \sum_{IJ} v_I v_J \overline{\omega}_I \overline{\omega}_J \overline{\Lambda}^{-1}_{IJ}(0) G^{\circ}_{JJ} \\ &= \frac{i}{3V} \sum_{IJ} C_J v_I v_J \frac{\overline{\omega}_I}{\overline{\omega}_J} \overline{\Lambda}^{-1}_{IJ}(0), \end{aligned} \tag{2.36}$$

where $C_J = \hbar^2 \overline{\omega}_J^2 G^{\circ}_{JJ}/T$ reduces to the generalized modal specific heat in the limit of quasi-degenerate pairs of normal modes.

While being completely general in the QH limit, Eq. (2.36) would require the computation and inversion of a matrix $N^2 \times N^2$, with N being the number of normal modes. Even for systems of moderate size, such an operation would represent a challenging computational hurdle. However, studying Eq. (2.36) in the following cases provides simplifications and valuable insight regarding the connection between the various approaches to compute the lattice thermal conductivity: QHGK, BTE and WBTE.

Until now, the kind of anharmonic potential has not yet been specified. However, in order to quantitatively compare the different approaches, an anharmonic potential truncated at the lowest order (the third one, Eq. (2.23)), is assumed in the following sections.

2.5.2 *The single-mode approximation*

The first case consists of decoupling the correlation functions for different I, J, in the spirit of the SM approximation, by assuming a diagonal structure for $\Gamma_{IJ} = \Gamma_I \delta_{IJ}$. Thus, Eq. (2.36) becomes:

$$\begin{aligned}\kappa &= \frac{i}{3V}\sum_I C_I |v_I|^2 \left(\overline{\Lambda}_{II}(0)\right)^{-1} \\ &= \frac{1}{3V}\sum_{\mu\mu'} C_{\mu\mu'}|v_{\mu\mu'}|^2 \frac{i}{(\omega_{\mu'}-\omega_\mu)+i\overline{\Gamma}_{\mu\mu'}}.\end{aligned}$$

The expression can be symmetrized with respect to $\mu \leftrightarrow \mu'$ exchange, by observing that $\overline{G}_{\mu\mu',\mu\mu'}$ is Hermitian under this exchange. This property is a direct consequence of $A_{\mu\mu'} = A^\dagger_{\mu'\mu}$ and the property of Kubo inner product: $(\hat{A},\hat{B}) = (\hat{A}^\dagger,\hat{B}^\dagger)^*$, which yields to:

$$\int_0^\infty (\hat{A}_{\mu\mu'}(t),\widehat{A}_{\mu\mu'}) = \left(\int_0^\infty (\widehat{A}_{\mu'\mu}(t),\widehat{A}_{\mu'\mu})\right)^*.$$

Thus, by symmetrizing one obtains:

$$\kappa = \frac{1}{3V}\sum_{\mu\mu'} C_{\mu\mu'}|v_{\mu\mu'}|^2 \frac{\overline{\Gamma}'_{\mu\mu'}}{(\omega_\mu-\omega'_\mu-\overline{\Gamma}''_{\mu\mu'})^2+(\overline{\Gamma}'_{\mu\mu'})^2}, \tag{2.37}$$

where $\overline{\Gamma}'_{\mu\mu'} = \mathrm{Re}\,\overline{\Gamma}_{\mu\mu',\mu\mu'}(0)$ and $\overline{\Gamma}''_{\mu\mu'} = \mathrm{Im}\,\overline{\Gamma}_{\mu\mu',\mu\mu'}(0)$.

The above expression closely reminds to QHGK formula, Eq. (2.17). For instance, in both formulas, only modes that are quasi-degenerate with respect to some anharmonic smearing can contribute to thermal conductivity.

However, the similarity is not only formal. Indeed, by assuming a cubic anharmonic potential and after some lengthy calculations (for details see Ref. [18] and App. A.3), one obtains:

$$\overline{\Gamma}'_{\mu\mu'}(z=0) = \overline{\gamma}^{>\,\prime}_{\mu}(\omega_{\mu'})d_{\mu\mu'} + \overline{\gamma}^{<\,\prime}_{\mu'}(\omega_\mu)d_{\mu'\mu} + \mathcal{O}(N^{-1}), \tag{2.38}$$

where $d_{\mu\mu'} = \frac{\beta\hbar(\omega_\mu-\omega_{\mu'})}{e^{\beta\hbar(\omega_\mu-\omega_{\mu'})}-1}$, and $\overline{\gamma}^{\lessgtr}_{\mu}(\omega)$ are the FL transforms of the memory function of the one-body greater/lesser Green's functions, whose expressions as obtained from Mori's formalism [45, 47] are

$$\begin{aligned}\overline{g}^{>}_{\mu}(\omega) &= -\langle \hat{a}_\mu \hat{a}^\dagger_\mu\rangle \frac{1}{(\omega_\mu-\omega)-i\overline{\gamma}^{>}_{\mu}(\omega)}, \\ \overline{g}^{<}_{\mu}(\omega) &= \langle \hat{a}^\dagger_\mu \hat{a}_\mu\rangle \frac{1}{(\omega_\mu-\omega)-i\overline{\gamma}^{<}_{\mu}(\omega)}.\end{aligned} \tag{2.39}$$

Neglecting corrections of order $O(1/N)$ that vanish in the bulk limit, for quasi-degenerate modes one obtains $\overline{\Gamma}'_{\mu\mu'}(z=0) \approx \overline{\gamma}^{>\,\prime}_{\mu}(\omega_{\mu'}) + \overline{\gamma}^{<\,\prime}_{\mu'}(\omega_\mu)$. It can be observed that solving Eq. (2.14) using Cauchy' Residue theorem

with poles around $\sim \omega_\mu$ leads roughly to such result [18]. Therefore, it can be concluded that assuming a diagonal memory matrix in the I, J indices is equivalent to the SM approximation.

Now, let us include the RTA. The latter consists of assuming $\overline{\gamma}$ frequency-independent, and therefore real due to Kramers-Kronig's relations. Then, one obtains that $\Gamma_{\mu\mu'} = \gamma_\mu + \gamma_{\mu'}$, where $\overline{\gamma}^{>'}_{\mu}(\omega_\mu) = \gamma_\mu$, and therefore the QHGK expression, Eq. (2.17).

It must be noted that the addition of the RTA hypothesis on top of the SM approximation does not change significantly the results, as long as $\overline{\gamma}^{\lessgtr}_{\mu}(\omega)$ does not change significantly for ω between ω_μ and $\omega_{\mu'}$. This is a consequence of the quasi-harmonic approximation: whether is Lorentzian or not, the spectrum of the greater/lesser Green's function is still expected to peak around their harmonic frequency. For highly anharmonic materials Green's functions can wildly differ from the harmonic case [32, 53, 54], resulting in Eq. (2.14) being significantly different from its RTA equivalent [32]. However, in the highly anharmonic case, anharmonic corrections to the energy flux can not be excluded *a priori* and that is beyond the scope of this work.

2.5.3 *From Green-Kubo to the full Boltzmann transport equation*

The previous section explains the SM-RTA in the framework of the MZ formalism, showing an alternative derivation of the QHGK formula. Still, as previously mentioned, the QHGK formula is not able to fully capture some proprieties of the lattice thermal conductivity of crystals, which are instead captured by the Full-BTE [34, 43]. In order to understand the origin of this discrepancy, it is necessary to go beyond the diagonal case of the memory matrix.

Firstly, let us re-write Eq. (2.36) for the crystalline case, taking into account the aforementioned block structure of the generalized velocity matrix:

$$\kappa = \frac{i}{3VT} \sum_{\mathbf{q}\mathbf{k}ss'tt'} C_{\mathbf{k}tt'} v_{\mathbf{q}ss'} v_{\mathbf{k}tt'} \frac{\overline{\omega}_{\mathbf{q}ss'}}{\overline{\omega}_{\mathbf{k}tt'}} \overline{\Lambda}^{-1}_{\mathbf{q}ss',\mathbf{k}tt'}(0), \tag{2.40}$$

where s, t, s', t' are band indices. Eq. (2.40) has a more complex and general structure compared to Eq. (2.21), due to the presence of interband terms $s \neq s', t \neq t'$. However, analogously with the QHGK case, the interband terms can neglected in the case of well-separated bands. Intuitively, as Ω° grows with the separation between bands, it dampens the corresponding element of $\overline{\Lambda}^{-1}$. For a formal proof see App. A.2.

By neglecting the interband terms, Eq. (2.40) becomes:

$$\kappa = \frac{1}{3V} \sum_{\mathbf{q}s\mathbf{q}'s'} C_{\mathbf{q}s} v_{\mathbf{q}s} v_{\mathbf{q}'s'} (S^{MZ})^{-1}_{\mathbf{q}s\mathbf{q}'s'}, \tag{2.41}$$

where

$$S^{MZ}_{\mathbf{q}s\mathbf{q}'s'} = \overline{\Gamma}_{\mathbf{q}'s'\mathbf{q}s} \frac{\omega_{\mathbf{q}'s'}}{\omega_{\mathbf{q}s}} \tag{2.42}$$

is a scattering matrix. Indeed, when computed for a cubic anharmonic potential, the scattering matrix just defined coincides [18] with the one in the Full-BTE case [33, 34]. For details see App. A.3.

2.5.4 *Comparison with the Wigner-Boltzmann transport equation*

As in the SM-RTA case, the solution of the GK extends its BTE counterpart by the presence of interband terms. Still, the computation on the interband terms in Eq. (2.41) appears to be more challenging than in Eq. (2.18). Such complication can be treated following the example of WBTE. As explained in Ref. [55], leveraging a common approximation for the Lindblad's equation, the scattering of $\hat{a}^\dagger_{\mathbf{q}s}\hat{a}_{\mathbf{q}s'}$ pairs with $s \neq s'$, called *coherences* in the WBTE framework, can be treated at the SM-RTA level, even if the *populations* $\hat{a}^\dagger_{\mathbf{q}s}\hat{a}_{\mathbf{q}s}$ are treated taking full account of the scattering matrix. By adopting this approximation, Eq. (2.40) becomes:

$$\kappa^{\mathrm{I-QHGK}} = \kappa^{\mathrm{Full-BTE}} + \frac{1}{3V}\sum_{\mathbf{q}s\neq s'} C_{\mathbf{q}ss'}|v_{\mathbf{q}ss'}|^2\tau_{\mathbf{q}ss'}, \tag{2.43}$$

which is here labeled I-QHGK as it involves the inverse of the scattering matrix. This formula is analogous to the WBTE expression [17, 27, 28]:

$$\kappa^{\mathrm{WBTE}} = \kappa^{\mathrm{Full-BTE}} + \frac{1}{3V}\sum_{\mathbf{q}s\neq s'} \frac{\omega_{\mathbf{q}s'}+\omega_{\mathbf{q}s}}{4}\left(\frac{C_{\mathbf{q}s}}{\omega_{\mathbf{q}s}}+\frac{C_{\mathbf{q}s'}}{\omega_{\mathbf{q}s'}}\right)|v_{\mathbf{q}ss'}|^2\tau_{\mathbf{q}ss'}, \tag{2.44}$$

where $v_{\mathbf{q}ss'} = \frac{2\sqrt{\omega_{\mathbf{q}s}\omega_{\mathbf{q}s'}}}{\omega_{\mathbf{q}s}+\omega_{\mathbf{q}s'}}v_{\mathbf{q}s's}$, assuming that $v_{\mathbf{q}ss'}$ is computed in the "smooth convention" [28]. The two formulas differ in the interband term by negligible corrections of order $\mathcal{O}(\gamma^2/\omega^2)$, as it has been numerically verified for a variety of systems [17]. This proves that, as long as the same level of approximation is employed, the WBTE and QHGK are equivalent, in line with Ref. [17] and previous work for the electrical conductivity as reported, for instance, in the Mahan's textbook [56].

2.5.5 *Application to* Li_3ClO *anti-perovskite*

Finally, the proposed theory is tested on lithium-rich anti-perovskite Li_3ClO, a promising candidate for all-solid-state lithium-metal batteries, whose transport properties have been recently investigated using state-of-the-art techniques [57].

Fig. 2.2 displays the thermal conductivity of Li_3ClO as a function of temperature for the different approaches, with the lower panel highlighting the relative variation to the BTE-RTA approach. Computational details are available in App. C.

Two distinct regimes can be identified, depending on the temperature. At lower temperatures, the interband term is negligible, while fully accounting for the scattering matrix significantly increases the thermal

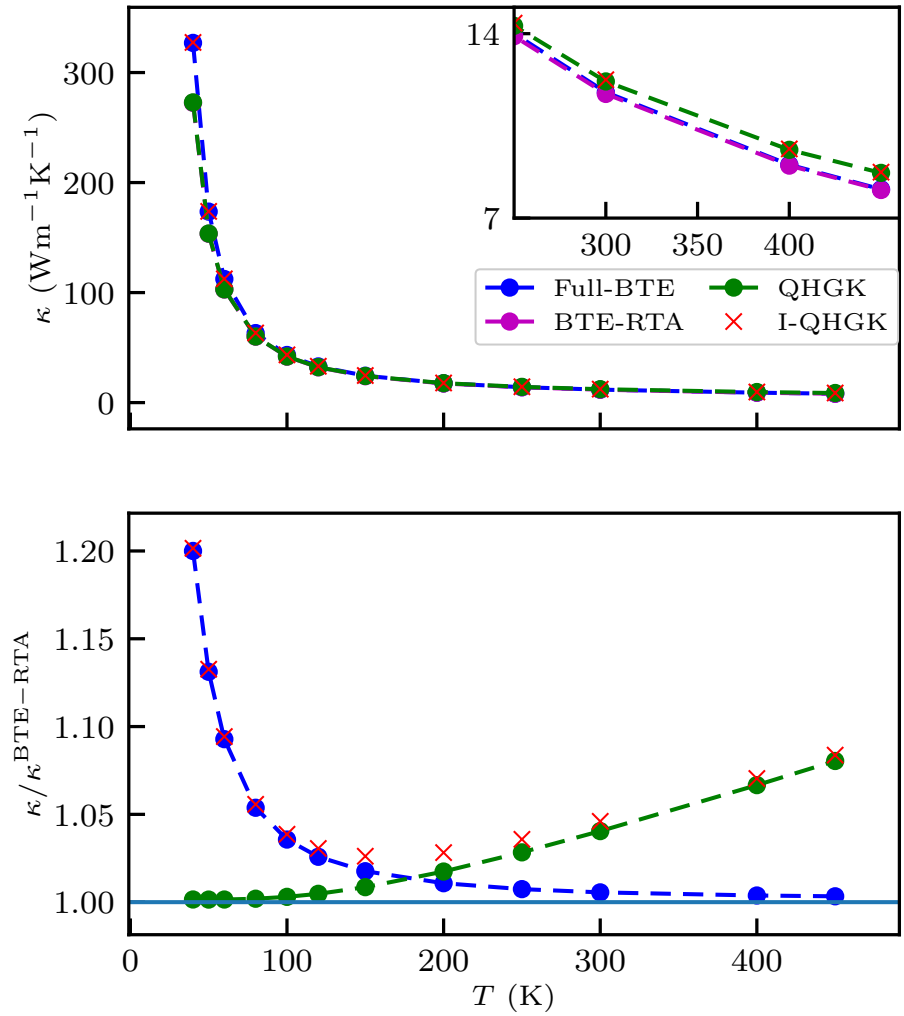

Figure 2.2: Top panel: Thermal conductivity of Li_3ClO as a function of temperature, computed using different approaches. Inset: Close-up of the region around room temperature. Bottom panel: Ratio of thermal conductivity computed with other methods to the BTE-RTA results, as a function of temperature.

conductivity: $\kappa^{\mathrm{BTE-RTA}}, \kappa^{\mathrm{QHGK}}$ and $\kappa^{\mathrm{Full-BTE}}, \kappa^{\mathrm{I-QHGK}}$ coincide separately. However, at room temperature and above, the interband term becomes significant while the SM-RTA does not influence the results.

The different and almost opposite temperature dependencies of the SM-RTA violation and the interband term are due to their physical origins. In brief, the former is generally attributed to *normal* three-phonon scattering of acoustic phonons in the linear dispersion regime, i.e. as $\mathbf{q} \to 0$. Normal scattering processes conserve crystal momentum among the three involved phonons $\mathbf{q} \leftrightarrow \mathbf{q}' + \mathbf{q}''$, whereas Umklapp ones conserve crystal momentum modulo a reciprocal lattice vector $\mathbf{G} \neq 0$. Under normal scattering, the energy flux carried by acoustic phonons, which dominate at low temperatures, is effectively proportional to crystal momentum and is thus conserved [34, 43], whereas a SM-RTA approach

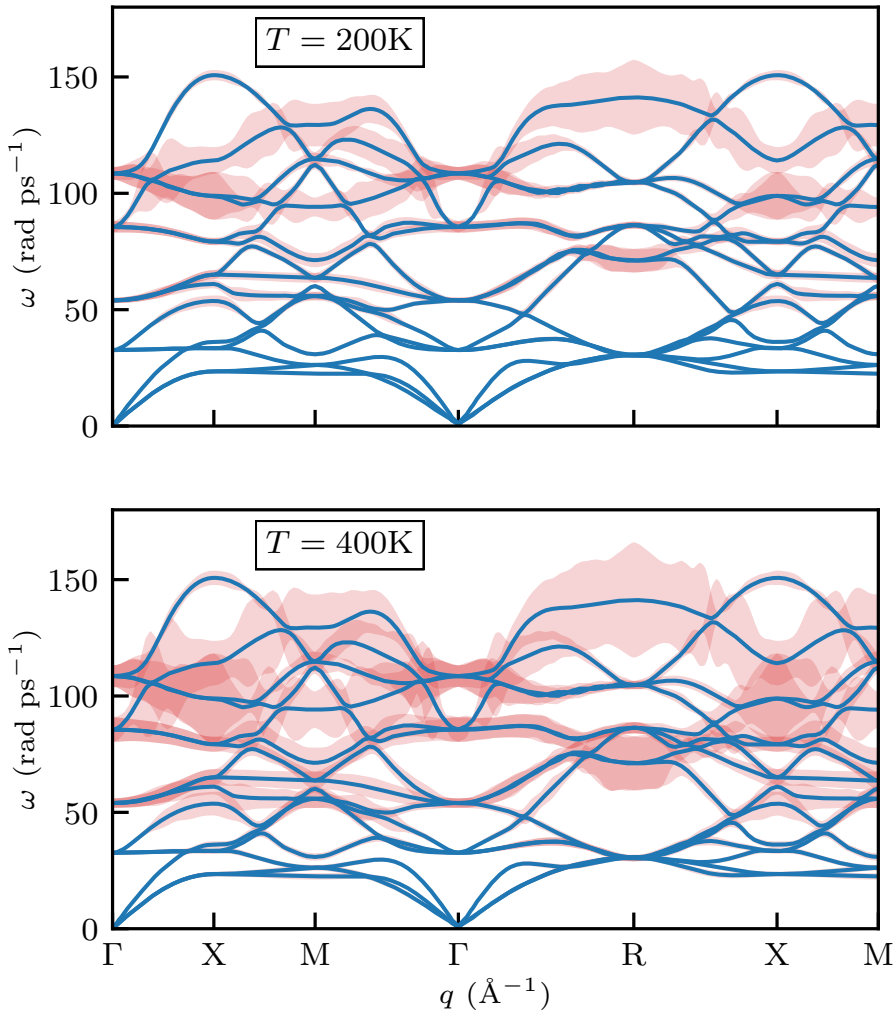

Figure 2.3: Phonon dispersion of Li_3ClO along high-symmetry points, including anharmonic broadening set to 3 times $\gamma_{\mathbf{q}s}$. The anharmonic linewidths are computed at $T = 200, K$ (upper panel) and $T = 400, K$ (lower panel).

would still predict a decorrelation time of the order of the phonon anharmonic lifetimes. On the other hand, the interband term requires the interband spacing to become comparable to the anharmonic linewidths, the latter being typically an increasing function of temperature. For instance, in the classical regime of a cubic anharmonic potential, the linewidth scales approximately as $\gamma \propto T$. This is evident in Fig. 2.3, which shows the anharmonic broadening of the band dispersion at $T = 200$ K and $T = 400$ K. Furthermore, since γ must vanish for $\mathbf{q} \to 0$ faster than the angular frequency for hydrodynamic reasons [58], the interband contribution is typically confined to phonons in the optical frequency range, whose population becomes significant at higher temperatures.

To summarize, using the MZ formalism allows for a deeper understanding and analysis of the approximations underlying the unified

quasi-harmonic Green-Kubo approach to heat transport in both glasses and crystals. Additionally, by going beyond the SM-RTA, it becomes possible to bridge the QHGK approach with various formulations of the BTE. This comparison emphasizes the absence of interband terms in the quasi-particle framework of the BTE. Finally, the quantitative impact of these different approaches and approximations is numerically assessed across multiple systems, Figs. 2.1-2.2.

3

HYDRODYNAMICS OF GLASSES

Unified lattice dynamical theories of thermal transport, such as QHGK [26] and WBTE [27], have brought considerable advancements to the field. Despite these advances, the numerical simulation of heat transport in glasses remains a formidable challenge. In this chapter, the problem of reaching the bulk thermal conductivity of glasses is addressed by leveraging hydrodynamic arguments [35] and efficient numerical techniques [25]. Through numerical experiments and theoretical analysis, I examine how anharmonicity regularizes the singularity observed in harmonic models of heat transport in glasses. Finally, the application of machine learning potentials to this field is briefly discussed. The theoretical findings are supported by numerical experiments performed for three paradigmatic classes of glass (amorphous silicon carbide, silica, and silicon).

We underline that theories such as QHGK and WBTE apply only above the so-called *plateau* in the thermal conductivity as a function of temperature, which is observed in many glassy materials. The temperature dependence of κ in glasses features three universal characteristic trends [59]: at very low temperatures, i.e. $T \lesssim 2\,K$, the dominant scattering mechanism is the quantum tunneling between different local minima in the glass energy landscape, and $\kappa \sim T^2$ [60–62]; then, up to $\approx 30\,K$, the thermal conductivity rises and saturates to a plateau value. Despite the absence of an established theoretical agreement in the literature, this phenomenon seems to be related to the crossover between the regime dominated by quantum processes and one where propagating waves are scattered by disorder [59, 61–63]. Above the plateau, the behavior of κ is dictated by the third-order anharmonic decay of normal modes as prescribed by the QHGK theory. Since we do not have access to the quantum-tunneling between quasi-degenerate minima that play a crucial role at low temperatures, in this work we focus on the third regime.

3.1 STRIVING FOR THE BULK LIMIT

Striving for an estimate of the bulk thermal conductivity, large finite models are used, comprising up to several thousand atoms [26, 64–66]. One limiting factor in pursuing larger sizes is the diagonalization of the dynamical matrix and its poor (cubic) scaling with the number of atoms N. While samples with several thousand atoms already constitute a considerable computational effort, such a size is about one or even two orders of magnitude smaller than the size of a typical simulation for a crystalline

material. In such cases, lattice periodicity and the Bloch theorem can be exploited to map the simulation of a large model onto a number of independent computations performed for the vibrations of definite wavevectors in the BZ, $\mathbf{q}$, of a unit cell comprising a much smaller number of atoms. These wavevectors are usually arranged in a regular grid whose number of nodes is the ratio between the total number of atoms in the bulk model and the number of atoms in the unit cell. The effective model that can thus be afforded has a linear dimension $L \sim 2\pi/q_{min}$, with q_{min} being the discretization step of the regular grid in the BZ.

Since glasses are also simulated with PBCs, like crystals, it could be tempting to apply a similar strategy to glasses. However, simply repeating a disordered cell induces a spurious order on a scale larger than the size of the original cell, leading to an overestimate of the lattice thermal conductivity, both in MD simulations [67, 68] and lattice-dynamical ones [35, 55].

To address these issues, a method has recently been developed [35] that efficiently and accurately extrapolates the value of the thermal conductivity of aperiodic solids, such as glasses, to infinite size, without artificially introducing nonphysical normal modes, which can grossly overestimate the final result. This method, the so-called *hydrodynamic extrapolation*, leverages hydrodynamic arguments, which exploit the natural partitioning of glassy normal modes into categories based on their propagating properties [69]: *propagons*, delocalized low-frequency vibrations with wavelengths much larger than the interatomic distance, propagate almost freely as plane (sound) waves; *locons*, high-frequency vibrations localized in real space, barely contribute to thermal transport; and *diffusons*, intermediate-energy vibrations, are spatially extended and spread diffusively. The existence and properties of propagons can be interpreted from a hydrodynamic perspective. In the long-wavelength limit, sound propagation is described qualitatively in the same way between crystals and glasses, i.e. through the hydrodynamic equations. In crystals, the continuum picture is connected to the atomistic one through the acoustic phonons. Analogously, in glasses, we expect sound waves to be decomposed into long-lived delocalized normal modes: the propagons.

Being long-wavelength vibrations, propagons are severely affected by the finite size of the cell. In fact, similarly to the crystalline case, the size of the system sets a lower bound to the minimum frequency accessible to the calculation, which roughly goes as $\sim 1/L$, where L is the side of a cubic sample. Moreover, it determines the normal-mode spacing in the low-frequency region, which is already undersampled with respect to other portions of the spectrum, due to the vanishing of the Vibrational Density of States (VDOS) in the zero-frequency limit [26, 33, 70]. The undersampling is a relevant issue for both the AF and QHGK approaches, where an insufficient spacing, compared with their respective smearing, leads to an underestimate of the thermal conductivity [25].

The hydrodynamic extrapolation technique solves these problems with two ingredients that can be computed inexpensively. The first is the

QHGK contribution of diffusons and locons from samples of moderate size. The second is a Debye-like model for the propagons contribution in the bulk limit, whose parameters are obtained by the Vibrational Dynamical Structure Factor (VDSF) [35, 71], which can be affordably computed using the Haydock's algorithm [72, 73] even on very large models ($N \gtrsim 10^5$). It is important to note that the hydrodynamic extrapolation applies only above the previously mentioned *plateau* of thermal conductivity, at $T \gtrsim 30\,K$. This limitation arises because the hydrodynamic extrapolation does not inherently account for quantum tunneling between quasi-degenerate minima in the glass energy landscape, which is believed to cause the plateau commonly observed at a few tens of kelvins in most glasses [60, 74–78].

The ability to compute the bulk limit is not only beneficial on the quantitative side, but it has also qualitative and theoretical consequences. For instance, it highlights the importance of the anharmonicity in glasses. Indeed, under general assumptions [79, 80], the scattering due to harmonic disorder in the vanishing frequency limit has a Reyleigh-like scaling $\sim \omega^4$, which alone is not sufficient to guarantee a finite bulk lattice thermal conductivity [24, 25]. Consequently, the purely harmonic Allen-Feldman approach typically shows an infrared singularity in the bulk limit.

On the theoretical side, this singularity was removed by assuming a residual effect of the quantum tunneling even at higher temperatures where typically quantum effects disappear [24]. Even admitting that quantum effects could survive at hundreds of kelvins, this approach has hardly been pursued in the literature on numerical applications of the AF theory, where the singularity is customarily regularized without relying on any such tunneling effects. However, it has been recently shown [25] how perturbative anharmonic effects, as in the QHGK approach, are sufficient to guarantee a finite bulk thermal conductivity at any finite temperature, without invoking quantum tunneling effects. On the computational side, the effects of the singularity on the AF computations have been long overlooked for different reasons. Firstly, the diverging infrared contribution of AF calculations, which is eliminated in small samples due to finite-size effects, is often very small when perturbative anharmonic effects are accounted for, although there are some notable exceptions. The second reason is related to the comparison with thin-film experiments [42, 81–84]. Indeed, the smearing in the AF formula, Eq. (2.20), can formally and sometimes quantitatively reproduce the boundary scattering intrinsic to thin-film experiments, therefore producing in some occasions a spurious experimental validation.

3.1.1 *The acoustic infrared cutoff*

Accelerating the size-convergence of thermal conductivity in glasses requires addressing the main limiting factors.

Excluding the three trivial translational modes at $\omega = 0$, the first significant factor is the presence of an acoustic infrared cutoff. This cutoff

scales as $\sim 2\pi c/L$, where L is the characteristic size of the system and c is the sound speed, which differs between longitudinal and transverse acoustic waves. In the long-wavelength limit, both types of materials exhibit sound waves with linear dispersion, $c|\mathbf{Q}|$, consistent with Goldstone's theorem [70]. For glasses, this infrared cutoff reduces the contribution to thermal conductivity, especially at lower temperatures, where only modes with $\hbar\omega \sim k_B T$ are significantly populated, following the Bose-Einstein distribution. The impact of this cutoff is generally smaller for crystals, as their periodicity allows for the simulation of much larger systems compared to glasses, thereby mitigating the effects of the cutoff.

3.1.2 *The smearing problem*

The second factor is more subtle and primarily numerical in nature, though its effect can be significant despite often being overlooked. This issue, here termed the *smearing problem*, arises from the requirement in both the QHGK and AF approaches for a "dense" vibrational density of states (VDOS). The degree of this density depends on the smearing parameter, which is γ_μ for QHGK and η for AF. As a rule of thumb, one aims to satisfy the condition

$$3N\rho(\omega)\Delta\omega \sim 1,$$

where $\rho(\omega)$ represents the VDOS (normalized to the unity) and $\Delta\omega$ denotes the smearing, whether for the AF or QHGK approach. This phenomenon is visible in the AF data for a fixed size L, as shown in 3.7 (or Fig. B.3 in App. B.2), where the thermal conductivity $\kappa^{AF}(\eta, L)$ decreases sharply when η falls below a critical value. In 3D materials with linear mode dispersion, the VDOS scales quadratically with frequency at low values, $\rho(\omega) \sim \omega^2$, consistent with the Debye model. As the frequency approaches zero, the modes become increasingly sparse, making it difficult to satisfy the smearing requirement.

Let us now estimate the cutoff frequency resulting from this constraint. For AF with a fixed η, assuming a quadratic VDOS, the smallest angular frequency satisfying the smearing condition is given by:

$$\omega_{\text{crit}}^{\text{AF}} \sim \sqrt{\frac{1}{3N\eta}} \sim \frac{1}{L^{3/2}}.$$

Since the acoustic cutoff due to the system size scales as $1/L$, the effective minimum frequency contributing to thermal conductivity, defined as the maximum of these two cutoffs, is typically determined by the former one. However, this is not necessarily the case for QHGK. Suppose, for example, that the anharmonic linewidths scale as $\gamma_\mu \sim A(T)\omega_\mu^{1+\alpha}$, where $\alpha > 0$ and $A(T)$ is a temperature-dependent coefficient. In this scenario, the critical frequency for QHGK becomes

$$\omega_{\text{crit}}^{\text{QHGK}} \sim \left(\frac{1}{3NA(T)}\right)^{1/(3+\alpha)} \sim \frac{1}{L^{3/(3+\alpha)}}.$$

For sufficiently large QHGK simulations, the effective minimum frequency ω_{crit} is determined by the smearing, rather than the system's actual minimum frequency. Importantly, $A(T)$ is typically an increasing function of temperature. As a result, for fixed system size L, the infrared cutoff due to acoustic phonons may dominate at higher temperatures, while the smearing cutoff may become more significant at lower temperatures.

3.1.3 *The pseudo-crystal approach*

Both crystals and glasses are typically simulated in PBCs, thus one would hope to tackle the size problem similarly. However, sampling a q-mesh in glasses mimics an artificial order by adding long-lived modes below this threshold, thus reflecting the spurious periodicity induced by PBCs and determining an artificial increase of the thermal conductivity. Indeed, real glasses below this threshold frequency feature propagating waves whose wavelength is proportional to their inverse frequency, and whose decay depends on disorder [69]. Strictly speaking, a replicated model glass cannot be disordered on a spatial scale larger than the original simulation cell. Thus, the spurious modes whose wavelength is larger than the simulation cell are unaffected by disorder and would propagate for longer times than the corresponding modes in an infinite, actually disordered, glass. In fact, finite wavevectors other than high-symmetry points at the BZ boundary have, in general, a finite group velocity, resulting in Eq. (2.18). The resulting intraband/BTE-RTA contribution due to the finite group velocity is crystalline-like and describes modes whose decay depends only on anharmonicity. Unsurprising, this yields to an overestimate of the thermal conductivity. This has been recently observed in Ref. [66], where a $3 \times 3 \times 3$ q-mesh is shown to determine a low-temperature divergence of the thermal conductivity of amorphous silica systems. The same does not happen for a genuinely disordered system with an equivalent number of atoms (i.e., 3^3 times the number of atoms of the small model) sampled at the Γ point; for such a system the thermal conductivity is a monotonically increasing function of temperature [66]. Similar results are shown in Ref. [35] also for other glasses. The unphysical increase of thermal conductivity due to this approach has also been observed in MD simulations of glasses [67, 68].

3.1.3.1 *An alternative pseudo-crystalline approach*

A recently proposed method leverages the *pseudo-crystalline* approach to glasses while avoiding the drawback of overestimating thermal conductivity by employing a so-called *regularization* procedure [66]. This overestimation, caused by the artificial crystalline order introduced by periodic replicas of the fundamental simulation cell, is mitigated by convolving the QHGK/WBTE Lorentzian lineshape of the unphysical low-frequency modes with a smearing function. The width of this smearing function, η, is carefully selected as described below. While choosing the smearing

function to be Lorentzian would result in a Lorentzian smeared lineshape whose width would be the sum of the original and smearing linewidths $\gamma_\mu \rightarrow \gamma_\mu + \eta$, it was found that using a Gaussian smearing function would lead to slightly better numerical behavior of the procedure. Of course, the heat conductivities computed with this method depend on the smearing width, and they would in fact diverge, in the low-temperature limit and even for finite samples, for vanishing smearing. In Ref. [66] the choice of the smearing width was somewhat justified by the existence of a plateau in the dependence of the heat conductivity on it. When such a plateau exists, the width so chosen should be a compromise between a large enough value allowing to encompass several normal modes and small values necessary not to mimic spuriously large scattering sources.

In a nutshell, this protocol forces the QHGK (or, equivalently, WBTE) method for a pseudo crystal—whose unit cell is the whole simulation representing the glass model—to behave like the AF model for low-frequency modes whose linewidths are smaller than the smearing width—i.e., the modes responsible for the unphysical overestimate of κ—while doing almost nothing to modes with higher frequency/larger linewidth.

The regularization procedure has significant flaws, as reported in Ref. [35]. For αSiO_2 at room temperature, a plateau is observed in the thermal conductivity as a function of the smearing parameter and it is possible to obtain from a smaller sample results compatible with a genuine larger glass. However, no such plateau is found for αSi and αSiC [35]. Moreover, at low temperatures, when $\gamma_\mu \ll \eta$, the technique reproduces the AF results [66] with a fixed η. However, as explained later, this differs significantly from the genuine bulk limit of QHGK (or WBTE) at low temperatures.

3.2 HYDRODYNAMIC FINITE-SIZE SCALING OF THE THERMAL CONDUCTIVITY IN GLASSES

In order to properly estimate the bulk limit of heat conductivity in glasses without relying on pseudo-crystalline approaches, one must devise a suitable finite-scaling technique based on genuine glass samples simulated with PBCs, but at the Gamma point, $\mathbf{q} = (0, 0, 0)$.

Naively, to deal with finite-size effects one should compute the thermal conductivity for samples with increasing size, L, up to convergence $\lim_{L\to\infty} \kappa(L, T) = \kappa_\infty(T)$. The simplest way to extrapolate $\kappa_\infty(T)$ from the finite size samples would be to assume that for each temperature $\kappa(L)$ can be expanded in a power series of $1/L$ and then perform a linear fit in L. However, there are different flaws in this procedure: firstly, the simulation must be repeated for different sizes–at least three to meaningfully fit a straight line; secondly, if $1/L$ is too small for the linear contribution to be dominant, higher powers are needed, introducing further parameters, thus increasing the number of data points required and the complexity of the extrapolation. In the following, we present a physically motivated technique to bypass these challenges.

3.2.1 *Propagons, diffusions, and locons*

The hydrodynamic extrapolation method is physically grounded in the natural partitioning of vibrational modes in glasses into propagons, diffusons, and locons, as previously discussed [69, 71]. These features are evident in the VDSF, which, for a harmonic system, is defined as [71]:

$$S^{\circ}_{b}(\omega, \mathbf{Q}) = \sum_{\mu} \delta(\omega - \omega_{\mu}) |\langle \mu | \mathbf{Q} b \rangle|^2, \tag{3.1}$$

where $|\mathbf{Q}b\rangle$ is a plane-wave-like vibrational state, whose projection on the displacement of the Ith atomic site in the α Cartesian direction is:

$$\langle I\alpha | \mathbf{Q}b \rangle = \frac{1}{\sqrt{N}} \varepsilon^{b}_{\alpha}(\mathbf{Q}) e^{i\mathbf{Q}\cdot\mathbf{R}_I}, \tag{3.2}$$

with $\mathbf{Q} = \frac{2\pi}{L}(n, m, l)$, where $n, m, l \in \mathbb{N}$ denote a wavevector in a cubic supercell of side L; $\mathbf{R}_I$ represents the equilibrium position of the Ith atom; and $\boldsymbol{\varepsilon}^{b}(\mathbf{Q})$ is a polarization (unit) vector. Consequently, the scalar product with the eigenvector of the μth normal mode, $\boldsymbol{e}^{\mu}$, is given by:

$$\langle \mu | \mathbf{Q}b \rangle = \frac{1}{\sqrt{N}} \sum_{I\alpha} \varepsilon^{b}_{\alpha}(\mathbf{Q}) (e^{\mu}_{I\alpha})^* e^{i\mathbf{Q}\cdot\mathbf{R}_I}. \tag{3.3}$$

The polarization of the plane-wave vector can be chosen to be either parallel or perpendicular to $\mathbf{Q}$ and is labeled by $b = L, T_1, T_2$, corresponding to the longitudinal (parallel to $\mathbf{Q}$) and transverse (perpendicular to $\mathbf{Q}$) branches, respectively. . Glasses are typically isotropic, therefore the transverse branches are degenerate, and T indicates the contributions of both transverse branches.

The plane-wave vibrational states are not necessarily a basis for a disordered system, since

$$\langle b\mathbf{Q}' | b\mathbf{Q} \rangle = \frac{1}{N} \sum_{i} e^{i(\mathbf{Q}-\mathbf{Q}')\mathbf{R}_i}$$

is not exactly $\delta_{\mathbf{Q}\mathbf{Q}'}$ if the positions $\mathbf{R}_i$ are not on a lattice . However, if both $Q, Q' < Q_{max}$ such that $2\pi/|Q_{max}|$ is much bigger than the interatomic distance, the medium appears to be homogenous and it has been numerically verified that these vectors, labeled *acoustic plane waves*, are effectively orthonormal. For our purpose of describing the propagons contribution, $|\mathbf{Q}b\rangle$ acts as a basis [85]. More details on App. B.1.

The VDSF can be interpreted as the spectral function of the retarded Green's function (see, for instance, Ref. [56] for details on Green's functions), $S^{\circ}_{b}(\omega, \mathbf{Q}) = \frac{1}{\pi} \mathrm{Im} g^{\circ,R}_{\mathbf{Q}b}(\omega)$, which reads:

$$\begin{aligned} g^{\circ,R}_{\mathbf{Q}b}(t) &= -i(\langle \hat{a}_{\mathbf{Q}b}(t) \hat{a}^{\dagger}_{\mathbf{Q}b} \rangle - \langle \hat{a}^{\dagger}_{\mathbf{Q}b} \hat{a}_{\mathbf{Q}b}(t) \rangle) \Theta(t) \\ &= \sum_{\mu} -i |\langle \mu | \mathbf{Q}b \rangle|^2 e^{-i\omega_{\mu} t} \Theta(t), \end{aligned} \tag{3.4}$$

where $\Theta(t)$ is the Heaviside function and

$$\hat{a}_{\mathbf{Q}b} = \sum_{\mu} \langle \mu | \mathbf{Q}b \rangle \hat{a}_{\mu}.$$

From Eq. (3.4), it is straightforward to account for weak anharmonic effects using the RTA, i.e. $\langle \hat{a}_{\mu}(t)\hat{a}_{\mu}^{\dagger} \rangle \propto e^{-i\omega_{\mu}t - \gamma_{\mu}|t|}$. This yields to

$$S_b(\omega, \mathbf{Q}) = \sum_{\mu} \frac{1}{\pi} \frac{\gamma_{\mu}}{\gamma_{\mu}^2 + (\omega - \omega_{\mu})^2} |\langle \mu | \mathbf{Q}b \rangle|^2, \tag{3.5}$$

Fig. 3.1 shows the VDSF for different glasses, for both the transverse and longitudinal polarization. The low-frequency, small-wavevector, portion of each branch of the VDSF features an almost linear dispersion, $\omega \simeq cQ$, typical of acoustic phonons. In other words, $S_b(\mathbf{Q}, \omega)$ is a peaked function centered at $\omega_Q = c_b Q$, $c_{T,L}$ being the transverse/longitudinal speed of sound. For low-enough Q, the profile of $S_b(\omega, \mathbf{Q})$ can be fitted as a function of the angular frequency with a Lorentzian profile,

$$S_b(\omega, \mathbf{Q}) \approx \frac{A_b(\mathbf{Q})}{\pi} \frac{\Gamma_b(\mathbf{Q})}{(\omega - c_b Q)^2 + \Gamma_b(\mathbf{Q})^2}, \tag{3.6}$$

where $A_b(\mathbf{Q})$ is a normalization factor. This fit allows one to evaluate the speed of sound as well as the wavevector dependence of the effective width, the sound attenuation coefficient $\Gamma_b(\mathbf{Q})$. Under the assumption of isotropy, $S_b(\omega, \mathbf{Q}) = S_b(\omega, Q)$ and, consequently, $\Gamma_b(\mathbf{Q}) = \Gamma_b(Q)$. A similar fit to $S_b^{\circ}(\omega, \mathbf{Q})$ yields $\Gamma^{\circ}(\mathbf{Q})$, representing the disorder contribution to the sound attenuation coefficient within the harmonic approximation. The Lorentzian shape of the VDSF for the propagons suggests they are long-lived excitations, scattered by both harmonic disorder and anharmonicity, which are taken into account by $\Gamma_b(\mathbf{Q})$.

Propagons are defined as those low-frequency, low-wavevector, normal modes with linear dispersion that populate the first portion of the VDSF. At sufficiently large frequencies, the broadening becomes comparable to $c_b Q$, marking a transition frequency between propagons and diffusons, commonly known as the Ioffe-Regel limit [86]. Finally, since locons are localized in real space, they are delocalized in reciprocal space. In the limiting case of a mode $|\mu\rangle$ localized on a single atom $\sum_b \langle \mu | \mathbf{Q}b \rangle|^2 = 1/N$ $\forall \mathbf{Q}$.

Further insight into the properties of propagons can gained from a hydrodynamic perspective. In the long-wavelength limit, the glass can be expected to behave as a continuous, practically homogeneous, medium. In this limit, if the hydrodynamics equations for energy, number, and momentum density are expressed in terms of the displacements density $\mathbf{u}(\mathbf{r}, t) \propto \sum_i u_i(t)\delta(\mathbf{r} - \mathbf{R}_i^{\circ})$, one obtains [58]:

$$\partial_t^2 u_b(\mathbf{r}, t) - c_b^2 \nabla^2 u_b(\mathbf{r}, t) = D_b \partial_t \nabla^2 u_b(\mathbf{r}, t),$$

where D_b are polarization-dependent coefficients and for the longitudinal case $b = L$ the coupling with the energy density is omitted. The

latter is a reasonable assumption if the thermal expansion is negligible, as it happens for a harmonic crystal [58]. By solving these equations with standard methods, one finds that in the hydrodynamic limit $S_{u_b}(\mathbf{Q}, \omega)$, the space-time FT of $\langle u(\mathbf{r}, t)u(0, 0)\rangle$, has the typical acoustic peaks at $\omega = \pm c_b Q$, with width $\sim D_b Q^2$. Given the straightforward connection between S_{u_b} and S_b, as outlined in App. B.1, one can theoretically motivate the ansatz in Eq. (3.6) and expect $\lim_{Q\to 0} \Gamma(Q) \sim Q^2$. The acoustic damping coefficients $\Gamma(Q)$ can be measured with, for instance, inelastic light scattering [87, 88], therefore allowing for experimental validation of the VDSF.

3.2.2 *Hydrodynamic extrapolation*

The hydrodynamic extrapolation can be summarized as follows: firstly, the glass samples of finite size are generated and their IFC computed. Then, the propagon contribution κ_P is separated from the contribution due to diffusons and locons, labeled diffusive contribution κ_D. While κ_D is computed directly with QHGK on the samples, κ_P is computed with a continuous Debye-like model whose parameters are obtained from the VDSF. A graphical summary of the workflow is reported in Fig. 3.2.

The decomposition

$$\kappa = \kappa_P + \kappa_D.$$

is well-defined because, due to the nature of $\tau_{\mu\mu'}$, Eq. (2.16), only quasi-degenerate pairs of modes contribute: propagons only pairs with propagons. Then, we want to rewrite the propagons contribution on the basis of the acoustic plane waves, using our knowledge from the VDSF to compute it efficiently. The main points of the derivation are exposed below, while further details are in the App. B.1.

In the new basis, the propagon contribution to the energy flux, Eq. 2.10 becomes:

$$\hat{J} = \frac{1}{V} \sum_{\mathbf{Q} b b' \in P} J^{bb'}_{\mathbf{Q}} \hat{a}^\dagger_{\mathbf{Q}b} \hat{a}_{\mathbf{Q}b'}, \tag{3.7}$$

where P indicates that sum is restricted to the propagon region and $J^{bb'}_{\mathbf{Q}}$ is the matrix element of $\hat{J}$ in the plane-wave basis. Similarly to the QHGK crystalline case, such matrix elements can be shown to have a block-matrix structure in the wavevector indices

$$J^{bb'}_{\mathbf{Q}\mathbf{Q}'} \approx \delta_{\mathbf{Q}\mathbf{Q}'} J^{bb'}_{\mathbf{Q}} \tag{3.8}$$

and the matrix between the two transverse polarizations, $J^{T_1 T_2}_{\mathbf{Q}} = 0$, can be assumed to be zero due to isotropy.

Another useful property is $\langle \hat{a}^\dagger_{\mathbf{Q}L} \hat{a}_{\mathbf{Q}T} \rangle \approx 0$. This orthogonality is a consequence of the energy separation of the L, T bands, i.e. $|(c_L - c_T)Q| \gg \Gamma_L(Q) + \Gamma_T(Q)$, and the VDSF, from which it can be inferred that

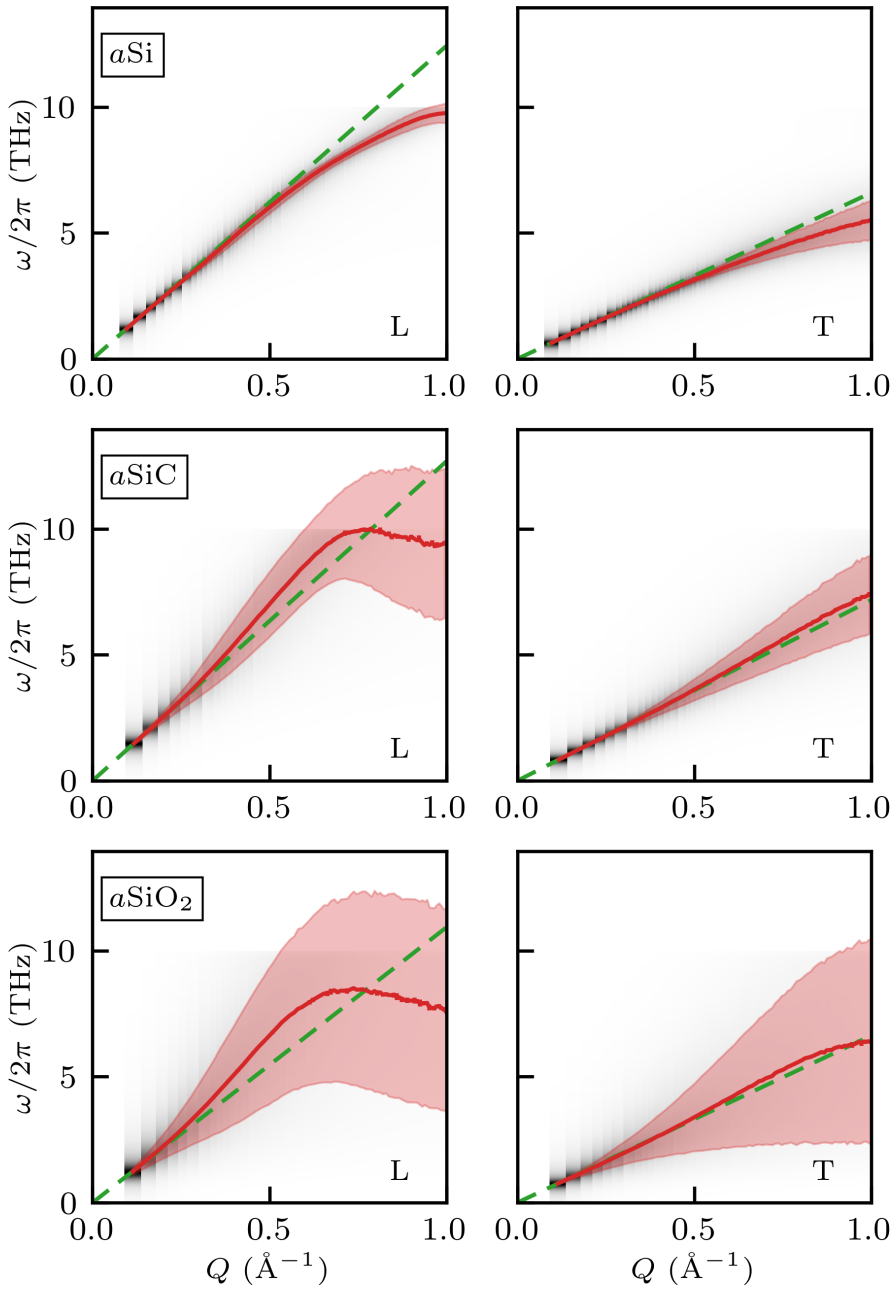

Figure 3.1: Harmonic VDSF, Eq. (3.1), as a function of the angular frequency and the modulus of the wavevectors. For each $\mathbf{Q}$ a Lorentzian fit is applied to $S^{\circ}(\mathbf{Q},\omega)$, whose centers and widths, $\omega_{\mathbf{Q}}$ and $\Gamma_{\mathbf{Q}}$, are indicated on top of the VDSF. The green line is a linear fit of the first few $\omega_{\mathbf{Q}}$. Left to right: longitudinal and transverse polarization. Top to bottom: aSi, aSiC and $a\mathrm{SiO_2}$. Smearing parameter $\eta = 1$ (rad ps^{-1})

$\langle \mu|\mathbf{Q}b\rangle$ is significantly different from zero only if $\omega_\mu \approx c_b|\mathbf{Q}| \pm \Gamma_{\mathbf{Q}b}$. The reasons for the energy separation are two-fold: firstly, in 3D materials $c_L > \sqrt{4/3}c_T$ [89], and secondly propagons are, by definition, modes with a sharp linear dispersion relation, i.e., $c_b Q \gg \Gamma_b(Q)$. The sharpness in-

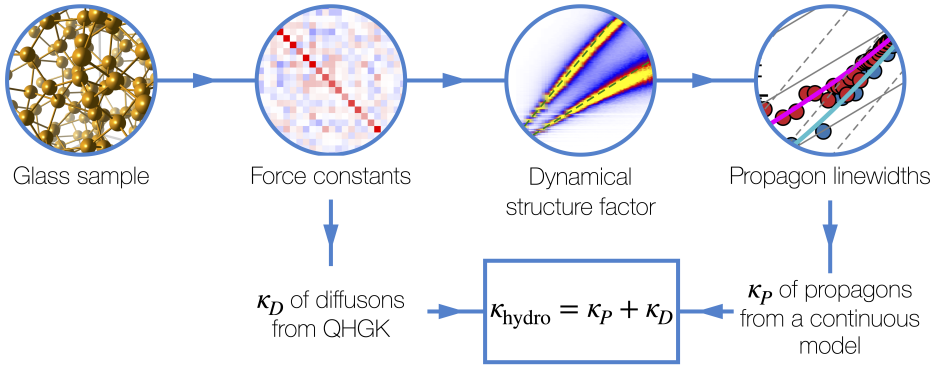

Figure 3.2: Graphical summary of the workflow necessary to implement the hydrodynamic extrapolation of the heat conductivity. Picture drawn from Ref. [35].

creases for smaller wavevectors as $\Gamma_b(Q)$ must vanish faster than linearly for $Q \to 0$ for hydrodynamic reasons [58, 90].

By combining these properties and Eq. (3.4)-(3.5), one obtains the greater Green's function of these acoustic modes:

$$\begin{aligned} g^{>}_{\mathbf{Q}bb'}(t) &= -i\langle \hat{a}_{\mathbf{Q}b}(t)\hat{a}^{\dagger}_{\mathbf{Q}b'}\rangle \\ &\approx -i\delta_{bb'}\frac{1}{2\pi}\int d\omega\, e^{-i\omega t}\frac{1}{\pi}\mathrm{Im}g^{R}_{\mathbf{Q}b}(\omega))(n(\omega,T)+1) \\ &\approx -i\delta_{bb'}\frac{1}{2\pi}\int d\omega\, e^{-i\omega t}S_b(\omega,\mathbf{Q})(n(\omega,T)+1) \\ &\approx -i\delta_{bb'}(n(c_bQ,T)+1)e^{-ic_bQt-\Gamma_b(Q)|t|}. \end{aligned} \tag{3.9}$$

Then, mirroring the derivation of Eq. (2.17) , the propagon contribution can be evaluated from Eq. (3.9), resulting in

$$\kappa_P = \frac{1}{3V}\sum_{\mathbf{Q}b\in P} C(c_bQ)c_b^2\tau_{Qb}. \tag{3.10}$$

The last equation, reminiscent of the BTE-RTA model, defines the lifetimes of acoustic excitations, $\tau_{Qb} = \frac{1}{2\Gamma_b(Q)}$, and the frequency-dependent heat capacity, $C(\omega) = \hbar\omega\frac{\partial n(\omega)}{\partial T}$. In principle, there would be interband terms between the longitudinal and transverse polarization. However, this contribution is negligible if the two bands are energetically well-separated, as it happens for sufficiently small wavevectors due to the more-than-linear scaling of $\Gamma_b(Q)$.

The final step to evaluate the infinite-size limit of κ is to map Eq. (3.10) onto the kinetic theory of gases. The sum over plane waves can be recast as an integral over angular frequency in the $L \to \infty$ limit using the fact that, for propagons, the linear dispersion relation, $\omega = cQ$, is valid, and introducing per-branch densities of states, $\rho_b(\omega) = \frac{1}{V}\sum_{\mathbf{Q}}\delta(\omega - c_bQ)$. This yields:

$$\kappa_P = \sum_{b=L,T} \frac{c_b^2}{3} \int_0^{\omega_P} d\omega \; C(\omega)\rho_b(\omega)\frac{1}{2\Gamma_b(\omega/c_b)}. \tag{3.11}$$

Acoustic excitations feature a density of states of the Debye form, i.e., $\rho_T(\omega) = \frac{\omega^2}{\pi^2 c_T^3}$ and $\rho_L(\omega) = \frac{\omega^2}{2\pi^2 c_L^3}$. Once κ_P is available, one computes the hydrodynamic extrapolation of the thermal conductivity as

$$\kappa_{hydro} = \kappa_P + \frac{1}{3V}\sum_{\mu\mu'} \Theta(\omega_\mu - \omega_P)\Theta(\omega_{\mu'} - \omega_P) C_{\mu\mu'} |v_{\mu\mu'}|^2 \tau_{\mu\mu'}, \tag{3.12}$$

where the second term comes from Eq. (2.17), and the Heaviside-theta limits the sum to the nonpropagonic part of the spectrum. The method can be straightforwardly adapted to the AF model with fixed smearing, by mapping $2\gamma_\mu \to \eta$.

For the model to be valid, ω_P must be chosen in a (angular-) frequency range accessible to the finite sample that satisfies certain requirements. All the normal modes below ω_P should be *bona fide* propagons for both polarizations, so as to avoid a regime where transverse-diffusons and longitudinal-propagons are mixed. Thus, between the transverse and longitudinal Ioffe-Regel angular frequencies, ω_P should be the smaller one, which is generally the transverse one. Slightly lower values may also be preferred to guarantee that all the hypotheses regarding linear dispersion are valid. Studying the dependence of κ_{hydro} on ω_P constitutes a good and inexpensive test to find an appropriate value of ω_P and verify the robustness of the procedure, since κ_{hydro} should be roughly independent on the choice of ω_P as long as it is placed in the mentioned frequency range (see, for instance, the supplementary material of Refs. [35, 37]).

3.2.3 *Low-frequency behavior of the sound attenuation coefficients*

The hydrodynamic extrapolation of heat conductivity requires extrapolating the sound attenuation coefficients $\Gamma_b(\omega/c_b)$ to vanishing frequencies, far below the minimum frequency accessible in glass samples of moderate size. Simply using Eq. (3.10) with lifetimes computed from Eq. (3.5) would offer little advantage, as it would still require the diagonalization of large dynamical matrices. However, there are two reasons that allow the extrapolation. Firstly, the harmonic VDSF can be computed efficiently with Haydock's algorithm illustrated below, without ever needing to compute the eigenvectors of the dynamical matrix. Moreover, by fitting the anharmonic linewidths with respect to the frequency, $\gamma_\mu \approx \gamma(\omega_\mu)$, the anharmonic effects can be effortlessly included. Secondly and most importantly, leveraging theoretical arguments, one can obtain an ansatz for $\Gamma_b(\omega/c_b)$ for vanishing frequencies.

Under general assumptions [79, 80], the low-frequency behavior of the sound attenuation coefficients reads [35, 58, 90]:

$$\Gamma_b(\omega/c_b) \approx A_b\omega^2 + B_b\omega^4, \tag{3.13}$$

where $A_b, B_b > 0$. A model of this form was also proposed in Ref. [84], where the quadratic and quartic terms come, respectively, from the Umklapp and isotopic scattering of long-wavelength phonons in crystalline silicon. More generally, the $\Gamma \sim \omega^2$ trend is required by hydrodynamics [58, 91] and can be explained through the Akhiezer mechanism [92, 93]. On the other hand, the $\Gamma \sim \omega^4$ behavior—also observed in experiments [87, 88]—can be rationalized in the continuous limit through random media theory [94, 95] or, for atomistic models, through harmonic perturbation theory, as in the case of crystals with mass disorder [96, 97] or random spring constants [79, 98]. The crossover between the $\sim \omega^2$ and $\sim \omega^4$ behaviors in the sound attenuation has also been observed in MD simulations [99] and it has also been rationalized by analyzing nonaffine displacements in amorphous solids [90].

While Eq. (3.13) should describe under very general hypothesis the sound attenuation coefficients at very low frequencies [100], it is worth mentioning that for $0 < \omega < \omega_P$ a second crossover $\omega^4 \to \omega^2$ can be observed due to the harmonic disorder. This crossover is illustrated in Fig. 3.5, which displays the computed harmonic sound attenuation coefficients for the three glasses. While all three glasses tend to a Rayleigh scattering for Γ° in the vanishing frequency limit, both aSiC and $aSiO_2$ show a crossover $\omega^4 \to \omega^2$ at a finite angular frequency. This second crossover, observed experimentally for $aSiO_2$ [87, 88], it can be described by the phenomenological function proposed in Ref. [88]:

$$\Gamma_b^\circ(\omega) = C_b\omega^2[1 + (\omega_{XO}^b/\omega)^{2\delta}]^{-1/\delta}, \tag{3.14}$$

where C_b is a constant, ω_{XO}^b is the polarization-dependent crossover angular frequency, and $\delta = 1.5$ determines the sharpness of the transition. As the quartic frequency dependence of the sound attenuation coefficients in harmonic glasses can be understood perturbatively in terms of the scattering of acoustic waves in a homogeneous medium with small, random, independent local fluctuations of the elastic constants [98], the $\omega^4 \to \omega^2$ crossover can be explained with spatially correlated elastic deformation [94, 100]. In a nutshell, assuming a finite correlation length for these fluctuations, vibrations with a wavelength larger than this length, and therefore $c_b Q < \omega_{XO}^b$, experience Rayleigh-like ω^4 scattering, while for higher frequencies/smaller wavelengths $\Gamma^\circ \sim \omega^2$.

To summarize, the typical behavior of $\Gamma_b(\omega/c_b)$ can be described as follows [87]. For $0 < \omega < \omega_P$, we find firstly a—temperature-dependent—crossover at a very low frequency between an ω^2 regime, determined by anharmonic effects, and the ω^4 regime where disorder dominates [100], followed a by second—temperature-independent—crossover from ω^4 to

ω^2, due to the spatially correlated elastic deformation at the mesoscale mentioned above [94, 100].

3.2.3.1 *Toy-model*

The qualitative effect of these crossovers on the finite-size scaling of κ_P is studied in Fig. 3.3 for a toy-model, using Eq. (3.11) with the addition of an infrared cutoff:

$$\kappa_P(\omega_{min}) = \sum_{b=L,T} \frac{c_b^2}{3} \int_{\omega_{min}}^{\omega_P} d\omega \; C(\omega)\rho_b(\omega)\frac{1}{2\Gamma_b(\omega/c_b)}, \tag{3.15}$$

and neglecting the differences between the contributions of the two polarizations. It can be observed how, for ω_{min} either lower than the first crossover and higher than the second one, κ_P is linear in $\sim \omega_{min} \sim 1/L$. However, a linear size extrapolation $\kappa(1/L) = \kappa(\infty) - a/L$ from the second region would lead to the wrong bulk limit, highlighting the risks of the standard way of size extrapolating.

It is worth noting that as long the linewidth due to harmonic disorder tends to Rayleigh's scattering [79], $\sim \omega^4$, as shown by Fig. 3.5, it implies that a purely harmonic system would have $A_b = 0$. However, it can be easily noted that from Eq. (3.11) that κ_P would diverge at any temperature in such case, in agreement with the observations of Refs. [23, 42] and Ref. [101], respectively for glasses and crystals. The effects of this singularity and the consequent bias that it introduces in the computational community are discussed in detail later in the chapter.

3.2.4 *The Haydock's algorithm*

The direct computation of the harmonic VDSF is unfeasible for systems of tens of thousands of atoms because it requires the diagonalization of the entire dynamical matrix, a procedure that scales as the cube of the number of atoms. Haydock's recursion method is an iterative procedure, based on the Lanczos orthogonalization algorithm, that allows one to estimate the VDSF as the imaginary part of a diagonal element of the vibrational Green's function of the system [72, 73]. Using this procedure, it is possible to address several systems of tens of thousands of atoms, where the quartic scaling of the harmonic linewidth is appreciable, as reported in Fig. 3.5.

Our goal is to compute Eq. (3.1). To achieve this, we express $S_b^0(\omega, \mathbf{Q})$ in terms of the diagonal matrix elements of the vibrational Green's function:

$$\lim_{\eta\to 0} \mathrm{Im}\, \langle \mathbf{Q}b|\left((\omega+i\eta)^2 - \mathbf{D}\right)^{-1}|\mathbf{Q}b\rangle = \frac{\pi}{2|\omega|}\left[S_b^0(\omega,\mathbf{Q}) + S_b^0(-\omega,\mathbf{Q})\right], \tag{3.16}$$

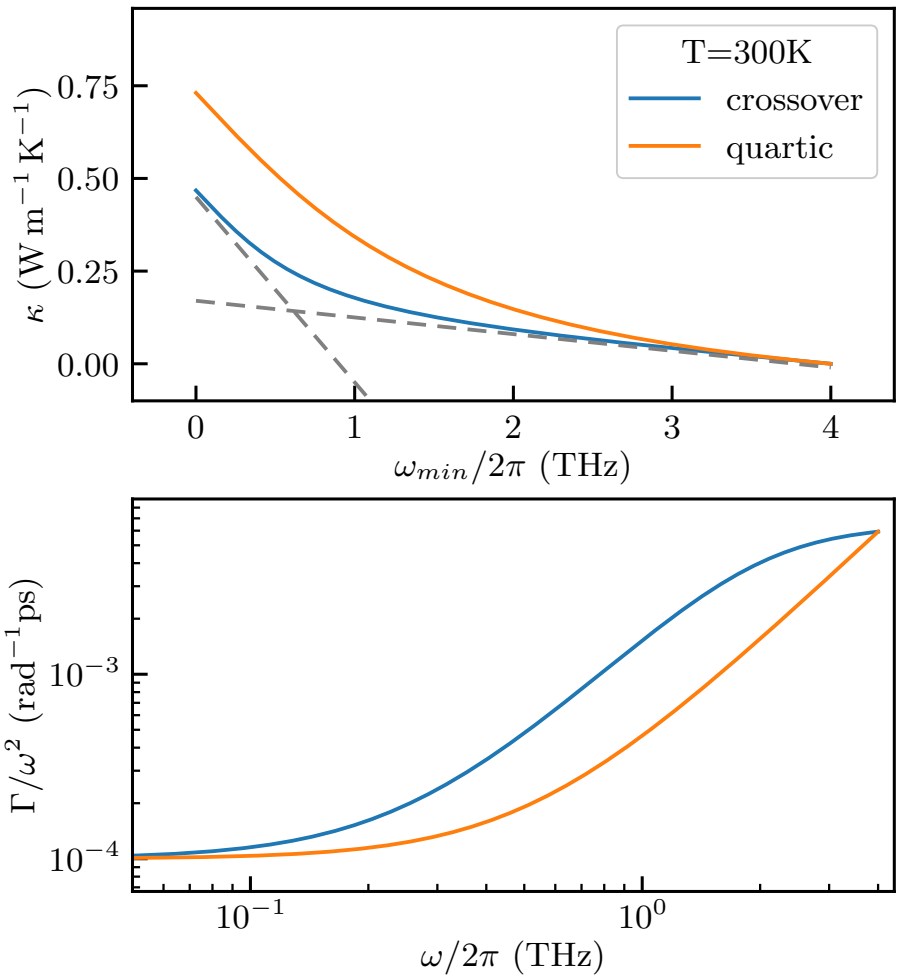

Figure 3.3: Top panel: Qualitative analysis of the contribution of propagons to thermal conductivity, given by Eq. (3.15), as a function of the minimum frequency. The calculations are conducted at $T = 300\,K$ using $\Gamma(\omega) = a\omega^2 + \Gamma^\circ(\omega)$, with $a = 10^{-4}\,\mathrm{rad}^{-1}\,\mathrm{ps}$, and Γ° evaluated for both the quartic case (orange line) and the crossover case, as depicted in the lower panel. To construct a simple yet realistic model, the speed of sound and the parameters for the *crossover* Γ° are derived from the aSiC (transverse) VDSF data, shown in Figs. 3.1-3.5. The quartic parameter is determined by matching the sound attenuation coefficients of the two cases at $\omega_P/2\pi = 4\,\mathrm{THz}$. Gray dashed lines on the top panel serve as a visual guide only. Note the logarithmic scale on both axes of the lower panel.

where $\mathbf{D}$ is the dynamical matrix and $|\mathbf{Q}b\rangle$ are the 3N eigenvectors specified before. The harmonic VDSF, Eq. (3.1), is then computed by a continued fraction expansion:

$$\frac{\pi}{2|\omega|}\left[S_b^0(\omega,\mathbf{Q})+S_b^0(-\omega,\mathbf{Q})\right]= \lim_{\eta\to 0}\operatorname{Im}\cfrac{1}{(\omega+i\eta)^2-a_0-\cfrac{b_1^2}{(\omega+i\eta)^2-a_1-\cfrac{b_2^2}{\ddots}}}, \tag{3.17}$$

where the coefficients $\{a_0, a_1, \dots\}$ and $\{b_1, b_2, \dots\}$ are evaluated by the recursion Lanczos chain:

$$\begin{aligned}
&|\phi_{-1}\rangle = |0\rangle\,,\\
&|\phi_0\rangle = |\mathbf{Q}b\rangle\,,\\
&b_n\,|\phi_n\rangle = (\mathbf{D}-a_{n-1})\,|\phi_{n-1}\rangle - b_{n-1}\,|\phi_{n-2}\rangle\,,\\
&a_n = \langle\phi_n|\,\mathbf{D}\,|\phi_n\rangle\,,\\
&b_n = \langle\phi_n|\,\mathbf{D}\,|\phi_{n-1}\rangle\,.
\end{aligned} \tag{3.18}$$

This procedure drastically reduces the computational cost of the evaluation of the harmonic VDSF, going from a $\mathcal{O}\big((3N)^3\big)$ scaling of the exact diagonalization algorithm to the $\mathcal{O}(s(3N)^2)$ scaling, where N is the number of atoms in the simulation cell and s is the number of steps of the Lanczos chain. Moreover, if the matrix of the interatomic force constants is sparse, as in the present case of short-range interactions, the numerical burden of Haydock's algorithm can be further reduced to a complexity $\mathcal{O}(sN)$. The procedure proves to be numerically robust, in spite of the well-known instabilities of the Lanczos tridiagonalization scheme [102], and approximately 200 recursion steps are typically sufficient to estimate the sound attenuation coefficients, which we increased up 600 steps to carefully test the convergence. Moreover, since the coefficients $\{a_0, a_1, \dots\}$ and $\{b_1, b_2, \dots\}$ do not depend on frequency, once they are obtained the spectrum can be inexpensively recomputed for different frequencies and for different smearing η. In particular, perturbative anharmonic effects can be included, Eq. (3.5), by substituting the fixed smearing with a frequency-dependent fit of the anharmonic linewidths, $\eta \to \gamma(\omega)$. Further details are given in App. B.3

The iterative algorithm is validated by a comparison between the value of Γ° obtained from a direct computation of the VDSF, Eq. (3.1), and Haydock's method. As shown in Fig. 3.4 for a αSiC model of 13824 atoms, there is excellent agreement between the two methods.

Both Haydock's algorithm and the direct method are not immune from their own smearing problem. However, under the assumption that $S_b(\omega, Q)$ is a Lorentzian function the problem can be easily fixed [35]. Indeed, using a fixed smearing η is equivalent to convolute the real spectrum with another Lorentzian, as Lorentzian functions are a closed group under convolution. Therefore, the constant smearing leads to another Lorentzian spectrum with the same center and $\Gamma \to \Gamma + \eta$, thus allowing for a straightforward correction *a posteriori*. A range of values for the smearing has been tested, leading to compatible results.

It is worth mentioning that in the present work, and Ref. [25], the sound attenuation coefficients Γ are first obtained for each glass sample and then averaged over samples of the same size. It has been noted that inverting the order as Ref. [35], first averaging the VDSFs and then fitting with a Lorentzian, yields smoother spectra but it does introduce an additional width due to the statistical noise of the peaks $\sim cQ$ positions. The additional width was comparable to the smallest Γ of aSi, which exhibits the weakest scattering by disorder among the three materials, thereby impacting the extrapolated thermal conductivity. This bias was eliminated using Haydock's algorithm.

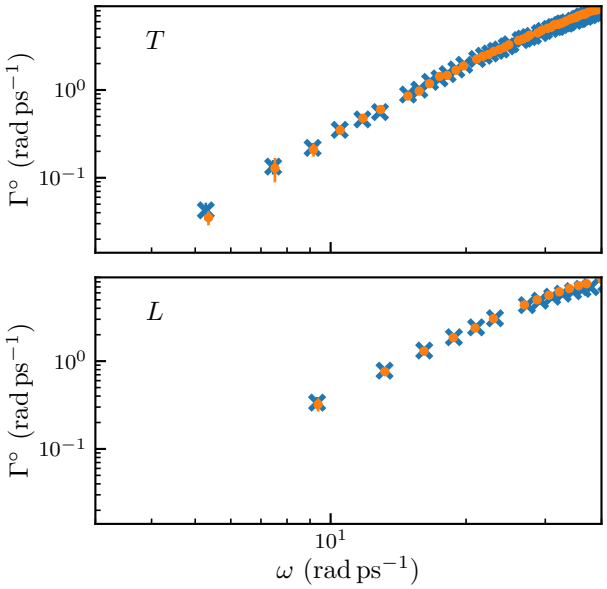

Figure 3.4: Harmonic sound attenuation coefficients Γ° aSiC obtained by fitting the harmonic vibrational dynamical structure factor, Eq. (3.1), computed via Haydock's method (orange dots) and via direct diagonalization (cyan crosses). Both results are averaged over 4 samples of 13,824 atoms, and the error bars represent standard deviations. Upper panel, transverse modes; lower panel, longitudinal modes. Picture drawn from Ref. [25]

3.2.5 *Numerical results*

In the following sections, the hydrodynamic extrapolation technique is applied to three paradigmatic glasses, chosen both for their extensive investigation in the literature and for their representation of different regimes regarding the role of propagating modes. Specifically, amorphous silica ($aSiO_2$) is a material whose thermal transport properties are primarily determined by diffusons, amorphous silicon (aSi) is dominated by propagons, and amorphous silicon carbide (aSiC) represents an intermediate case [103, 104].

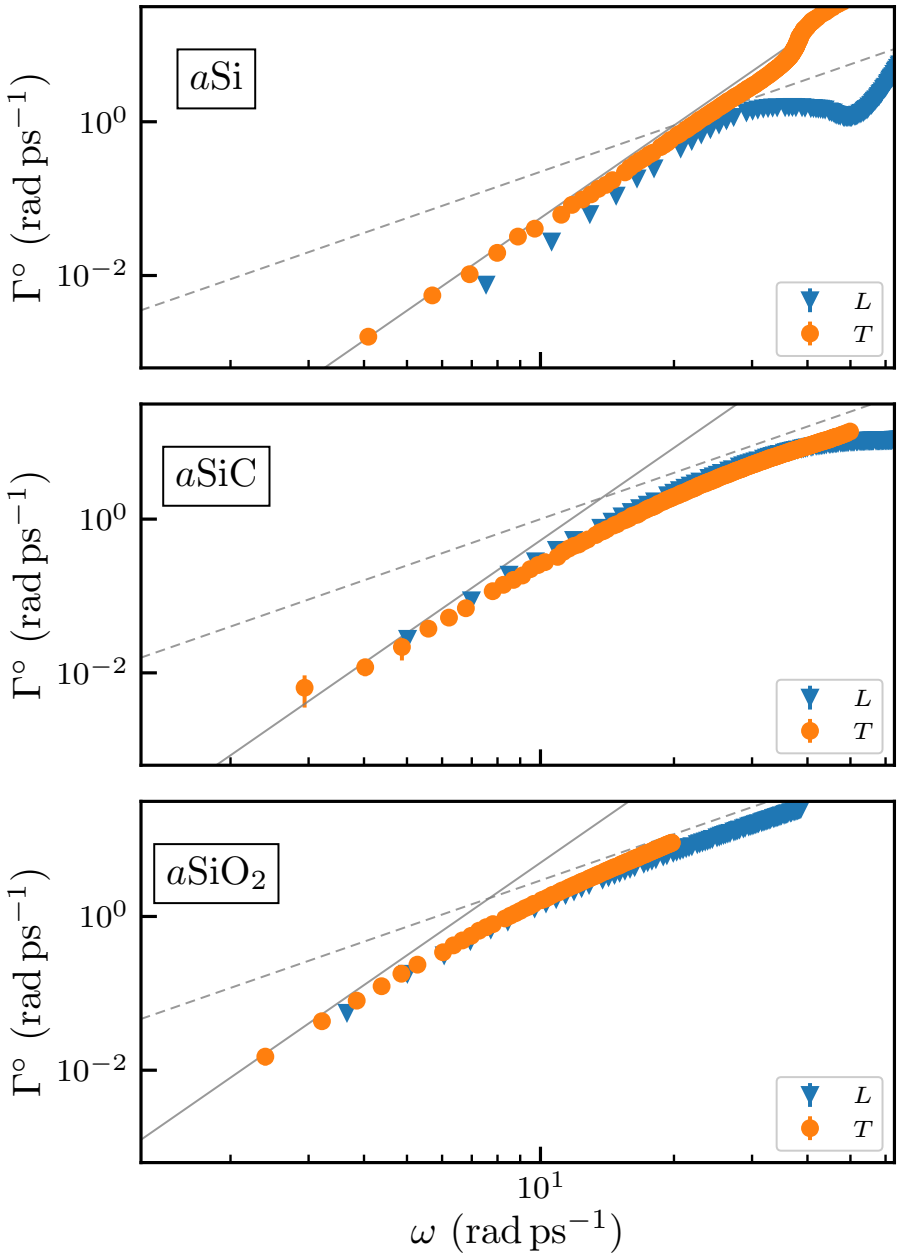

Figure 3.5: Sound attenuation coefficients in the harmonic approximation for aSi, aSiC, and $a\mathrm{SiO_2}$. The estimate is obtained by fitting the harmonic vibrational dynamical structure factor obtained through Haydock's method with its sound-wave form, Eq. (3.6), and expressing the linewidth as a function of ω, as in Eq. (3.13). The sizes of the samples are respectively 13824, 97336, and 139968 atoms. The estimated errors are smaller than the size of the symbols. The dashed and continuous gray lines indicate respectively the ω^2 and ω^4 scaling. Note the logarithmic scale on both axes. Picture drawn from Ref. [25]

The samples are generated using a melt-and-quench procedure, as detailed in Ref. [35]. Further details on the generation process and the computation of the thermal conductivity and VDSF are provided in App. C.

For all materials, the speed of sound and acoustic damping coefficients $\Gamma^{\circ}(Q)$ are obtained using Haydock's algorithm. The cutoff angular frequency for propagons is set to $\omega_P/2\pi = 3.0, 3.0, 1.2$ THz for aSi, aSiC, and aSiO$_2$, respectively. The harmonic sound attenuation coefficients are fitted using a quartic power law for aSi, while the crossover function, Eq. (3.14), is applied to both aSiC and aSiO$_2$.

The extensive validation of the method is reported in App. B.2. For all three glasses, and across a range of smearing parameters and sizes, Eq. (3.10) is tested against the propagon contribution directly computed using the AF/QHGK formulas. These tests demonstrate the method's ability to reproduce the finite-size scaling $\kappa(L)$ and its dependence on additional linewidths (e.g. η or γ_μ), while also investigating potential sources of error.

3.2.5.1 *Hydrodynamic extrapolation of amorphous silicon*

After testing the technique on all three glasses, we focus on the notable case of amorphous silicon. In the following section, we examine the finite-size scaling of QHGK calculations performed on aSi at $T = 400\,K$, as shown in Fig. 3.6. As suggested in the literature [68] and by the sharp dispersion in Fig. 3.5, the propagon contribution plays a significant role for aSi. Indeed, the bulk limit κ^{hydro}, is approximately 80% higher than κ^{QHGK} for the largest affordable size of $N = 13824$ atoms, underscoring the significance of finite-size effects. The remarkable finite-size effects are mainly due to the propagon contribution since the diffusive one quickly converges in size. It is worth noticing that the diffusive contribution could appear erroneously as the dominant contribution in small samples, even though in the bulk limit it accounts for only $\approx 30\%$ of the total thermal conductivity. Moreover, since the diffusive contribution is suppressed by the specific heat at temperatures lower than $k_B T < \hbar\omega_P$ (≈ 150K), the relative importance of κ_P over κ_D is expected to further increase at lower temperatures [35].

For convenience, the size-scaling data presented here are plotted against the number of replicas of the fundamental simulation cell repeated along each Cartesian component, $\ell = L/L_0$, where L is the actual linear size of the simulation cell and L_0 is the size of the smallest cell used for each material. For aSi, L_0 corresponds to a cell containing 8 atoms.

The QHGK finite-size results are compared with Green-Kubo Molecular Dynamics (GKMD) calculations, which are computed by averaging 10 ns trajectories from four different samples. As shown in the supplementary material of Ref. [26], $T = 400\,K$ is sufficiently high for aSi to neglect the differences between the quantum Bose-Einstein occupation function and the classical equipartition, while remaining far below the melting point. Indeed, the GKMD results are compatible with the QHGK ones for common system sizes and exhibit a similar finite-size scaling. Despite extending to larger systems, up to $N(\ell = 20) = 64000$ atoms, the GKMD results still do not achieve size-convergence.

To compare κ^{hydro} with a standard size extrapolation, the QHGK data points are fitted using the following expression (blue continuous line):

$$\kappa(L,T) = -A\arctan(B/L) + \kappa_\infty, \tag{3.19}$$

where A and B are positive parameters. This ansatz can be derived from Eq. (3.11) under the following assumptions: *i)* the classical limit is valid [i.e., $C(\omega) = k_B$]; *ii)* the linewidth follows the form $\Gamma(\omega) = a\omega^2 + b\omega^4$; and *iii)* the only size effect arises from the minimum frequency available at each size, $\omega_{\text{min}} = 2\pi c/L$.

While, in principle, separate parameter sets would be needed for each polarization, this would unnecessarily complicate the fitting procedure. Using a single set of parameters, as in Eq. (3.19), effectively averages the contributions from each polarization.

Under these simplifying assumptions, Eq. (3.11) becomes:

$$\begin{aligned}\kappa(L,T) &= \frac{k_B}{2\pi^2 c}\int_{2\pi c/L}^{\omega_P} \omega^2 \frac{1}{2(a\omega^2 + b\omega^4)} d\omega + \kappa_D \\ &= \kappa_\infty - \frac{k_B}{4\pi^2 c\sqrt{ab}}\arctan\left(\frac{2\pi c}{L}\sqrt{\frac{b}{a}}\right).\end{aligned} \tag{3.20}$$

Alternatively, another fitting approach can be suggested if the third assumption is replaced with a sub-linear scaling for the effective minimum frequency $\omega_{\text{min}}(L)$, influenced by smearing. To test this hypothesis, the QHGK data is also fitted using the following function (gray dashed line):

$$\kappa(L,T) = -A\arctan\left(\frac{B}{L^{3/4}}\right) + \kappa_\infty, \tag{3.21}$$

where A and B are positive parameters, and the exponent 3/4 is motivated by the analysis in Sec. 3.1.2.

Since only low-energy modes are involved, the classical approximation for the modal-specific heat is further justified. These fitting functions successfully capture the non-linearity (particularly the convexity) of both the QHGK and GKMD data. The error bars for the fits are computed using the standard method, based on the covariance matrix of the parameters obtained after the least-squares minimization.

Both fitting functions are compatible with the two data sets, despite being fitted exclusively to the QHGK data. Regarding the bulk thermal conductivity, the result obtained from the hydrodynamic extrapolation, κ^{hydro}, is in good agreement with the size extrapolation derived from Eq. (3.21), although it lies slightly above the curve fitted using Eq. (3.19). Despite underestimating κ^{hydro}, the latter fit still underscores the significance of finite-size effects, predicting a $\approx 50\%$ increase between the largest available QHGK system size ($\ell = 12$) and the bulk limit.

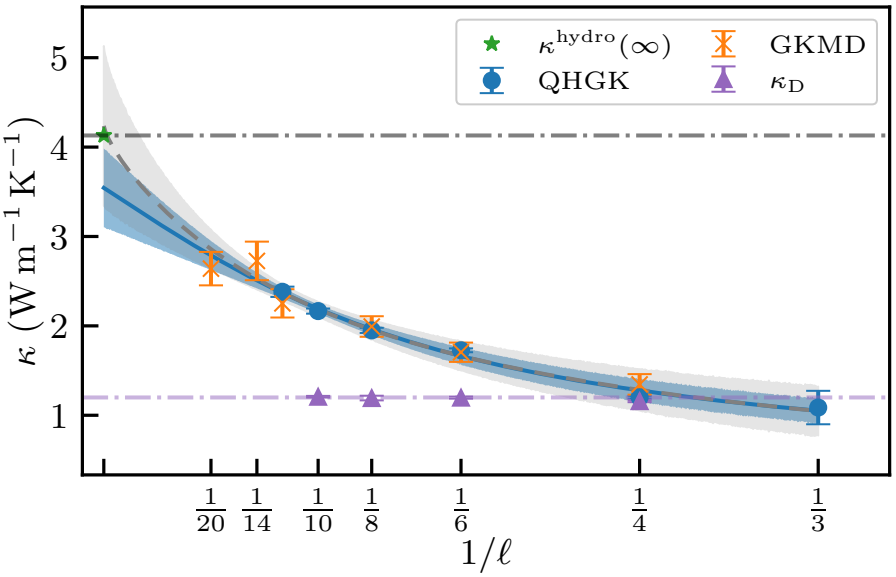

Figure 3.6: Comparison of the size scaling of κ in aSi from QHGK calculations and GKMD simulations at 400 K. Even for $\ell = 20$, i.e. for systems with 64000 atoms, the convergence in size is yet to be achieved. The solid blue line and the dashed gray line are fitted on the QHGK data according to, respectively, Eqs. (3.19)-(3.21). The bulk limit obtained with the hydrodynamic extrapolation is indicated with a star. The QHGK diffusive contribution is indicated by triangles. The shaded areas indicate the error in the fit, obtained by propagating the covariance matrix of the fitting parameters. The error bars of the GKMD data are obtained through standard block-averaging of 10 ns-long time series of four different samples for each size; the error bars of the QHGK data are standard deviations over ten different samples for each size.

3.3 ANHARMONIC REGULARIZATION OF THE THERMAL CONDUCTIVITY IN GLASSES

3.3.1 *Failure of the harmonic model of heat transport in glasses*

Using the hydrodynamic extrapolation, it is possible to properly discuss the bulk limit of the Allen-Feldman approach and highlight the importance of anharmonic effects. Indeed, Eq. (3.11) for the AF model becomes:

$$\kappa_P = \sum_{b=L,T} \frac{c_b^2}{3} \int_{\omega_{\mathrm{min}}^b}^{\omega_P} d\omega \; C(\omega)\rho_b(\omega)\frac{1}{2\Gamma_b^\circ(\omega/c_b)+\eta} \tag{3.22}$$

where $\omega_{\mathrm{min}}^b = \frac{2\pi c_b}{L}$. If the low-frequency limit follows Rayleigh's scaling, $\Gamma^\circ \sim \omega^4$, the bulk limit of the purely harmonic AF model, with $\omega_{\mathrm{min}}^b = 0$ and $\eta = 0$, would diverge at any finite temperature.

In order to demonstrate how the ω^4 dependence of the harmonic sound attenuation coefficients affects the bulk limit of the AF heat conductivity, we computed the propagon contribution to the AF conductivity in aSi, aSiO_2, and aSiC over a range of values of the smearing parameter,

η, and for finite models of progressively larger sizes. We compared these results with the analytical model provided by Eq. (3.22), $\kappa_P(T,\eta)$, Fig. 3.7. As the size of the model increases, the AF data approach the analytical benchmark, as is particularly evident for aSi (top panel). As expected, in the $\eta \to 0$ limit, the analytical model diverges due to the Rayleigh ($\propto \omega^4$) scattering term in the harmonic linewidth.

3.3.2 *Allen-Feldman harmonic bulk thermal conductivity*

Given the generality of the Rayleigh scattering and the consequent singularity of the AF model, which was actually pointed out by the same authors [64], two questions naturally arise: why do practical calculations using the AF model often overlook this infrared singularity, and more importantly, why do they compare fairly well with experimental results?

Regarding the overlooking of Rayleigh scattering and the consequent infrared singularity, it must be noted that, for typical glass model sizes, the effects in AF calculations are not always easy to detect. A particularly misleading scenario arises in glasses where the sound attenuation coefficients exhibit a second crossover from ω^4 to ω^2 due to harmonic disorder, as seen in materials like aSiC and $a\mathrm{SiO_2}$. When the infrared cutoff, $\sim c/L$, imposed by the sample size is larger than the crossover frequency ω_{XO}, the observable harmonic disorder scattering appears to follow a $\sim \omega^2$ trend, seemingly sufficient for size convergence. As briefly discussed for a toy-model glass in Fig. 3.3, as long as $\omega_{min} \sim 1/L$ is beyond ω_{XO}, the finite-size scaling of the thermal conductivity can misleadingly suggest a converging $\kappa_\infty - \kappa(L) \propto \frac{1}{L}$ trend. This issue is particularly relevant for $a\mathrm{SiO_2}$, often depicted as a highly disordered material, whose thermal conductivity is believed to exhibit very small finite-size effects and to converge well using models with a few thousand atoms, even in the harmonic approximation [103]. However, even for a highly disordered system like $a\mathrm{SiO_2}$, harmonic disorder alone is insufficient to achieve finite-size convergence. As observed in Fig. 3.5 for a very large sample containing $N \approx 1.4 \times 10^5$ atoms, the scattering due to harmonic disorder still exhibits Rayleigh-like scaling at low enough frequencies. Since the crossover frequency for $a\mathrm{SiO_2}$ is approximately $\omega_{XO} \sim 7.5\,\mathrm{rad/ps}$ for both polarizations [88], properly evaluating the bulk thermal conductivity of this system would require samples whose linear size exceeds the wavelength of the corresponding sound wave. The wavelength of the longitudinal sound wave, λ^L_{XO}, is approximately $\frac{2\pi c_L}{\omega_{XO}} \sim 60\,\text{Å}$, while the transverse sound wave's wavelength, λ^T_{XO}, is $\frac{2\pi c_T}{\omega_{XO}} \sim 35\,\text{Å}$. Thus, the sample size must be greater than λ^L_{XO}, requiring models containing at least ~ 14000 atoms.

Regarding the second and most pressing question—the comparison of actual AF calculations to experimental results—there are several factors to consider. In summary, the "unreasonable" effectiveness of AF results computed on finite samples can be explained by the fact that the infrared contribution of modes below the minimum frequency, $\omega < \omega_{min}(L)$, which

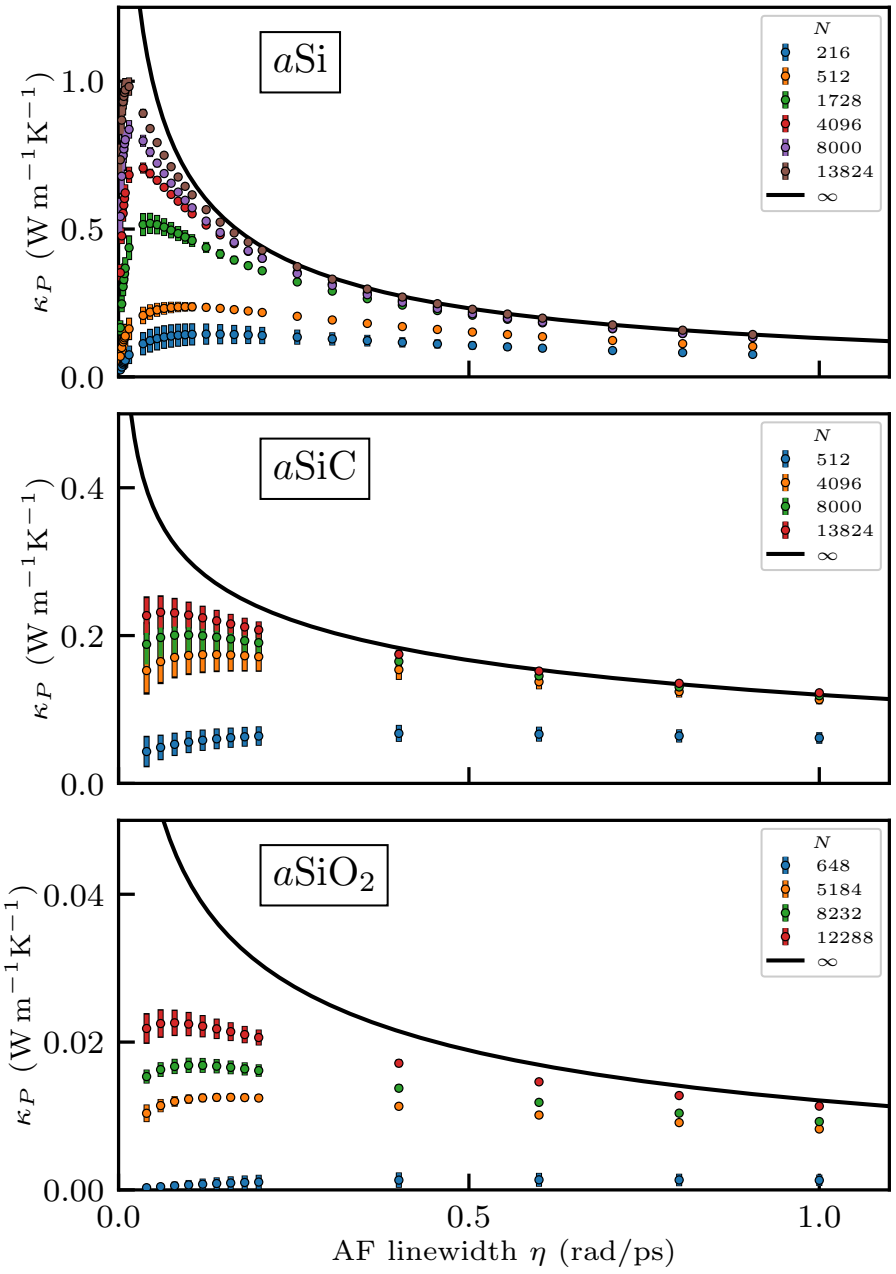

Figure 3.7: Propagon AF thermal conductivity of aSi, aSiC, and $aSiO_2$ samples with different number of atoms (N), as a function of the AF linewidth, η. Calculations are made at a temperature of 500 K. The black, solid, line is the infinite-size analytical result given by Eqs. (3.11)-(3.22). The cutoff angular frequency for propagons is set to $\omega_P/2\pi = 3$ THz, $\omega_P/2\pi = 3$ THz, and $\omega_P/2\pi = 1.2$ THz, for the three materials, respectively. Picture drawn from Ref. [35].

diverges in the harmonic approximation, is actually relatively small. This reduction is typically due to additional scattering mechanisms, such as anharmonicity or boundary scattering.

Boundary scattering is particularly important in the comparison to thin-film experiments. Indeed, the smearing parameter η introduced in finite-size AF calculations effectively mimics the boundary scattering that affects the thin-film experiments [84]. Roughly, boundary scattering adds to the linewidth of each polarization a term equal to $\eta_{BS}^{b} = c_b/d$ [42, 105], where d is the thickness of the sample, that typically range between $0.1 - 100$ μm. Still, even if $\eta \approx \eta_{BS}^{b}$ the thin film has an infrared cutoff way smaller than the simulated glass sample. However, for typical values of η_{BS}^{b} the propagon contribution is so dampened that the whole propagon contribution is negligible when compared to the diffusive contribution, thus making the differences in the infrared cutoff meaningless. In such a situation, the effectiveness of the AF calculations is justified, as previously mentioned. Indeed, if the infrared contribution is actually negligible, then the result of a AF calculations on a finite sample, where the diverging AF infrared contribution is removed by the infrared cutoff, can be in agreement with the experiment.

The effect of the boundary scattering is exemplified in Fig. 3.8, where the bulk thermal conductivity is studied both in the harmonic and weakly anharmonic cases as a function of the film thickness. In the harmonic approximation, the thermal conductivity diverges as the film thickness increases, as indicated by the solid lines. When anharmonicity is accounted for, the thermal conductivity saturates for sufficiently large thicknesses to its finite bulk value. The figure demonstrates that in materials such as αSiO_2 and αSiC, where propagons contribute marginally to heat transport compared to diffusons, the bulk limit is reached at nanometer scales. In our αSi model, where propagons play a more significant role, the bulk limit is achieved at much larger sizes, around a hundred micrometers.

It is worth noting that, at the typical thin-film sizes used experimentally, the harmonic value of κ is not significantly different from the anharmonic one. This suggests that a harmonic model on a *finite* system can provide a reasonable estimate of the thermal conductivity of a thin film even when extrapolated to $\omega_{min} \to 0$, as long as boundary scattering is appropriately accounted for.

3.3.3 *Beyond the harmonic approximation*

Finally, the temperature dependence of κ for αSiO_2 and αSi are illustrated in Fig. 3.9. The experimental measurements from the literature are compared with our hydrodynamic QHGK results and AF calculations conducted on finite samples. The anharmonic linewidths are computed on a range of temperatures and extrapolated to get a continuous line, as described in Refs. [84, 108]: $\gamma(\omega, T)/\gamma(\omega, T_0) = \frac{T}{T_0} e^{-C(\frac{1}{T} - \frac{1}{T_0})}$, where C is a positive parameter. These linewidths are then combined with the total linewidth using the Matthiessen rule [105]. For αSiO_2, the QHGK results match the bulk experimental measurement [81]. AF calculations, performed on a sample comprising 3000 atoms, also show good agreement with both bulk-QHGK results and experimental data. This indicates that,

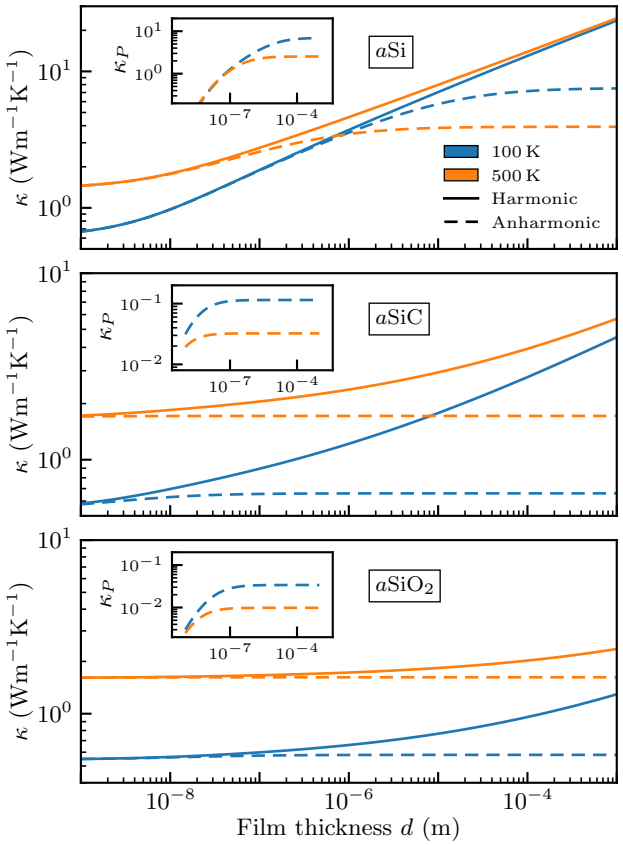

Figure 3.8: Size-dependent thermal conductivity of aSi, aSiC and $aSiO_2$ at 100 K (blue) and 500 K (orange). Calculations employ Eq. (3.11) with $\omega_{min} = 0$, and boundary scattering according to the systems' size, for propagons, while the diffuson contribution is size-independent. Solid lines show the harmonic results, while dashed lines include also anharmonic linewidths. In the insets, we display only the propagon thermal conductivity in the anharmonic case. Note the logarithmic scale on both axes. Picture drawn from Ref. [25].

in the case of $aSiO_2$, in the temperature range considered here diffusons completely dominate the thermal conductivity. Therefore, similar results are obtained neglecting contributions below ω_{min} (as done in finite AF calculations) as well as considering the anharmonic damping of propagons (as in bulk QHGK calculations). However, a direct extrapolation of the AF results regularized with a finite η yields values of κ ranging from κ_D to infinity, depending on the value of the smearing parameter.

In the case of aSi, where propagons are more important, the intriguing effectiveness of AF calculations in matching experimental data is further questioned. For instance, a calculation using 4096 atoms closely agrees with measurements on a 0.52 µm-thick film [82], seemingly validating the entire procedure. Again, what is actually happening is that the (diverging) contribution to κ from 0 to ω_{min} is being set to zero rather than to the (finite and small) value it would have when accounting for anharmonicity. For aSi, the missing contribution is not as negligible as it is for $aSiO_2$,

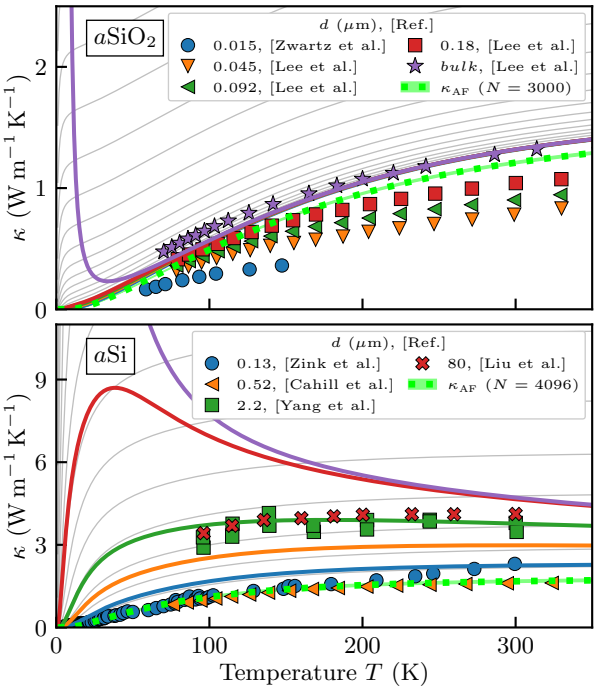

Figure 3.9: Thermal conductivity of $aSiO_2$ and aSi as functions of temperature. Markers are experimental data taken from Refs. [81, 106] ($aSiO_2$) and Refs. [42, 82, 83, 107] (aSi). The solid lines, color-matched to the markers, represent hydrodynamic QHGK results for films of the same thickness. Light-green, dotted lines are standard AF results on a finite system of the size indicated in the legend, and obtained with a smearing parameter η set to the average angular frequency spacing. Gray lines correspond to bulk AF results with κ_P computed according to Eq. (3.11), where $\omega_{min} = 0$ and η ranges from 0.1 rad ps^{-1} (bottom-most curve) to 10^{-9} rad ps^{-1} (top-most curve) on a logarithmic scale.

resulting in a pronounced difference between the QHGK results and the AF calculation.

The temperature dependence of the QHGK heat conductivity results from two competing contributions. The first one is due to diffusons, which is exponentially suppressed at low temperatures—due to the Bose-Einstein occupation function—and saturates to a constant at higher temperatures. The second one is due to propagons, which diverges as $T \to 0$ for essentially the same reasons why it does so in crystals [35]: first, the propagation of sound waves with wavelengths much larger than the atomic correlation length is relatively unaffected by disorder at leading order in ω, and, second, the temperature dependence of A_b in Eq. (3.13) causes the integral in Eq. (3.10) to diverge for vanishing temperatures [84, 108].

The differences in the concavity of the bulk $\kappa(T)$ between aSi and $aSiO_2$, illustrated in Fig. 3.9, is thus determined by the relative magnitudes of the two contributions [35]. In materials where propagons contribute marginally to the heat conductivity (such as $aSiO_2$, upper

panel), the divergence of the bulk value of $\kappa_P(T)$ becomes noticeable primarily at very low temperatures. The change in concavity is thus determined by the onset of diffusons. Conversely, when propagons dominate the thermal conductivity, the concavity might be entirely determined by κ_P, such as in the case of our model of aSi (purple curve in the lower panel of Fig. 3.9). At low temperatures, in thin films the divergence is suppressed by boundary scattering effects, as illustrated in Fig. 3.9. In bulk systems, where no boundary scattering exists, the low-temperature divergence is suppressed by the previously mentioned quantum tunneling between quasi-degenerate minima in the glass energy landscape. These quasi-degenerate minima, which are responsible for the residual entropy in glasses [109–111], are believed to lead to the plateau commonly observed at a few tens of kelvins in most glasses [60, 74–78].

To summarize, AF results on finite samples of glasses qualitatively reproduce the thin-film experiments when either boundary scattering or anharmonicity sufficiently dampens the otherwise diverging infrared contribution. On the other hand, the bulk limit of QHGK is finite at any finite temperature, but it would diverge for $T \to 0$ in the same way as it would in crystals. In practice, at extremely low temperatures, this residual divergence is suppressed by quantum-tunneling between quasi-degenerate low-energy minima [74].

As our treatment is limited to vibrational properties within a single such energy minimum, it obviously fails to address the low-temperature plateau. The description of these tunneling effects from first principles remains a major challenge in the physics of glasses and is a subject to be addressed in the future. It is noteworthy that in materials where the dominant influence of propagons on heat transport persists at temperatures higher than those at which quantum tunneling suppresses them, our analysis suggests that the bulk thermal conductivity should display a maximum at low temperatures, which could potentially be detected experimentally.

3.4 MACHINE LEARNING POTENTIALS APPLIED TO HEAT TRANSPORT IN GLASSES

All calculations for the three glasses discussed above were performed using empirical force fields. While first-principles methods to compute the BO potential, such as DFT, have the advantage of being generally more accurate and transferable, they would introduce significant computational bottlenecks when estimating the bulk thermal conductivity of glasses. Recently, materials science has been transformed by the development of Machine Learning Potentials (MLPs), which potentially offer ab initio accuracy at a classical force-field computational cost. Numerous applications of MLPs have emerged in studies of heat transport of glasses, often in combination with MD methods [112, 113].

However, despite the overall success of MLPs, a recent study has raised questions about their ability to model heat transport in glasses [113]. Specifically, MLPs appear to reproduce harmonic quantities, such as the VDOS, well but show discrepancies with the reference potential in calculating anharmonic linewidths.

Following Ref. [113], a proof-of-concept test was conducted on quantities crucial to hydrodynamic extrapolation. This test involved using a DeePMD (DP) deep neural network potential [114–116], smooth edition [117], and a Neuroevolution Potential (NEP) [118], both trained in Ref. [113] on a comprehensive dataset of liquid and amorphous αSiO_2 configurations. To directly assess the learning capability of the MLPs, the reference potential used was a short-range Tersoff force field [119], chosen for its relatively good accuracy in modeling the amorphous phase of silica.

Fig. 3.10 shows the harmonic sound attenuation coefficients (top panel) and the anharmonic linewidths (lower panel). While the harmonic contributions are similar across the three potentials, significant differences are observed for the anharmonic linewidths. Specifically, the DP potential markedly overestimates γ. The NEP potential better reproduces Tersoff's anharmonic linewidths, except for the lowest non-zero frequency mode, where γ is also overestimated.

Although the NEP demonstrates better overall performance, the increased anharmonic linewidths at low frequencies complicate the extrapolation to the bulk limit. This issue is also observed for αSi with another NEP, trained [118] for different crystalline and amorphous phases of silicon using the ab initio dataset from Ref. [120]. Since reference calculations are computationally prohibitive in this case, the NEP potential is compared with the Tersoff [121] force field, used in the rest of this chapter to simulate αSi. Indeed, Fig. 3.11 shows a similar qualitative behavior for Γ° between the two potentials, although $\Gamma^\circ_{\text{NEP}} > \Gamma^\circ_{\text{Tersoff}}$ for most data points. Conversely, the anharmonic linewidths show qualitative differences, especially at low frequencies, where the Tersoff results approach a $\sim \omega^2$ scaling, while the NEP linewidths appear not to vanish. It is possible that the NEP linewidths reverse the trend and vanish at even lower frequencies, which are not accessible for samples of this size, allowing the existence of long-lived low-frequency vibrations. However, the previous test on αSiO_2 suggests that this anomalous behavior is at least partially introduced by the use of MLPs.

In summary, this preliminary study suggests that MLPs could be used to obtain harmonic VDSF of glasses with accuracy comparable to the reference potential (e.g., ab initio accuracy), but further investigation and caution are necessary for anharmonic quantities. It is worth emphasizing that this issue does not typically appear in crystals, where MLPs anharmonic linewidths are routinely benchmarked against ab initio results [36, 122], which are computationally feasible due to periodicity.

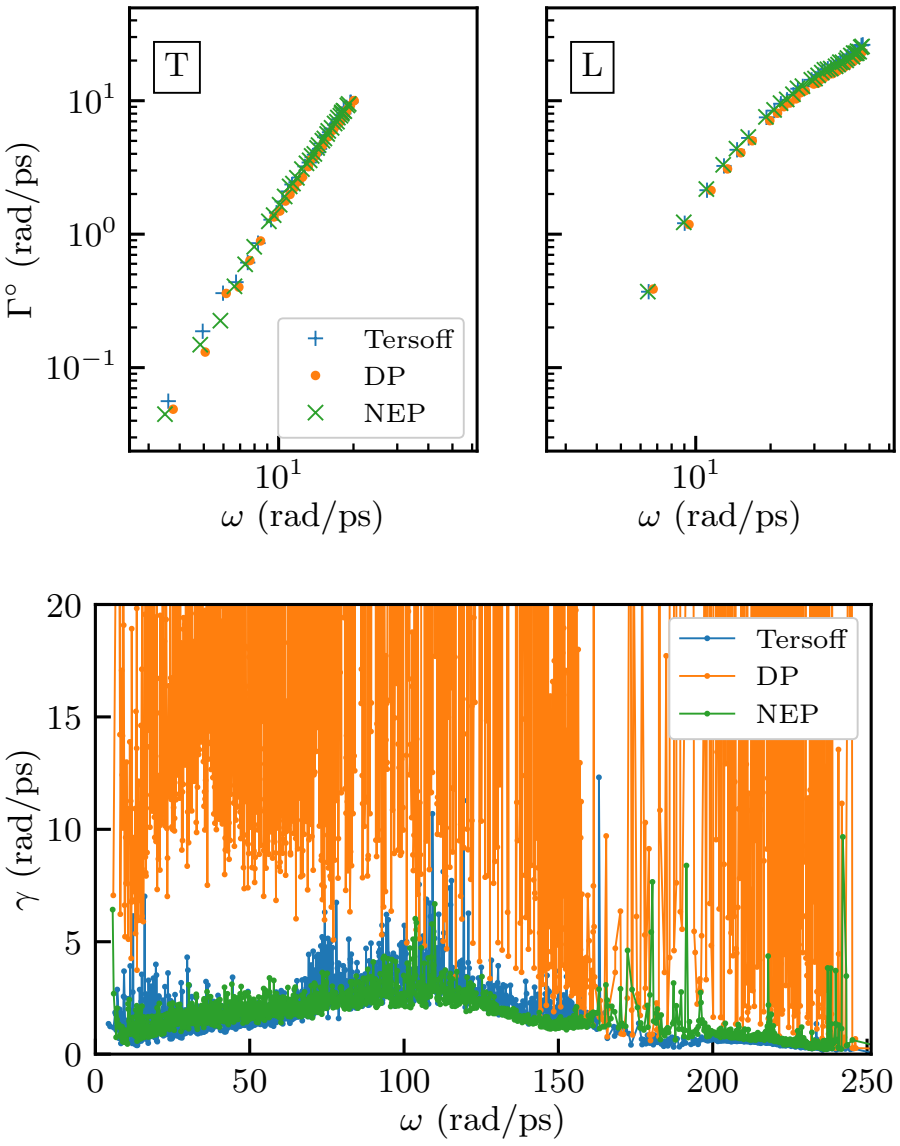

Figure 3.10: Top panel: Harmonic contribution to the sound attenuation coefficients for the transverse (left) and longitudinal polarization (right). Lower panel: Anharmonic linewidths for all normal modes. The calculations are performed using the NEP, DP [113] and Tersoff [119] potentials, the latter being the reference potential of the first two, with configurations of N = 12288 atoms for the harmonic calculations and N = 648 atoms for the anharmonic calculations. Note the logarithmic scale on both axes of the top panels.

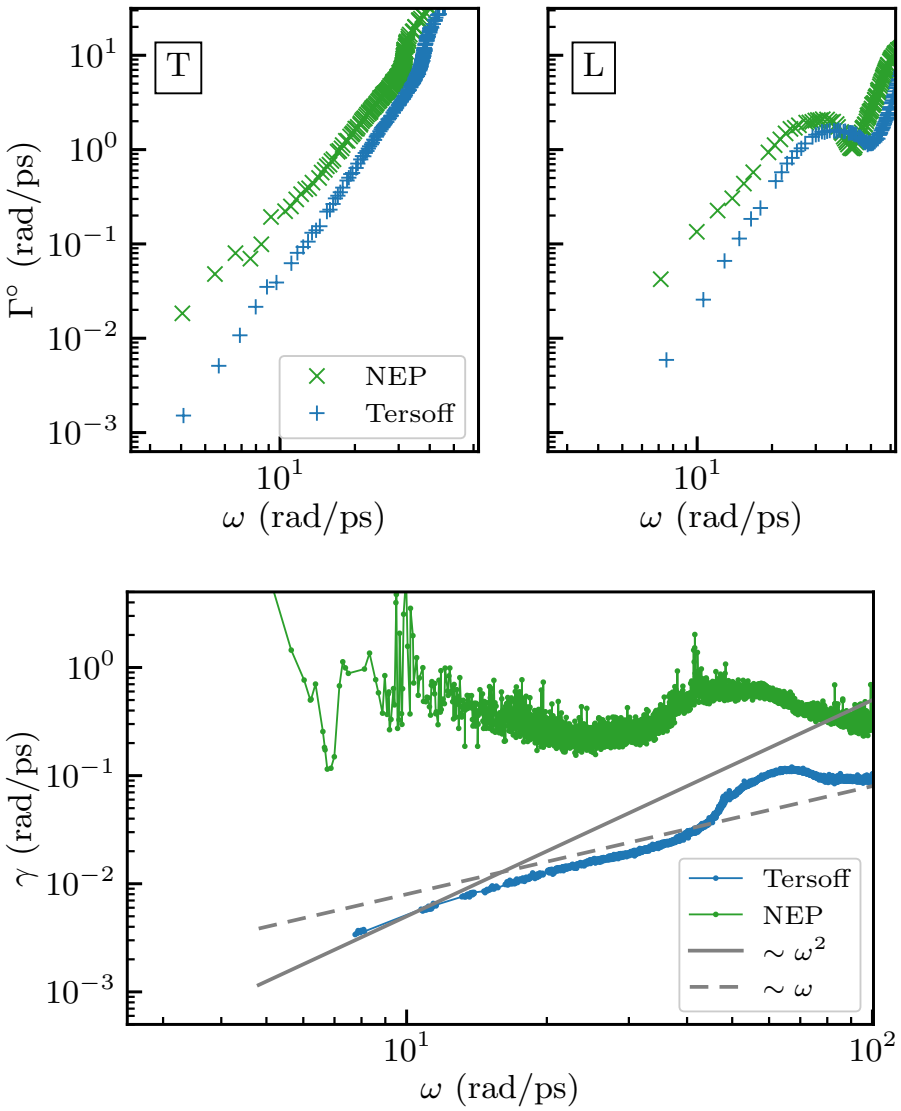

Figure 3.11: Top panel: Harmonic contribution to the sound attenuation coefficients for the transverse (left) and longitudinal polarization (right). Lower panel: Anharmonic linewidths for all normal modes. The calculations are performed using the NEP [118] and Tersoff [121] potentials, with configurations of N = 13824 atoms for the harmonic calculations and N = 1728 atoms for the anharmonic calculations. The dashed and continuous gray lines indicate respectively the ω and ω^2 scaling. Note the logarithmic scale on both axes in all panels.

4

SPATIALLY CORRELATED ALLOYS

Understanding lattice thermal transport is essential for advancing our ability to manage heat and convert wasted thermal energy into useful electrical power, thereby facilitating the design of highly efficient Thermoelectric (TE) devices. This chapter investigates the thermal conductivity of SiGe alloys, focusing on the impact of the spatially correlated (colored) disorder on thermoelectric performance [37]. By integrating first-principles calculations with hydrodynamic extrapolation [35], the study reveals a significant reduction in the contribution of acoustic modes to thermal transport. These findings underscore the potential of colored disorder to improve thermoelectric efficiency, offering valuable insights into material design for energy applications.

4.1 THE ROLE OF THERMAL TRANSPORT IN THERMOELECTRIC DEVICES

The efficiency of TE materials is quantified by the dimensionless figure of merit:

$$ZT = \frac{\sigma S^2 T}{\kappa},$$

where σ is the electrical conductivity, S the Seebeck coefficient, T the temperature, and $\kappa = \kappa^{el} + \kappa^{l}$ encompasses the thermal conductivity, computed as the sum of electronic (el) and lattice (l) contributions. While maximizing the figure of merit by manipulating electronic properties (σ, S, κ^{el}) is often complicated and limited by their interconnection, a successful strategy involves reducing the lattice thermal conductivity without significantly altering the other factors [123–125]. For silicon-based TE devices, a viable way to achieve this goal is through alloying with germanium [126, 127]. Indeed, through doping, silicon can become a TE device with a high power factor ($\sigma S^2 \sim 22\ \mu W cm^{-1} K^2$ at room temperature [128]), and σS^2 has a weak dependence on alloying with Ge [126, 129]. However, its performance is hindered by a high lattice thermal conductivity ($\approx$ 148-156 $W m^{-1} K^{-1}$ at room temperature [130]). Through alloying with a chemically similar element such as germanium, the lattice thermal conductivity of bulk pure silicon can be reduced by at least an order of magnitude [96, 131–134] without altering significantly the electronic transport coefficients [129, 135, 136]. SiGe alloys have been used since the 1960s in the high-temperature regime for applications like powering space probes with typical $ZT \approx 1$ at the operating temperature of $T \approx 1100\,K$ [137]. Further development in the field would allow $Si_{1-x}Ge_x$ alloys to compete, at room temperature, with the class of TE

devices presently employed, often composed of rare and/or toxic materials [138]. Such a goal has been pursued through the years through alloying and structuring at the nano and mesoscale [137, 139–142]. Both theoretical [143] and experimental [144] work have recently suggested using spatially correlated disorder to strongly damp acoustic vibrations.

Following Ref. [37], I present a study of the lattice thermal conductivity of $Si_{1-x}Ge_x$ alloys, both for the standard uncorrelated (*white*) and spatially correlated (*colored*) compositional disorder. Aiming to a realistic model, the state-of-the-art QHGK approach has been combined with the hydrodynamic extrapolation technique, both powered by ab initio DFT calculations. Our findings suggest that indeed colored disorder suppresses thermal transport across the acoustic vibrational spectrum, leading to up to a 4-fold enhancement in the intrinsic thermoelectric figure of merit.

The chapter is organized as follows: firstly, the Virtual Crystal Approximation is discussed, which allows one to inexpensively obtain IFC from first principles for systems with tens of thousands of atoms. Secondly, the uncorrelated case is studied, validating our numerical results against experimental ones of both thermal conductivity and Raman spectroscopy. Then, the colored case is carefully discussed. Finally, the intrinsic figure of merit in the different cases is estimated and compared to state-of-the-art SiGe systems.

4.2 MATERIAL CHARACTERIZATION

4.2.1 *Electronic and vibrational virtual crystal approximations for SiGe alloys*

Lattice dynamical methods like QHGK require the knowledge of the atomic masses and of the BO potential energy surface close to mechanical equilibrium, which is entirely determined by the electronic ground state at fixed atomic positions. Indeed, the dynamical matrix element between two atoms I and J is defined as:

$$D_{IJ} = \frac{1}{\sqrt{M_I M_J}} \frac{\partial^2 U}{\partial R_I \partial R_J}$$

where U is the BO potential energy, and R_I and M_I are the equilibrium position and mass of the Ith atom, respectively, and Cartesian indices have been omitted for notational simplicity.

For an alloy, both the BO potential and the distribution of masses contribute to the disorder. The two contributions are referred to as *chemical* and *mass* disorder, respectively. However, for chemically similar atoms like Si and Ge, it is known [135, 136] that the BO potential can be accurately described by the electronic Virtual Crystal Approximation (eVCA). In essence, for any given concentration of $Si_{1-x}Ge_x$, we consider the electronic properties of a "virtual" crystal where both atomic species are replaced by a fictitious one whose (pseudo)potential is the linear interpola-

tion of the actual species' potential. Under this assumption, the dynamical matrix becomes:

$$\overline{D}^{e}_{IJ}(x) = \frac{1}{\sqrt{M_I M_J}} \frac{\partial^2 U_x}{\partial R_I \partial R_J}$$

where U_x is the (x-dependent) BO potential energy, while the masses are still distributed at random (for details, see App. D.1). This case is referred to as the mass-disordered alloy, where mass disorder is fully accounted for, while chemical disorder is neglected. If also the mass disorder is disregarded, then one obtains the vibrational Virtual Crystal Approximation (vVCA). In this case,

$$\overline{D}^{v}_{IJ}(x) = \frac{1}{M_x} \frac{\partial^2 U_x}{\partial R_I \partial R_J}$$

where $M_x = xM_{Ge} + (1-x)M_{Si}$. While being a much cruder approximation [135], the vVCA can still provide valuable insights into the vibrational properties of the system in the acoustic region, where neighboring Si and Ge atoms vibrate in phase, and it is often the starting point for perturbative treatments of mass disorder [96, 129, 132].

The eVCA is assumed to be valid throughout this paper and it plays a fundamental role in enabling the computation of second- and third-order IFCs using *ab initio* methods such as Density Functional Perturbation Theory (DFPT) [145–147]. By neglecting chemical disorder, the IFC can be computed efficiently for the virtual crystal, fully leveraging the benefits of periodicity.

4.2.2 *Raman spectroscopy*

The reliability of the eVCA is tested by computing the nonresonant Stokes Raman spectrum of $Si_{1-x}Ge_x$ alloys using the Placzek approximation [149]. Raman spectroscopy is widely used to investigate the vibrational properties of materials, as the Raman shift between the incident and scattered light typically arises from the creation or annihilation (Stokes and anti-Stokes Raman processes, respectively) of a vibrational normal mode, coupled to the light via polarizability.

In harmonic solids, for given polarizations of the incident and scattered light, $\mathbf{e}^{in}$ and $\mathbf{e}^{out}$, respectively, the intensity of the peaks in the nonresonant Stokes Raman spectrum is proportional to [150]:

$$I^R(\omega) \propto \sum_{\mu} \delta(\omega - \omega_\mu) |\langle \phi | \mu \rangle|^2 \frac{n(\omega, T) + 1}{\omega},$$

where $|\mu\rangle$ denotes the eigenvector of the system's dynamical matrix, computed in the eVCA, and ϕ is a vector defined as:

$$\phi_{I\lambda} = \frac{1}{\sqrt{M_I}} \sum_{\alpha\beta} e^{in}_{\alpha} e^{out}_{\beta} \chi'_{I\alpha\beta\lambda},$$

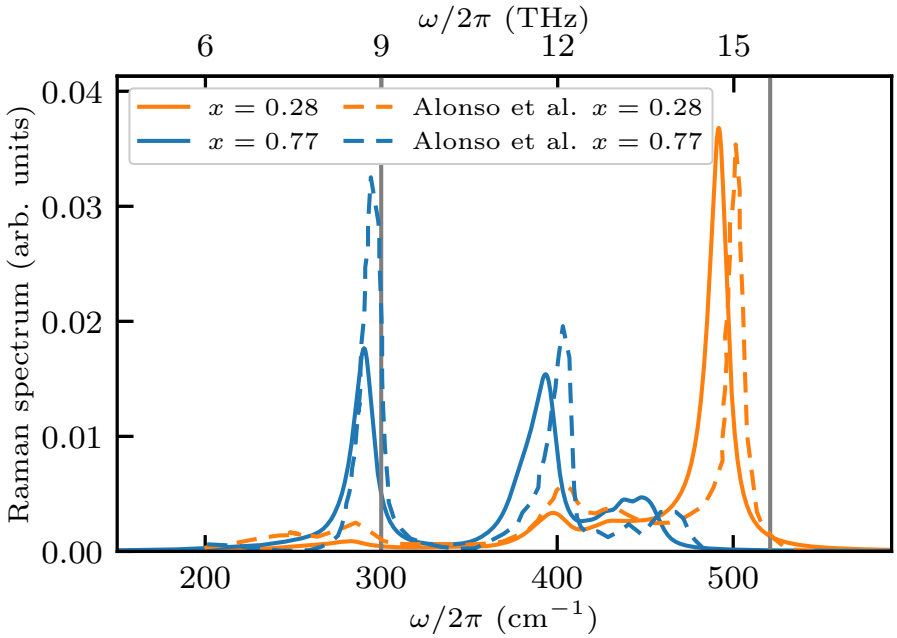

Figure 4.1: Unpolarized Stokes Raman spectroscopy at room temperature for different Germanium concentration x. Dashed lines: experimental data from Ref. [148]. Continuous lines: numerical Raman spectrum computed as explained in the main text with smearing equal to the experimental resolution $\eta = 5\,\mathrm{cm}^{-1}$. Vertical lines represent, respectively, the experimental [148] pure Germanium and Silicon bulk degenerate optic frequencies at $q = (0,0,0)$, ω_{Ge} and ω_{Si}. To take into account the small discrepancies between the DFT frequencies and the experimental ones ($\leqslant 2\%$) of the pure systems $\Delta_{Ge/Si} = \omega^{exp}_{Ge/Si} - \omega^{DFT}_{Ge/Si}$, the numerical spectra have been shifted by $\Delta(\omega) = \frac{\Delta_{Si}-\Delta_{Ge}}{\omega_{Si}-\omega_{Ge}}(\omega - \omega_{Ge}) + \Delta_{Ge}$. Picture drawn from Ref. [37]

with I as the atomic index, α, β, λ indicating Cartesian indices, and $\chi'_{I\alpha\beta\lambda} = \frac{\partial \chi^{\alpha\beta}}{\partial u_{I\lambda}}$ representing the derivative of the polarizability tensor χ with respect to atomic displacement, i.e., the tensor of Raman coefficients [73, 150].

The above summation can be rewritten in terms of the vibrational spectral function of the ϕ vector:

$$I^R(\omega) \propto \frac{n(\omega, T) + 1}{\omega} S^{\circ}_{\phi}(\omega),$$

which can be computed similarly to the VDSF, thereby leveraging Haydock's algorithm [72, 73].

Under the eVCA, the Raman tensor is periodic and can be easily computed for the unit cell of the virtual crystal [73]. Finally, the unpolarized Raman spectrum is obtained from the rotation invariants using the powder formula [151], with a computational cost of a few polarized spectra.

To compare the experimental and numerical results, the spectrum is computed with a smearing width of $\eta = 5\,\mathrm{cm}^{-1}$, matching the experimental resolution [148]. The smearing due to anharmonic linewidths at

room temperature is neglected, as numerical verification has shown that they are an order of magnitude smaller than the experimental resolution in the selected frequency range [37]. Moreover, the line broadening is predominantly caused by mass disorder, which is explicitly accounted for in the VDSF calculation.

The experimental phenomenology of $Si_{1-x}Ge_x$ alloys has been extensively studied [148, 152, 153]. The Raman spectra of pure Si and Ge systems exhibit peaks corresponding to the degenerate optical frequencies at the Γ point of the BZ, located at $521\,cm^{-1}$ and $300\,cm^{-1}$, respectively. For intermediate concentrations, three main peaks are observed at approximately $500\,cm^{-1}$, $400\,cm^{-1}$, and $300\,cm^{-1}$. These peaks are labeled as $Si-Si$, $Si-Ge$, and $Ge-Ge$ Raman peaks, as they correspond to those found in bulk crystalline SiGe alloys with similar compositions [148]. Additionally, minor peaks between $400\,cm^{-1}$ and $500\,cm^{-1}$ are commonly observed in experiments.

It is worth noting that the vVCA approach would predict only a single peak, corresponding to the optical frequency at the Γ point of the concentration-dependent virtual crystal, thus failing to capture the sensitivity of Raman spectroscopy to local atomic disorder [154]. In contrast, the eVCA calculations are qualitatively superior, as they accurately predict the positions of both the major and minor peaks observed experimentally. However, the experimental Ge peak appears sharper than the simulated one. This discrepancy could be attributed to several factors, including possible frequency-dependent variations in experimental resolution [155, 156] and the chemical bonding differences between Si and Ge sites, which are not accounted for under the eVCA assumptions.

4.2.3 *Scattering by mass disorder*

In order to rationalize the effect of disorder on the vibrational properties of the $Si_{1-x}Ge_x$ alloy, it is crucial to understand how mass disorder affects the normal modes in different frequency ranges.

Indeed, in the acoustic frequency range, there is a strong resemblance between the normal modes of the virtual crystal and those of the (mass) disordered alloy. However, the similarities disappear in the optic frequency range, as hinted by the Raman calculations. To qualitatively characterize this similarity, and its breakdown, Fig. 4.2 shows the spectral function of the virtual crystal eigenvectors in the harmonic approximation and the Inverse Participation Ratio (IPR) [64], respectively in the right and left panel. The former is defined as

$$S^{\circ}_{\mathbf{q}s}(\omega) = \lim_{\eta\to 0} \sum_{\mu} \frac{1}{\pi} \frac{\eta}{\eta^2 + (\omega - \omega_\mu)^2} |\langle \mu | \mathbf{q}s \rangle|^2, \tag{4.1}$$

where $\langle \mu | \mathbf{q}s \rangle$ is the scalar product between a vVCA normal mode eigenvector and an eVCA one. This spectral function reduces to the VDSF when the acoustic bands are $b = L, T_1, T_2$ are considered, with the difference

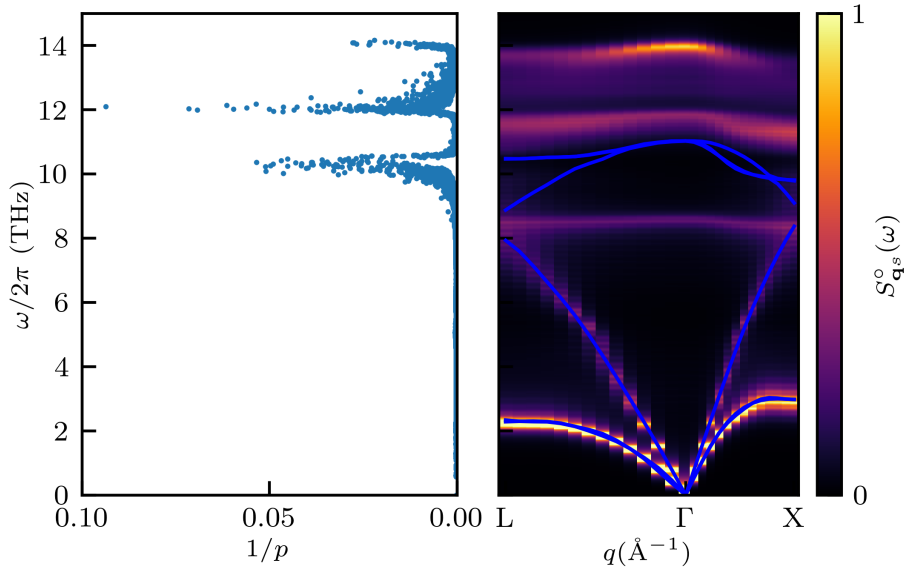

Figure 4.2: Left panel: Inverse participation ratio of the normal modes of a disordered Si-Ge alloy containing $\approx$ 12000 atoms at mixing ratio of $x = 0.5$. Right panel: Spectral function $S^{\circ}_{\mathbf{q}s}(\omega)$ (Eq. 4.1) of the same system shown as a colormap, along with the phonon band dispersion (blue) of a virtual crystal of size equivalent to $\approx$ 45000 atoms at $x = 0.5$ overlaid. The spectral function is computed in the harmonic approximation with an artificial smearing $\eta = 0.5$ rad ps^{-1} and its intensity is expressed in arbitrary units. Spikes in $1/p$ are observed in the optical frequency range, corresponding to regions where the differences between the vVCA dispersion and the VDSF are more pronounced. Figure drawn from Ref. [37].

that $|\mathbf{q}s\rangle$ are exactly orthonormal vectors, not only in the long-wavelength limit as for glasses. The IPR is defined as [64]:

$$\frac{1}{p_\mu} = \frac{\sum_I [\sum_\alpha (e^\mu_{I\alpha})^2]^2}{\sum_{I\alpha} (e^\mu_{I\alpha})^2} \tag{4.2}$$

where $e^\mu_{I\alpha}$ is the component of the μ-th vibrational eigenvector on the I-th atom in Cartesian direction α. As observed in the spectral function, the vVCA cannot predict the splitting of the optical bands into Si-Si, Si-Ge, and Ge-Ge-related modes [154]. Moreover, a significative difference between eVCA and vVCA is indicated by the IPR, which is a measure of localization and ranges from $1/N_{\text{atoms}} \approx 0$ (fully delocalized modes) to 1 (fully localized). The IPR shows that optical modes undergo substantial localization that cannot be captured in the vVCA approach, in which the normal modes are crystalline, hence fully delocalized.

4.3 THERMAL CONDUCTIVITY OF SIGE ALLOYS

Given the similarity between the separation of glasses into propagating and not-propagating modes, hydrodynamic extrapolation is also applied to this case. For isotropic thermal conductivity, the hydrodynamic extrapolation is expressed as [35]:

$$\kappa_{\text{hydro}} = \kappa_P + \kappa_D \tag{4.3}$$

$$\kappa_P = \frac{1}{3V}\sum_{\mathbf{q}b} C_{\mathbf{q}b}|v_{\mathbf{q}b}|^2 \frac{1}{2\Gamma_{\mathbf{q}b}}\Theta(\omega_P - \omega_{\mathbf{q}b}) \tag{4.4}$$

$$\kappa_D = \frac{1}{3V}\sum_{\mu\mu'} \Theta(\omega_\mu - \omega_P)\Theta(\omega_{\mu'} - \omega_P) C_{\mu\mu'}|v_{\mu\mu'}|^2 \tau_{\mu\mu'}, \tag{4.5}$$

where $\Gamma_{\mathbf{q}b}$ are extracted by the VDSF, computed with Haydock's algorithm [72, 73], and κ_P differs from Eq. (3.10) just for the use of the vVCA crystalline group velocity for the acoustic bands. The acoustic attenuation coefficients, $\Gamma_{\mathbf{q}b}$, are computed using Matthiessen's rule [105], $\Gamma_{\mathbf{q}b} = \Gamma^\circ_{\mathbf{q}b} + \gamma_{\mathbf{q}b}$, where $\gamma_{\mathbf{q}b}$ accounts for third-order anharmonic scattering affecting the vVCA acoustic vibrations. The use of vVCA anharmonic linewidths has been extended to the diffusive contribution, as numerical verification has shown that the difference between vVCA and eVCA anharmonic linewidths has a negligible impact on the overall thermal conductivity [37]. The propagon contribution is then computed on a dense grid of wavevectors in the BZ, commonly referred to as a q-mesh, and it can be easily extrapolated to the bulk limit, resulting in the inclusion of a Debye-like term in the thermal conductivity [25, 35], Eq. (3.11). The diffusive thermal conductivity, κ_D, which has been tested to be to a large extent size-insensitive (see Fig. D.3 in App. D.2), is computed using the normal modes of a disordered sample of finite size.

For the uncorrelated case, this approach is tested against the standard approach [96]. For the spatially correlated case, I rely only on the hydrodynamic extrapolation, since a perturbative treatment in the presence of spatial correlations would require further theoretical and numerical effort.

The standard approach for an uncorrelated alloy involves a perturbative treatment of disorder [96], which has successfully reproduced experimental measurements [96, 129, 132]. The phonon frequencies and velocities of the virtual crystal are used in the BTE-RTA:

$$\kappa^{\text{BTE-RTA}} = \frac{1}{3V}\sum_{\mathbf{q}s} C_{\mathbf{q}s} v_{\mathbf{q}s} v_{\mathbf{q}s} \tau_{\mathbf{q}s}, \tag{4.6}$$

where the effect of disorder scattering is accounted for in the lifetimes through Matthiessen's rule [105]: $\tau^{-1}_{\mathbf{q}s} = (\tau^{\text{anh}}_{\mathbf{q}s})^{-1} + (\tau^{\text{iso}}_{\mathbf{q}s})^{-1}$. The mass disorder linewidth $\Gamma^{\text{iso}}_{\mathbf{q}s}$ can be computed perturbatively with FGR, yielding

to Tamura's formula for perturbative isotopic scattering [157], which for a (virtual) crystal with only one chemical element reads:

$$\frac{1}{\tau^{\text{iso}}_{\mathbf{q}s}} = \frac{\pi}{2} g_2 \omega^2_{\mathbf{q}s} \rho(\omega_{\mathbf{q}s}) \tag{4.7}$$

$$= 2\Gamma^{\text{iso}}_{\mathbf{q}s}. \tag{4.8}$$

Here, ρ is the vibrational density of states normalized to unity, and g_2 is a measure of mass variance, given by:

$$g_2 = \sum_i^{n_{\text{types}}} f_i \left(1 - \frac{m_i}{\overline{m}}\right)^2,$$

involving mass (m_i) and concentration (f_i) of the ith among n_{types} species, and their average mass, $\overline{m}$.

4.3.1 *White disorder*

As previously mentioned, the bulk lattice thermal conductivity of the uncorrelated alloys is computed using the hydrodynamic extrapolation of QHGK and the standard perturbative approach, Fig. 4.3.

As observed in Ref. [132] and Fig. 4.3, even with a typically dense q-mesh with a spacing between BZ points of 0.07 Å^{-1}, i.e. a $30 \times 30 \times 30$ mesh, finite-size effects can reduce the bulk thermal conductivity at room temperature by up to 40%. While finite-size effects for the QHGK are tackled by hydrodynamic extrapolation, also the BTE-RTA results must be extrapolated to the infinite-size limit, in order to obtain a fair comparison. For the latter, the "hydrodynamic extrapolation" simply consists of including the Debye contribution on top of the results obtained with a dense q-mesh. To perform the extrapolation, in the limit of vanishing frequencies, we fit the anharmonic contribution to the sound attenuation coefficient with a temperature-dependent quadratic term and the disorder contribution with a quartic Rayleigh-like one, resulting in $\Gamma(\omega) = a(T)\omega^2 + b\omega^4$ [35, 103]. In addition to the mass disorder due to alloying, we include isotopic scattering computed due to the actual isotopic composition of Si and Ge with Eq. 4.7 for both the QHGK and BTE-RTA methods. Unsurprisingly, since the mass difference between Si and Ge is much larger than the mass differences among their corresponding isotopes, isotopic effects are impactful only for the pure systems, while for the intermediate concentrations the linewidth due to alloying is on average two to three orders of magnitudes larger.

The computed bulk thermal conductivity is shown in Fig. 4.3 as a function of the concentration of Ge (upper panel) and of the temperature (lower panel). At fixed temperature, both methods exhibit a distinctive U-shape, typical of both crystalline [96, 158] and amorphous [113, 159] alloys, with a minimum around $x \approx 0.5$. Notably, the results from both methods are nearly equivalent, with a relative difference within 10%. Both methods reproduce well the experimental data at room temperature [126].

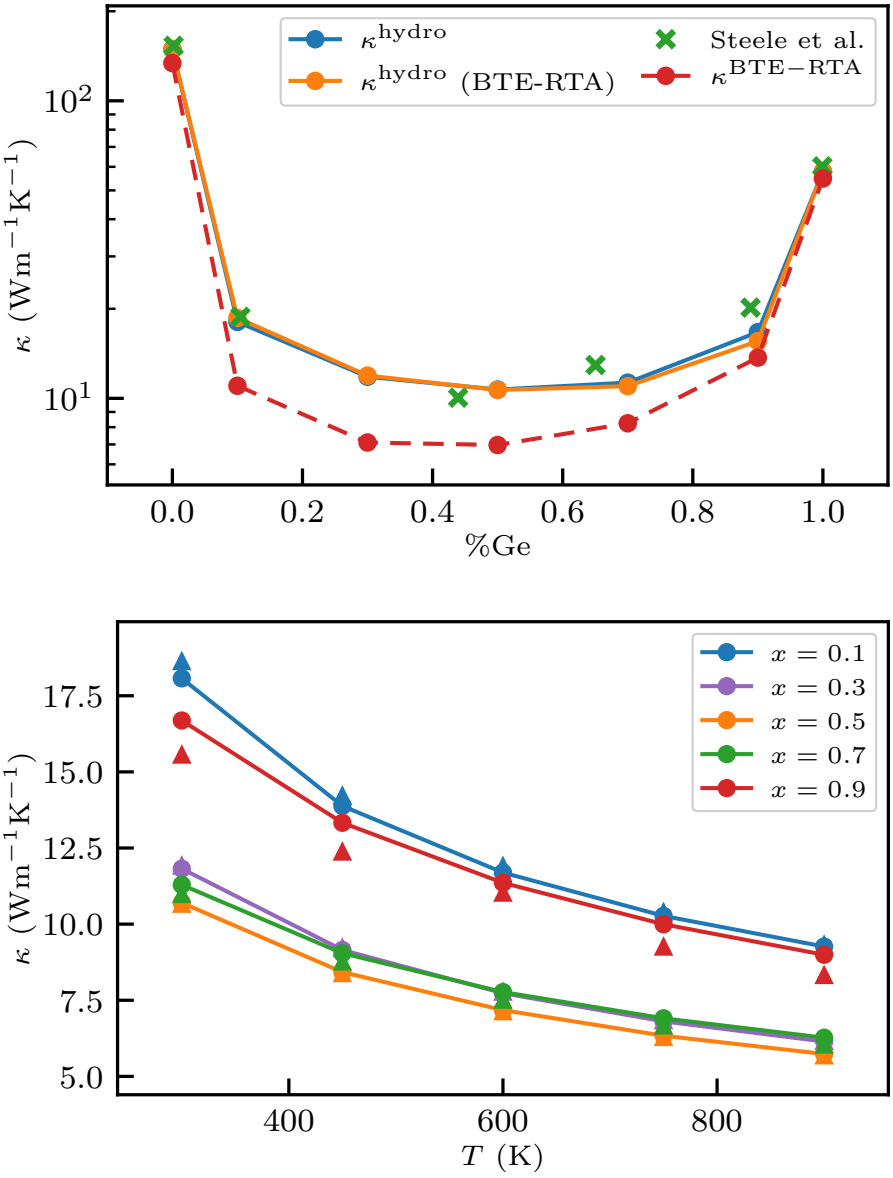

Figure 4.3: Upper panel: bulk thermal conductivity at room temperature as a function of Germanium concentration, computed with both the BTE-RTA and QHGK methods and compared to experimental results [126]. The BTE-RTA results are also shown for a dense q-mesh [28, 28, 28] (dashed line) to stress the importance of finite-size effects. Lower panel: bulk thermal conductivity as a function of temperature and concentration. The continuous lines are QHGK results, while the triangles of the same color are the corresponding BTE-RTA ones. Figure drawn from Ref. [37].

However, there is significant variance in experimental results, e.g., for $T = 300\,K$ and $x = 0.5$, κ can vary between 6 and $11\,Wm^{-1}K^{-1}$ [126, 127, 158]. This variance suggests some caution in the comparison with experiments and underscores the importance of accurately characterizing the disorder. In fact, according to Ref. [126], the process employed to grow the alloy and the resulting disorder is the most likely cause of such variance.

The success of the perturbative approach in reproducing the QHGK result, despite overlooking the diffusive contribution and misrepresenting the optical phonons dispersion, can be attributed to the dominant role of acoustic phonons, for which a perturbative treatment is reasonable. Indeed, according to Ref. [96], at room temperature and $x = 0.5$, phonons with a frequency below 2 THz contribute 88% of the total thermal conductivity. The lack of a diffusive interband contribution in the BTE-RTA would seem to imply that this method poses a lower bound to the QHGK results if harmonic scattering were exactly accounted for. Indeed, in the lower panel of Fig. 4.8 it can be observed that BTE-RTA has a smaller contribution to thermal conductivity due to modes in the optic frequency range. Instead, $\kappa^{\text{QHGK}} < \kappa^{\text{BTE-RTA}}$ at low Ge concentrations, highlighting the importance of a non-perturbative account of mass-disorder scattering. As shown in Fig. 4.4, and in agreement with the molecular dynamics results of Ref. [160], even for acoustic modes below 3 THz, linewidths from exact mass-disorder scattering can significantly differ, both positively and negatively, from the perturbative treatment of Eq. 4.7 [157]. However, it is somewhat surprising that such corrections to Tamura's formula are more pronounced for dilute concentrations ($x = 0.1, 0.9$) than for $x = 0.5$. A rationale can be found in the prefactor $-g_3 = -\sum_i^{n_{types}} f_i \left(1 - \frac{m_i}{\overline{m}}\right)^3$ in the third order correction to Eq. 4.7 [157], where for $x = 0.1, 0.5, 0.9$, the values for $-g_3$ are approximately $0.2, 0, -0.02$, respectively, which agree with the observations in Fig. 4.4.

4.3.2 *Colored disorder*

In the pursuit of reducing the predominant contribution of acoustic modes and lowering κ in SiGe thermoelectrics, several approaches have been proposed to enhance acoustic phonon scattering. From concentration graded superlattices [141, 142] to nanopores [162] and nanograins [107, 137, 139, 163–165], the overarching idea is to introduce disorder-induced scattering of large-wavelength acoustic vibrations, which would otherwise propagate almost as in a homogeneous medium. Quantitatively, the main limitation in reducing the acoustic contribution through harmonic disorder is represented by Rayleigh's ω^4 scattering. Indeed, a Rayleigh-like scattering is not sufficient alone to guarantee a finite bulk thermal conductivity in a glass, as mentioned in the previous chapter [25], or even mass-disordered harmonic crystal [166].

Under very general assumptions, disorder scattering in harmonic solids follows Rayleigh's scaling in the hydrodynamic limit [79]. Yet, the spatial correlations of elastic deformations can lead to nontrivial be-

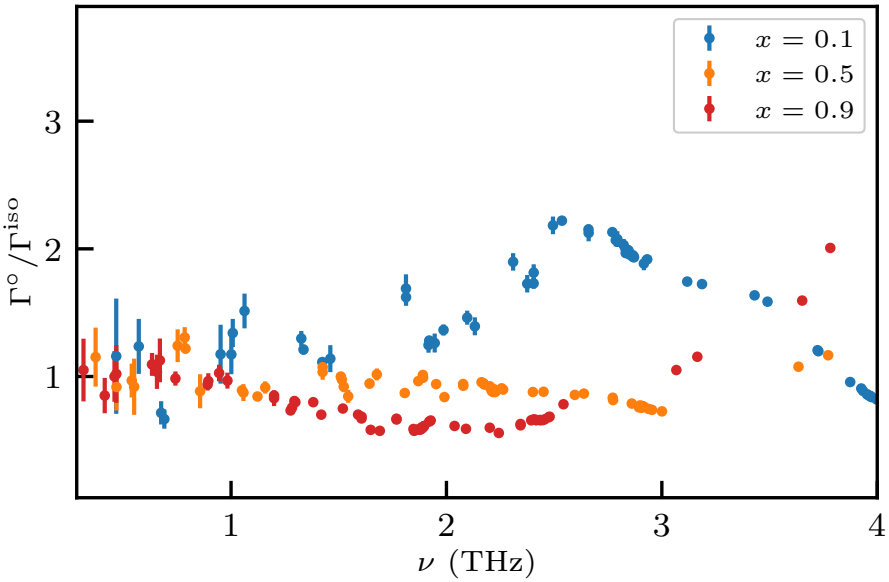

Figure 4.4: Ratio between the mass disorder linewidth computed from the non-perturbative and perturbative approaches, respectively Eq. 3.1-4.7. The error bars are the standard deviation over 4 samples of N $\approx$ 45000 atoms. Figure drawn from Ref. [37].

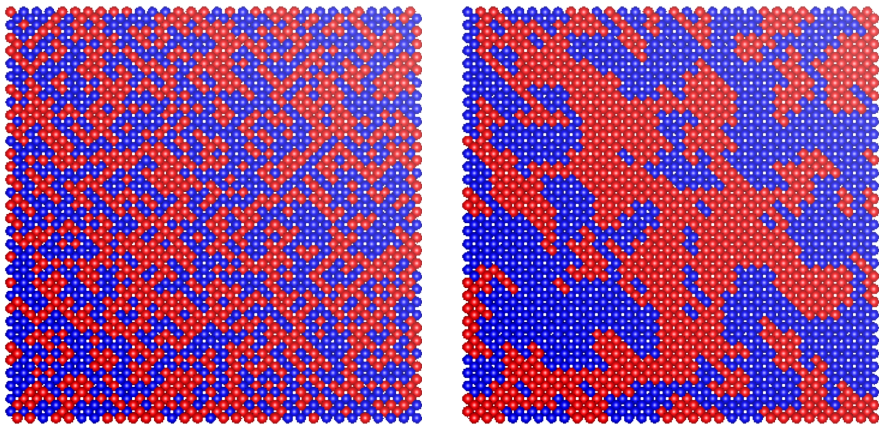

Figure 4.5: Section of a $Si_{0.5}Ge_{0.5}$ alloy model with $\approx$ 65000 atoms with uncorrelated (left) and correlated (right) mass disorder. The red and blue dots are respectively Si and Ge atoms. The correlated case is obtained with a Gaussian spatial correlation with $\sigma = 1$ as explained in the main text. Figure drawn from Ref. [37].

havior. Essentially, as long as their correlation length is finite, acoustic vibrations with wavelengths larger than the correlation length scatter like vibrational modes in a chain of equally spaced atoms connected by springs with uncorrelated random spring constants, resulting in a linewidth $\Gamma \propto \omega^4$ [98]. At higher frequencies, random media theory pre-

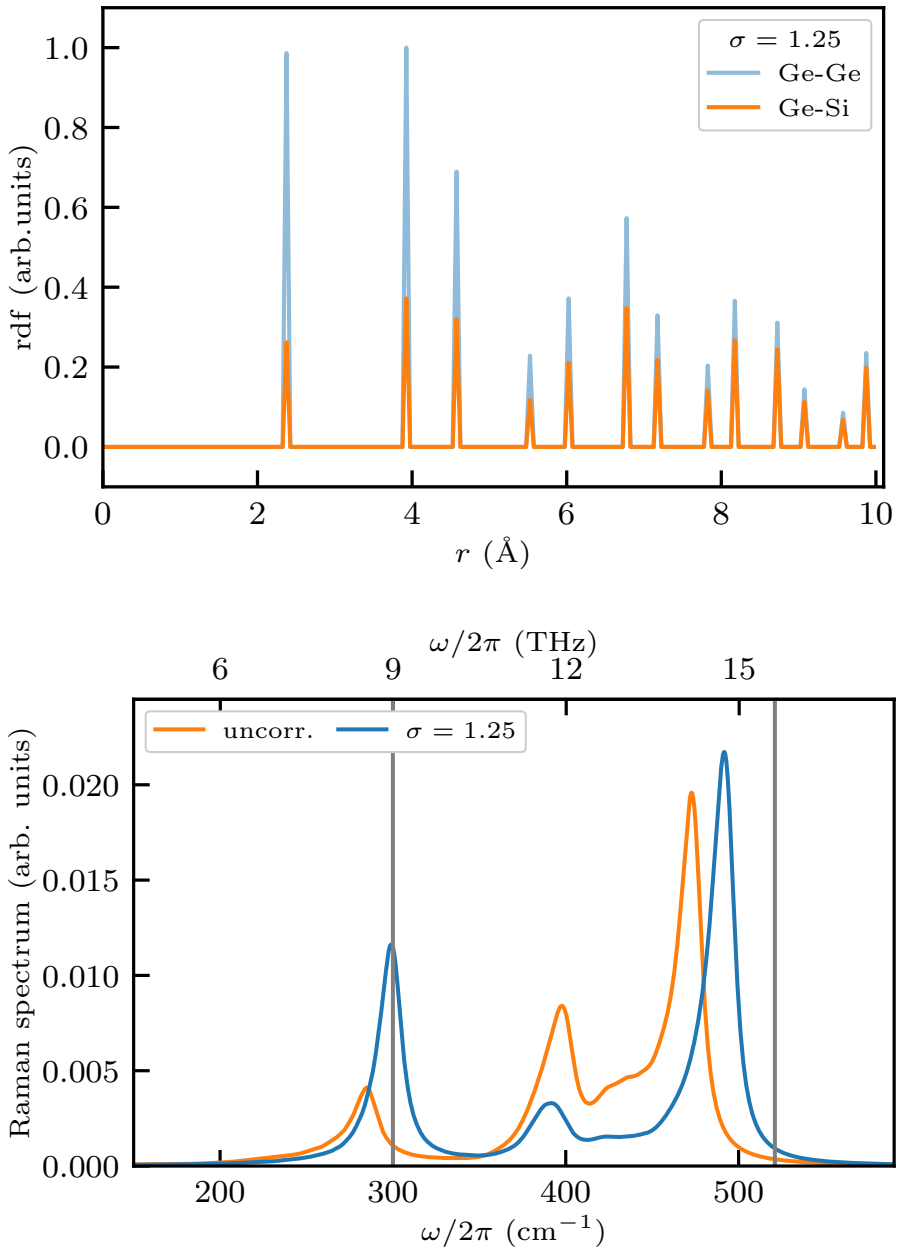

Figure 4.6: Top panel: partial radial distribution (rdf) for a sample of 43904 atoms generated with Gaussian disorder $\sigma = 1.25$ ($\sigma l_0 \approx 4.36$ Å) and $x = 0.5$. The $Si-Si$ rdf is not shown since it is identical, within statistical noise, to the $Ge-Ge$ one. Rdfs are computed with the OVITO [161] code. Bottom panel: comparison of the unpolarized Raman spectrum at room temperature between the mentioned correlated alloy and an uncorrelated one with the same size and %Ge concentration. The same shifting procedure and smearing as in Fig. 4.1 were applied.

dicts a $\omega^4 \to \omega^2$ crossover in the disorder scattering linewidths [80, 167]. This crossover is observed numerically for glasses as aSiC and aSiO$_2$, Fig. 3.5, and for aSiO$_2$ it has also been observed experimentally [87, 88]. If the correlation length increases, the crossover shifts to lower frequencies,

enhancing the overall scattering strength due to harmonic disorder [143, 144]. Ideally, a system nanostructured in order to display a disorder with an infinite correlation length could have $\omega_{XO} \approx 0$ and therefore maintain a quadratic disorder scattering rate in the $\omega \to 0$ limit. It is worth noting that such an ideal system would have a thermal conductivity less dependent on the anharmonicity than the glasses previously studied, that, under general assumptions [79], are characterized by Rayleigh-like harmonic disorder scattering.

In the following section, two prototypical kinds of disorder are studied, respectively with a finite and infinite correlation length. The type of mass disorder is characterized by the mass correlation function:

$$C(\mathbf{r}) \propto \frac{1}{N_{atoms}} \sum_{I,J=1}^{N_{atoms}} \delta M(\mathbf{R}_J)\delta M(\mathbf{R}_I)\delta(\mathbf{r}-\mathbf{R}_{IJ}), \tag{4.9}$$

where $\mathbf{R}_{IJ} = (\mathbf{R}_I - \mathbf{R}_J)$, $\delta M(\mathbf{R}_I)$ is the deviation of the mass at site I from the average mass and $C(\mathbf{r}) = C(r)$ since both correlation function are chosen isotropic.

The first case involves a Gaussian correlation $C(r) \propto e^{-r^2/(2\sigma^2 l_0^2)}$, where σ is a dimensionless parameter and l_0 is the cubic root of the unit-cell volume, $l_0 = V_0^{1/3}$, while the second case involves an infinite-range power-law correlation $C(r) \sim r^{-1}$. For each correlation function, multiple mass configurations at $x = 0.5$ are generated using the algorithm described in App. D.1. In Fig. 4.5 we display the effects of correlation on the atomic distribution on a planar cross-section of the simulation cell, observing a clustering effect as in Ref. [168]. Our procedure slightly differs from the commonly used algorithm for generating spatially correlated disorder [143, 169], aiming to reduce noise due to the discreteness of mass values.

To further characterize the correlated systems, Fig. 4.6 shows the partial radial distribution function and the unpolarized Raman spectrum. The radial distribution function reveals that introducing Gaussian correlation reduces the amount of heteroatomic Si-Ge bonds, which contrasts with the uncorrelated system at $x = 0.5$, where Si-Ge bonds are statistically as likely as homoatomic bonds. Spatial correlations also affect the Raman spectrum by inducing a blue shift in the most prominent peaks. Moreover, compared to the uncorrelated case, the Si and Ge peaks in the Raman spectrum are more intense, intuitively explained by the presence of larger clusters of pure silicon and pure germanium. These differences suggest a viable experimental method to distinguish between white and colored disorders. Although the presence of clusters might resemble polycrystalline SiGe with nanograins, [137] it is important to emphasize that, in these correlated alloys, there is no change in lattice orientation at the interfaces between different regions. In this respect, the system tends to resemble a bulk material with a disordered array of coherently embedded nanodots. From an electronic perspective, the difference between polycrystalline systems and the alloys studied here is even

more pronounced. Apart from the presumably small effect of the chemical difference between Si and Ge, which is neglected in the eVCA, the electronic density of both uncorrelated and correlated alloys considered here remains periodic. In contrast, even within the eVCA, a polycrystalline system lacks a periodic electronic density due to changes in crystal orientation at grain boundaries. This lack of periodicity can negatively impact electronic transport, thereby degrading the thermoelectric figure of merit.

Indeed, it has been experimentally shown that, for certain grain sizes, the reduction in thermal conductivity is accompanied by a decline in electronic conductivity, ultimately limiting the thermoelectric figure of merit [170].

Colored disorder significantly reduces the lattice thermal conductivity, as shown in the upper panel of Fig. 4.7. The longer the correlation length, the stronger the reduction. This reduction is due to the enhanced damping of acoustic modes (see the lower panel Fig. 4.7), which is not compensated by the slight increase in the diffusive contribution shown in Fig. 4.8. This enhanced damping not only bears substantial quantitative effects on heat conductivity but also leads to significant qualitative consequences in the harmonic approximation. In fact, below $\approx$ 2 THz one observes a crossover from the ω^4 dependence of sound-wave damping (due to Rayleigh scattering) to a ω^2 dependence. The crossover phenomenology is analogous to the one observed for αSiC, αSiO_2 in Fig. 3.5, and therefore it is also quantitatively captured using Eq. (3.14).

Apparently, also the long-range case shows a crossover. However, the crossover in this case appears to be due to finite-size effects. Indeed, it has been numerically tested that the crossover frequency, which is size-independent for the Gaussian case, reduces when the size of the sample increases.

Ignoring this finite-size crossover, the harmonic scattering linewidths have been extrapolated as $\sim \omega^2$. It is worth emphasizing again that an ideal system exhibiting $\sim \omega^2$ harmonic scattering due to correlated disorder would have a finite Debye-like contribution even without anharmonic scattering. This constitutes an exception to the conclusions of Ref. [25], which are derived for amorphous systems under the general assumption of Rayleigh scattering [79].

4.4 THERMOELECTRIC FIGURE OF MERIT

As previously mentioned, reducing the lattice thermal conductivity may improve the SiGe TE figure of merit. While the lowest value of thermal conductivity is reached for the $1/r$ correlation, the rest of our analysis is focused on the Gaussian case, whose scattering can be captured without finite-size effects and whose technological implementation would require control only at the nanoscale, rather than at all the scales. Notably, a Gaussian correlation with $\sigma = 1.25$ already reduces the thermal conductivity to approximately $2.4\,\mathrm{Wm^{-1}K^{-1}}$ at room temperature, which is about 4.5 times smaller than the corresponding value for an uncorrelated alloy.

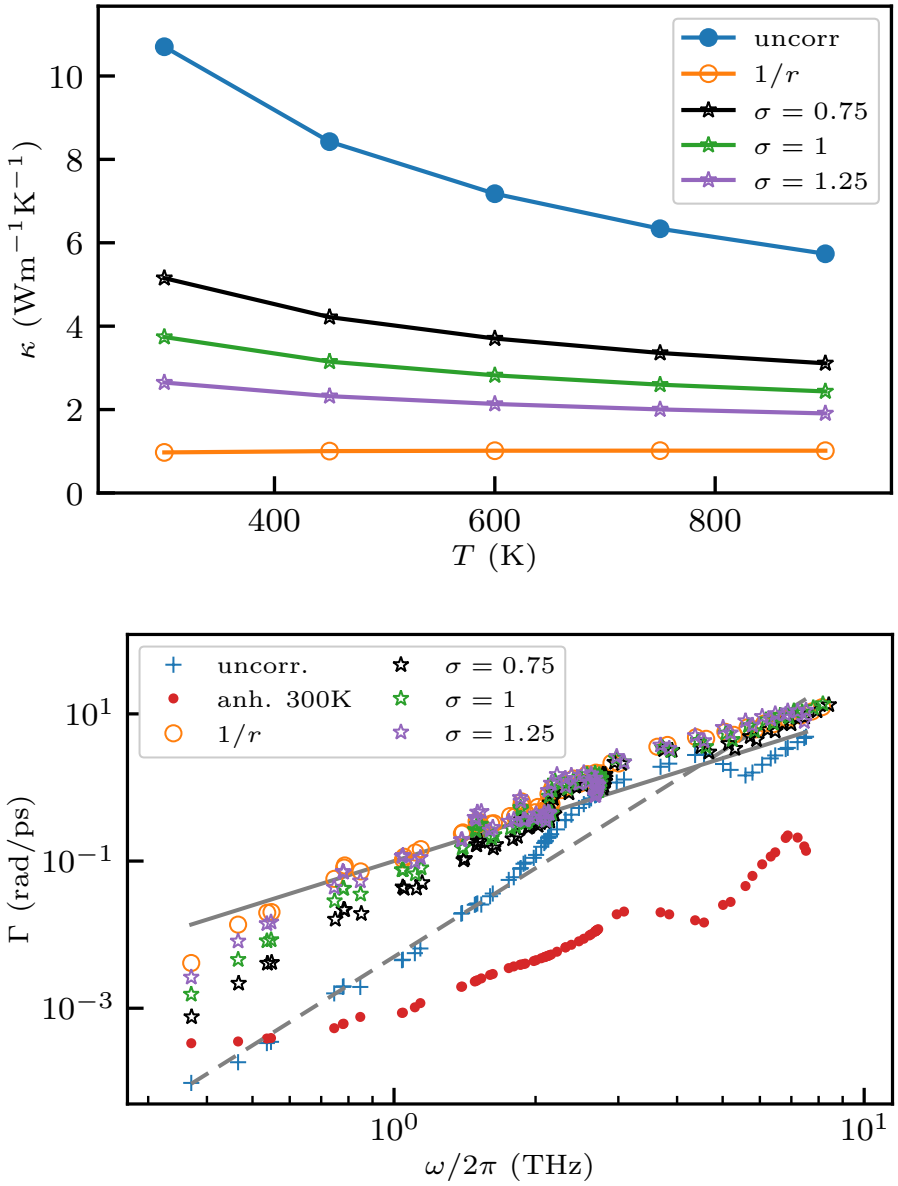

Figure 4.7: Upper panel: lattice thermal conductivity for different kinds of colored disorder, as a function of temperature. Stars and empty circles indicate respectively a Gaussian and $1/r$ spatial correlation function. σ is a dimensionless parameter proportional to the width of the Gaussian, as specified in the text. Lower panel: corresponding mass disorder linewidths of acoustic phonons as a function of frequency. Dashed and continuous gray lines are guidelines for, respectively, a ω^4 and ω^2 behavior. For comparison, we also show with red dots the anharmonic contribution to linewidths at room temperature, and with blue crosses the contribution from disorder scattering for a standard, spatially uncorrelated, alloy. All samples are at $x = 0.5$ concentration. Figure drawn from Ref. [37].

Such a large thermal conductivity reduction from the correlated mass disorder may extend the operational range of SiGe-based TE devices, so

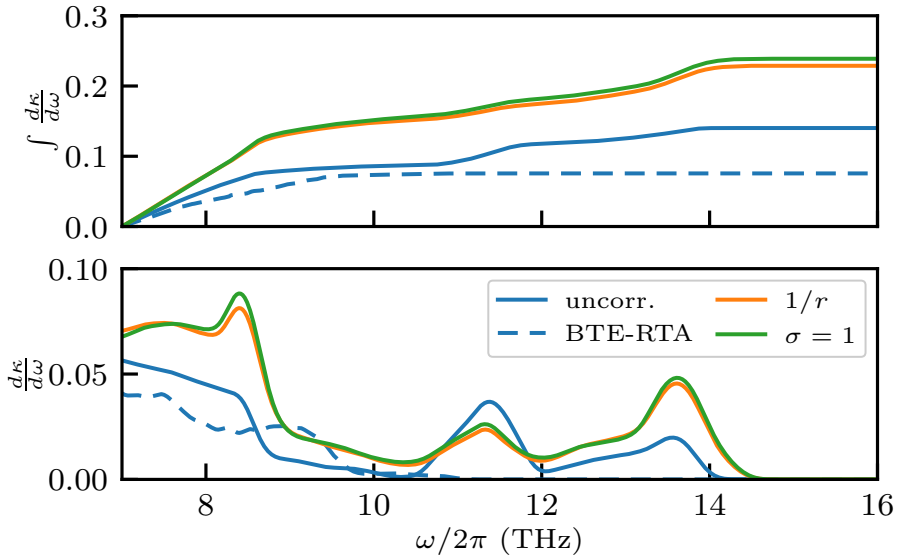

Figure 4.8: Conductivity accumulation function $\int_{\omega_a}^{\omega} \frac{d\kappa}{d\omega'} d\omega'$ (top panel) and frequency-resolved differential conductivity $\frac{d\kappa}{d\omega}$ (lower panel), Eq. (2.19), in units of $Wm^{-1}K^{-1}$ and $Wm^{-1}K^{-1}ps^{-1}$, respectively, for different instances of disorder at $T = 600\,K$ and $x = 0.5$. The lower limit for the integral in the accumulation function is set to $\omega_a/2\pi = 7$ THz, to neglect the significant differences in the acoustic frequency range due to the different nature of the disorder. The continuous lines are QHGK calculations, while the dashed blue line is the BTE-RTA result for the uncorrelated case. Figure drawn from Ref. [37].

far limited to high temperatures, $T > 1000$ K, mostly in radioisotope thermoelectric generators (RTGs) powering NASA space probes. RTGs consist of both p- and n-doped polycrystalline SiGe with carriers concentration $n \sim 10^{20}\,cm^{-3}$ and thermal conductivity lower than bulk crystalline SiGe $\kappa = 4.5\text{-}4.0\,Wm^{-1}K^{-1}$ [137]. The ZT of state-of-the-art n-doped RTG is shown in Fig. 4.9. We calculated ZT for $Si_{0.5}Ge_{0.5}$ with correlated disorder $\sigma = 1.25$, using σ_{el} and S for n-doped SiGe with $n \sim 10^{20}\,cm^{-3}$ from [129]. The intrinsic electronic transport coefficients of SiGe were computed by DFT-eVCA and the semiclassical Boltzmann transport equation in Ref. [129] as a function of alloy composition, temperature, and carrier concentration. κ_{el} is obtained by using the Wiedemann-Franz law with an experimentally determined Lorenz number of $2.14 \times 10^{-8}\,V^2K^{-2}$.

The impact of correlated disorder on the intrinsic ZT is substantial, as illustrated in Fig. 4.9. This figure shows that ZT enhancements range from a 4-fold increase at low temperatures to a 3-fold boost at high temperatures for single-crystal SiGe with uncorrelated (white) disorder, along with a 1.5-fold improvement over the n-doped NASA RTG across all temperatures.

By introducing a $1/r$ correlated mass disorder, the theoretical maximum ZT reaches 1.9 at $T = 1200\,K$. Moreover, ZT attains the techno-

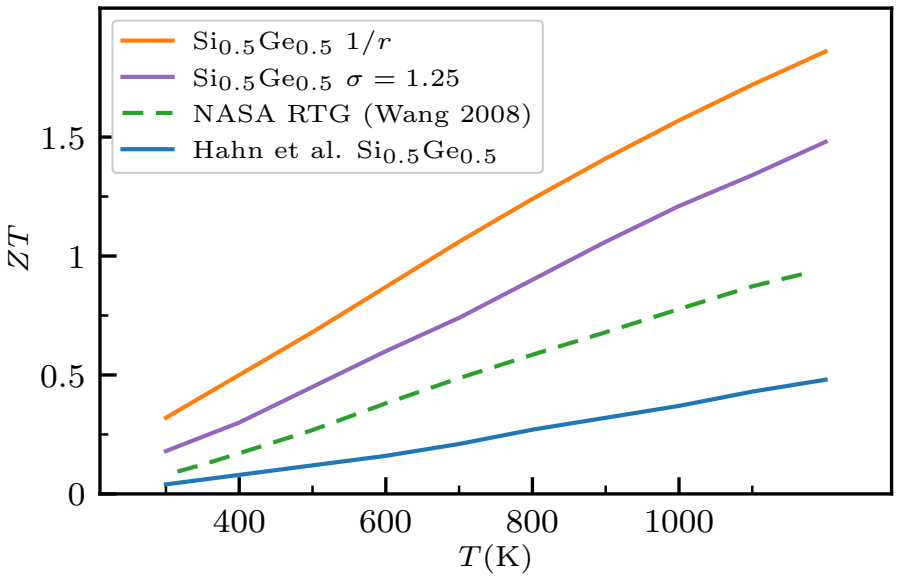

Figure 4.9: Projected improvement of the thermoelectric (TE) figure of merit for $Si_{0.5}Ge_{0.5}$ resulting from the reduction in thermal conductivity due to correlated disorder. Comparisons include the figure of merit for NASA's radioisotope thermoelectric generator (RTG) from Ref. [137] and numerical results from Ref. [129]. Solid lines represent a carrier concentration of $n = 10^{20}\,cm^{-3}$, while dashed lines correspond to $n = 2 \times 10^{20}\,cm^{-3}$. Figure adapted from Ref. [37].

logically significant threshold of 1 at $T = 700\,K$, positioning SiGe as a promising TE material for applications at moderate temperatures.

5 CONCLUSIONS

In this thesis, I have examined heat transport in both crystalline and disordered systems, emphasizing the importance of anharmonic effects, particularly in glasses, where their crucial role is often overlooked. In the first part of the thesis, I extended the Quasi-Harmonic Green-Kubo approach beyond the single-mode relaxation time approximation. This study highlights the interconnections between various formulations of the Boltzmann Transport Equation, including its recent Wigner generalization, and Green-Kubo-based methods, such as the Quasi-Harmonic Green-Kubo approach and its long-established precursor, the Allen-Feldman model. The physical distinctions between these methods were explored through their application to the antiperovskite Li_3ClO.

The remainder of the thesis focuses on disordered systems, such as glasses. On the nanoscale, the lack of periodicity clearly distinguishes glasses from crystals. However, on sufficiently large scales, both systems are expected to obey the same hydrodynamic equations. Computational limitations can severely restrict the size of atomistic simulations, thereby obscuring contributions from length scales where hydrodynamic behavior emerges. Nevertheless, capturing these contributions is crucial for obtaining a robust and reliable description of thermal conductivity. The significance of including these contributions is not only quantitative but also qualitative. For instance, the purely harmonic Allen-Feldman model may seem to yield reasonable results in finite-size samples, but its thermal conductivity diverges in the bulk limit if harmonic disorder scattering follows Rayleigh-like scaling. This issue, recognized over 30 years ago [23, 42], but often overlooked in practical calculations, underscores the importance of incorporating anharmonic effects. Chapter 3 demonstrates how third-order anharmonicity ensures a finite bulk thermal conductivity at any finite temperature, while a residual divergence at $T = 0\,K$ may require regularization by quantum tunneling scattering.

The tools developed to address the hydrodynamic contribution are not limited to glasses but are readily applicable to solid solutions. Indeed, they are valuable for designing more efficient thermoelectric devices, improving our ability to manage heat and convert otherwise wasted thermal energy into useful electrical power. For instance, they can be applied to study disordered systems such as spatially correlated silicon-germanium alloys. These tools are essential for capturing the effects of disorder at the nanoscale and beyond and hold significant potential for studying a wide range of nanostructured systems.

APPENDIX

A

DETAILS ON QUASI-HARMONIC GREEN-KUBO THEORY

A.1 GEOMETRIC GAUGE INVARIANCE OF THE ENERGY FLUX

In this section, the invariance of the generalized velocity matrix with respect to the different conventions of the Bloch basis, here labeled *geometric* gauge invariance, is discussed.

Let us consider a crystal with atomic positions $\mathbf{R}_l + \mathbf{r}_b$, where $\mathbf{R}_l, \mathbf{r}_b$ are respectively the Bravais lattice vector and basis vector. For simplicity of notation, the cartesian indices are omitted. The Bloch eigenvectors are defined as:

$$
\begin{aligned}
e^{lb}_{\mathbf{q}s} &= \frac{1}{\sqrt{N_q}} e^b_{\mathbf{q}s} e^{i\mathbf{q}\cdot(\mathbf{R}_l+\boldsymbol{\varphi}(b))} \\
\sum_{b'} D_{bb'}(\mathbf{q}) e^{b'}_s(\mathbf{q}) &= \omega^2_{\mathbf{q}s} e^b_{\mathbf{q}s} \\
D_{bb'}(\mathbf{q}) &= \sum_l D_{bb'}(\mathbf{R}_l, 0) e^{-i\mathbf{q}\cdot(\mathbf{R}_l+\boldsymbol{\varphi}(b)-\boldsymbol{\varphi}(b'))},
\end{aligned}
$$

where N_q is the number of cells, $D_{bb'}(\mathbf{R}_l, 0)$ is the dynamical matrix between a pair of atoms respectively in the l-th and 0-th unit cell, which is invariant under the translation of a lattice vector, and $\boldsymbol{\varphi}$ is a 3D arbitrary phase vector, which determines the convention adopted. For instance, the two most common conventions are the "step-like " one, $\boldsymbol{\varphi}(b) = 0$, and the "smooth" one, $\boldsymbol{\varphi}(b) = \mathbf{r}_b$ (see for instance Ref. [22]). Let us consider the unitary transformation between a generic convention and the "step-like" one, indicating the latter with a bar $(\bar{\cdot})$:

$$
\begin{aligned}
U_{bb'}(\mathbf{q}) &= \delta_{bb'} e^{i\mathbf{q}\cdot\boldsymbol{\varphi}(b)} \\
U(\mathbf{q}) D(\mathbf{q}) U^\dagger(\mathbf{q}) &= \bar{D}(\mathbf{q}) \\
U(\mathbf{q}) e_{\mathbf{q}s}(\mathbf{q}) &= \bar{e}_{\mathbf{q}s},
\end{aligned}
$$

While $\bar{\omega}_{\mathbf{q}s} = \omega_{\mathbf{q}s}$ is guaranteed under any unitary transformation, the invariance of the generalized velocity matrix can be proved by direct calculation:

$$
\begin{aligned}
2\sqrt{\omega_{\mathbf{q}s}\omega_{\mathbf{q}s'}}\mathbf{v}_{\mathbf{q}ss'} &= \sum_{bb'} \mathbf{V}_{bb'}(\mathbf{q}) (e^b_{\mathbf{q}s})^* e^{b'}_{\mathbf{q}s'} \\
&= \langle e_{\mathbf{q}s} | V(\mathbf{q}) | e_{\mathbf{q}s'} \rangle \\
&= \langle \bar{e}_s(\mathbf{q}) | \bar{V}(\mathbf{q}) | \bar{e}_{s'}(\mathbf{q}) \rangle \\
&= 2\sqrt{\omega_{\mathbf{q}s}\omega_{\mathbf{q}s'}}\bar{\mathbf{v}}_{ss'}(\mathbf{q})
\end{aligned}
$$

where

$$
V_{bb'}(\mathbf{q}) = -i \sum_l D_{bb'}(\mathbf{R}_l, 0)(\mathbf{R}_l + \mathbf{r}_b - \mathbf{r}_{b'}) e^{-i\mathbf{q}\cdot(\mathbf{R}_l+\boldsymbol{\varphi}(b)-\boldsymbol{\varphi}(b'))},
$$

which transform as $U(\mathbf{q})V(\mathbf{q})U^{\dagger}(\mathbf{q}) = \bar{V}(\mathbf{q})$. The key difference between the convention-dependent generalized velocity matrix in Ref. [28] and the present one mainly lies in the definition of the first moment of the dynamical matrix $V_{bb'}(\mathbf{q})$.

In Ref. [28], the generalized velocity matrix $v_{ss'}(\mathbf{q})$, distinguished by the QHGK one for the font, it is defined as [17]

$$\begin{aligned} v_{\mathbf{q}ss'} &= \langle e_{\mathbf{q}s}|\nabla_{\mathbf{q}}\sqrt{D(\mathbf{q})}|e_{\mathbf{q}s'}\rangle \\ &= \frac{1}{\omega_{\mathbf{q}s}+\omega_{\mathbf{q}s'}}\langle e_{\mathbf{q}s}|\nabla_{\mathbf{q}}D(\mathbf{q})|e_{\mathbf{q}s'}\rangle, \end{aligned}$$

where the first and second lines are connected by the definition of the square root of a matrix $D_{bb'}(\mathbf{q}) = \sum_{b''}\sqrt{D(\mathbf{q})}_{bb''}\sqrt{D(\mathbf{q})}_{b''b'}$, $\sqrt{D(\mathbf{q})}_{bb'} = \sum_s \omega_{\mathbf{q}s}e^{b}_{\mathbf{q}s}(e^{b'}_{\mathbf{q}s})^*$. Indeed, it can be easily verified that such a definition of $v_{\mathbf{q}ss'}$ is not geometric invariant [28] for the $s \neq s'$ elements. More importantly, the geometric dependence of $v_{\mathbf{q}ss'}$ affects the physical observable, the thermal conductivity.

Since the "step-like" convention leads to size-inconsistent [28] results, the only convention employed in WBTE implementations is the "smooth one", which yields thermal conductivities quantitatively compatible with the QHGK method [17] (implemented with any convention).

A.2 GREEN-KUBO MORI-ZWANZIG THERMAL CONDUCTIVITY FOR WELL-SEPARATED BANDS

The Full-BTE approach can be derived from GKMZ, Eq. (2.40), if the $\overline{\Lambda}^{-1}_{\mathbf{q}ss',\mathbf{k}tt'}$ elements can be neglected when $s \neq s', t \neq t'$. In the following section is proved that such approximation is reasonable under the hypothesis of well-separated bands: $|\omega_{\mathbf{q}s} - \omega_{\mathbf{q}s'}| \gg \overline{\Gamma}_{\mathbf{q}ss',\mathbf{k}tt'}\ \forall\ (\mathbf{k}tt')$.

Let us decompose the $\overline{\Lambda}$ matrix into a diagonal part, $D_{IJ} = (-\Omega_{II} + i\overline{\Gamma}_{II})\delta_{IJ}$, and an off-diagonal part $O = \overline{\Lambda} - D$ and apply the identity:

$$\overline{\Lambda}^{-1} = (D+O)^{-1} = D^{-1} - D^{-1}O(D+O)^{-1}.$$

The last term can be rewritten as:

$$\begin{aligned} \left(D^{-1}O(D+O)^{-1}\right)_{IJ} &= \sum_K D^{-1}_{IK}\left(O(D+O)^{-1}\right)_{KJ} \\ &= D^{-1}_{II}\left(O(D+O)^{-1}\right)_{IJ}. \end{aligned}$$

Since the O matrix does not diverge when $|\omega_{\mathbf{q}s} - \omega_{\mathbf{q}s'}| \to \infty$:

$$\begin{aligned} \lim_{|\omega_{\mathbf{q}s}-\omega_{\mathbf{q}s'}|\to\infty}\Big[&\frac{1}{\omega_{\mathbf{q}s'} - \omega_{\mathbf{q}s} + i\overline{\Gamma}_{\mathbf{q}ss',\mathbf{q}ss'}} - \\ &\frac{1}{\omega_{\mathbf{q}s'} - \omega_{\mathbf{q}s} + i\overline{\Gamma}_{\mathbf{q}ss',\mathbf{q}ss'}}\left(O(D+O)^{-1}\right)_{\mathbf{q}ss',\mathbf{k}tt'}\Big] = 0. \end{aligned}$$

Therefore, only the $s = s'$ elements survive in this limit. Due to the relation between $\overline{\Lambda}_{IJ}$ and $\overline{\Lambda}_{JI}$, the argument can be repeated for the second pair of band indices μ, μ'. Thus, for well-separated bands:

$$(\overline{\Lambda})^{-1}_{\mathbf{q}ss',\mathbf{k}tt'} \approx \delta_{ss'}\delta_{tt'}(\overline{\Lambda})^{-1}_{\mathbf{q}ss,\mathbf{k}tt}. \tag{A.1}$$

Finally, since the inverse of a block matrix is still a block matrix: $\overline{\Lambda}_{\mathbf{q}ss,\mathbf{k}tt} \approx \overline{\Gamma}_{\mathbf{q}ss,\mathbf{k}tt}$, which concludes the derivation of Eq. (2.41).

A.3 COMPUTATION OF THE MEMORY MATRIX IN THE CUBIC APPROXIMATION

In this section, it is shown how to compute the memory matrix for a cubic anharmonic potential, Eq. (2.23). Firstly, let us write $\overline{\Gamma}_{IJ}$ matrix, Eq. (2.32), as the FL transform of the time-correlation function of the projected time-derivatives of the $\hat{A}_I$ and $\hat{A}_J$ operators:

$$\overline{\Gamma}_{IJ}(0) = \frac{1}{G^{\circ}_{JJ}} \int_0^{\infty} dt \, \left(\mathcal{Q}\dot{\hat{A}}_I, e^{-i\mathcal{Q}\mathcal{L}\mathcal{Q}t} \mathcal{Q}\dot{\hat{A}}_J \right),$$

where

$$\begin{aligned} \mathcal{Q}\dot{\hat{A}}_I &\doteq \frac{1}{i\hbar}\mathcal{Q}[\hat{a}^{\dagger}_{\mu_1}\hat{a}_{\mu_2}, \hat{H}] \\ &= +\frac{i\hbar^{1/2}}{2} \sum_{\mu_3\mu_4} K_{\mu_1\mu_3\mu_4} \hat{X}_{\mu_3}\hat{X}_{\mu_4}\hat{a}_{\mu_2} + \\ &- \hat{a}^{\dagger}_{\mu_1} \frac{i\hbar^{1/2}}{2} \sum_{\mu_3\mu_4} K_{\mu_2\mu_3\mu_4} \hat{X}_{\mu_3}\hat{X}_{\mu_4}, \end{aligned} \tag{A.2}$$

where $\hat{X}_\mu = \hat{a}^{\dagger}_\mu + \hat{a}_\mu$ is a "scaled" normal coordinate operator and $K_{\mu\mu'\mu''}$ is invariant under exchange of the indices due to Schwarz's theorem. As explained in the main text, at our desired order of approximation, $\overline{\Gamma} \sim \mathcal{O}(K^2)$, both the average and the Liouvillian operator can be evaluated in the harmonic approximation:

$$\overline{\Gamma}_{IJ}(0) = \frac{1}{G^{\circ}_{JJ}} \int_0^{\infty} dt \, \left(\mathcal{Q}\dot{\hat{A}}_I, e^{-i\mathcal{L}t} \mathcal{Q}\dot{\hat{A}}_J \right)^{\circ}, \tag{A.3}$$

and most importantly the memory matrix can be computed using the unprojected Liouvillian operator [49–52]. In essence, the memory function is expressed using the unprojected Liouvillian via a Dyson-like decomposition [52]. As a consistency check, it can be observed that the orthogonal part of the time derivative, Eq. (A.2), remains orthogonal to any $\hat{A}_I$ during its evolution through the harmonic Liouvillian. This property can be directly verified by factoring out the time dependence and observing that the harmonic average of an odd number of creation or annihilation operators is zero.

Regarding the FLT ($\bar{f}(\omega)$), it is computed through the FT ($\tilde{f}(\omega)$):

$$\begin{aligned} \bar{f}(\omega) &= \int_0^{\infty} e^{i\omega t} f(t) \\ &= \int_{-\infty}^{\infty} e^{i\omega t} f(t)\Theta(t) \\ &= \frac{1}{2}\tilde{f}(\omega) + \frac{i}{2\pi}\mathcal{P}\int_{-\infty}^{\infty} d\omega' \, \frac{1}{\omega - \omega'}\tilde{f}(\omega'). \end{aligned}$$

where $\Theta(t)$ is the Heaviside's function and $\mathcal{P}$ indicates Cauchy's principal value . Assuming $\tilde{f}(\omega)$ to be real, as it happens if $f^*(t) = f(-t)$, the above expression reduces to the Kramers-Kronig's relations.

Combining Eq. (A.3) and Eq. (A.2), one obtains for the real part of $\overline{\Gamma}$ a linear combination of terms like:

$$\overline{\Gamma}' \sim \int_{-\infty}^{\infty} dt \int_0^{\beta} d\lambda \times K_{\mu_1\mu_5\mu_6} K_{\mu_3\mu_7\mu_8} \left\langle \hat{a}^\dagger_{\mu_5}(\tau)\hat{a}^\dagger_{\mu_6}(\tau)\hat{a}_{\mu_2}(\tau)\hat{a}^\dagger_{\mu_4}\hat{a}_{\mu_7}\hat{a}_{\mu_8}\right\rangle^\circ$$

where $\tau = t - i\hbar\lambda$. Applying Wick's theorem and reminding that $\frac{e^{\beta\hbar\omega}-1}{\hbar\omega}\delta(\omega) = \beta\delta(\omega)$, the previous equation becomes:

$$2\pi\beta K_{\mu_1\mu_5\mu_6} K_{\mu_3\mu_7\mu_8} n_{\mu_5} n_{\mu_6}(n_{\mu_2}+1)\times \delta(\omega_{\mu_5}+\omega_{\mu_6}-\omega_{\mu_2})(\delta_{\mu_5\mu_7}\delta_{\mu_6\mu_8}\delta_{\mu_2\mu_4} + \delta_{\mu_5\mu_8}\delta_{\mu_6\mu_7}\delta_{\mu_2\mu_4}).$$

A.3.1 *Scattering matrix and single-body memory function*

By applying repeatedly the procedure above, all elements of the memory matrix can be computed. Among those, there are two cases particularly relevant to the discussion in Ch. 2: the derivation of the Full-BTE and the SM approximation.

For the former case, the intraband memory matrix is fundamental to derive the Full-BTE from the GKMZ formalism. It reads:

$$\overline{\Gamma}_{\mathbf{qskt}}(z=0) = 2\gamma_{\mathbf{qs}}\delta_{\mathbf{qk}}\delta_{st} + \pi\hbar\sum_{\mathbf{q}'s'}|K_{\mathbf{qsktq}'s'}|^2 n_{\mathbf{q}'s'}\times \left[\frac{(n_{\mathbf{qs}}+1)}{n_{\mathbf{kt}}}\delta(\omega_{\mathbf{qs}}+\omega_{\mathbf{kt}}-\omega_{\mathbf{q}'s'}) - \frac{n_{\mathbf{qs}}}{n_{\mathbf{kt}}}\delta(\omega_{\mathbf{qs}}+\omega_{\mathbf{q}'s'}-\omega_{\mathbf{kt}}) - \frac{n_{\mathbf{qs}}+1}{n_{\mathbf{kt}}+1}\delta(\omega_{\mathbf{kt}}+\omega_{\mathbf{q}'s'}-\omega_{\mathbf{qs}})\right],$$

where only triplets of phonons that conserve the crystal momentum are considered since $|K_{\mathbf{qsktq}'s'}|^2 \propto \delta_{\mathbf{q}-\mathbf{q}'-\mathbf{k},\mathbf{G}}$, where $\mathbf{G}$ is any reciprocal lattice vector.

For the SM approximation, it is insightful to express the diagonal elements of $\overline{\Gamma}_{II}(0)$ through the memory function of the greater/lesser Green's function, Eq. (2.38). The latter can also be computed by applying the MZ procedure with a few minor changes. For instance, since the goal is $\langle \hat{a}_\mu(t)\hat{a}^\dagger_\mu\rangle$ it is convenient to redefine the Kubo inner product without the integration in the imaginary time $i\hbar\lambda$, a possibility explored in Ref. [47]. Then, one obtains:

$$\tilde{\gamma}^{<'}_{\mu_1}(\omega) = \frac{\pi\hbar}{2n_{\mu_1}}\sum_{\mu_2\mu_3}|K_{\mu_1\mu_2\mu_3}|^2\Big[n_{\mu_2}n_{\mu_3}\delta(\omega-\omega_{\mu_2}-\omega_{\mu_3}) + (n_{\mu_2}+1)n_{\mu_3}\delta(\omega+\omega_{\mu_2}-\omega_{\mu_3}) + n_{\mu_2}(n_{\mu_3}+1)\delta(\omega-\omega_{\mu_2}+\omega_{\mu_3}) + (n_{\mu_2}+1)(n_{\mu_3}+1)\delta(\omega+\omega_{\mu_2}+\omega_{\mu_3})\Big], \quad (A.4)$$

where $\tilde{\gamma}^{<'}_{\mu}(\omega_\mu) = \gamma_\mu$ as computed from FGR, Eq. (2.24).

B

DETAILS ON THE HYDRODYNAMIC EXTRAPOLATION

B.1 ACOUSTIC PLANE WAVES BASIS

For a system of N atoms, $|\mathbf{Q}b\rangle$ is a 3N-dimensional vector whose projection on the Ith atomic site in the α direction is:

$$\langle I\alpha|\mathbf{Q}b\rangle = \frac{1}{\sqrt{N}}\varepsilon_\alpha^b(\mathbf{Q})e^{i\mathbf{Q}\cdot\mathbf{R}_I}, \tag{B.1}$$

where $\boldsymbol{\varepsilon}^b(\mathbf{Q})$, with $b = L, T_1, T_2$, are three orthonormal polarization unit vectors. The scalar product between two plane-wave states is:

$$\langle\mathbf{Q}b|\mathbf{K}b'\rangle = \frac{1}{N}\sum_\alpha \varepsilon_\alpha^{b*}(\mathbf{Q})\varepsilon_\alpha^{b'}(\mathbf{K})\sum_I e^{i(\mathbf{K}-\mathbf{Q})\cdot\mathbf{R}_I}, \tag{B.2}$$

where the last sum is proportional to the Fourier Transform of the atomic number density, $\rho(\mathbf{r}) = \frac{1}{V}\sum_I \delta(\mathbf{r}-\mathbf{R}_I)$, i.e.

$$\begin{aligned}\tilde{\rho}(\mathbf{k}) =& \frac{1}{V}\int \rho(\mathbf{r})e^{-i\mathbf{k}\cdot\mathbf{r}}d^3r \\ =& \frac{1}{V}\sum_I \int \delta(\mathbf{r}-\mathbf{R}_I)e^{-i\mathbf{k}\cdot\mathbf{r}}d^3r \\ =& \frac{1}{V}\sum_I e^{-i\mathbf{k}\cdot\mathbf{R}_I}.\end{aligned} \tag{B.3}$$

Assuming that the material is homogeneous at length scales larger than a certain wavelength, λ, implies that $\tilde{\rho}(\mathbf{k} < 2\pi/\lambda)$ tends to a Dirac-delta function; consequently:

$$\begin{aligned}\langle\mathbf{Q}b|\mathbf{K}b'\rangle &= \sum_\alpha \varepsilon_\alpha^{b*}(\mathbf{Q})\varepsilon_\alpha^{b'}\delta_{\mathbf{QK}} \\ &= \delta_{bb'}\delta_{\mathbf{QK}}.\end{aligned} \tag{B.4}$$

Therefore, the subset of vectors $|\mathbf{Q}b\rangle$ with $|Q| < 2\pi/\lambda$ is effectively orthonormal, as numerically observed in Fig. B.1. Regarding the completeness problem, we are only interested in describing the propagons, not all the normal modes, which on the other hand would require a basis of 3N vectors. It can be argued that this set is sufficient for this purpose [85], as it can also be qualitatively understood from the plot of the VDSF, where low-frequency modes are decomposed in small-Q plane waves only.

It is now possible to write the propagon contribution to thermal conductivity on the plane-wave basis. The first term in the right-hand side of Eq. 3.12 in the main text couples only pairs of propagons. This is not

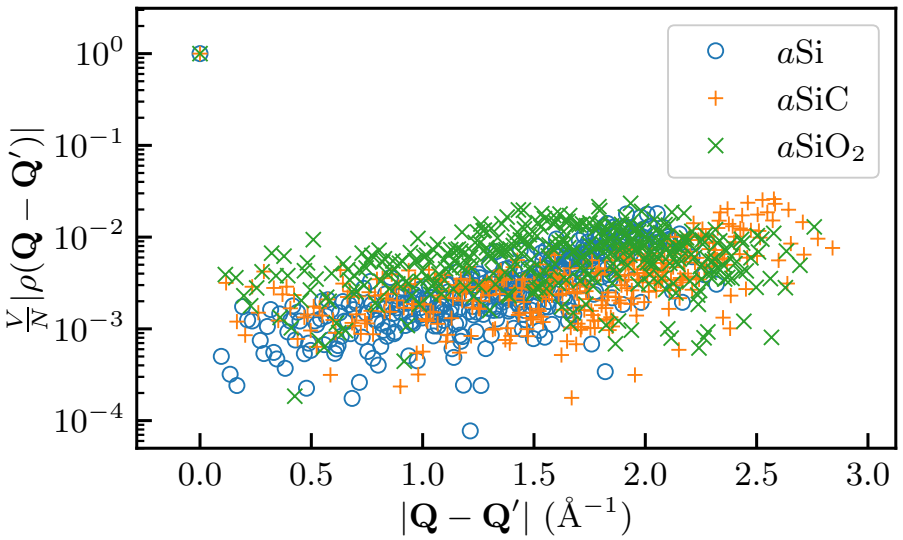

Figure B.1: The orthonormality of acoustic plane-wave vectors is tested by evaluating $\frac{V}{N}|\rho(\mathbf{Q}-\mathbf{Q}')| = \frac{1}{N}\left|\sum e^{i(\mathbf{Q}-\mathbf{Q}')}\right| \approx \delta_{\mathbf{Q}\mathbf{Q}'}$. Tests are performed on aSi, aSiC, and aSiO$_2$ configurations with $N = 13824, 13824$, and 12288 atoms, respectively, drawn from Ref. [35]. Note the logarithmic scale on the y-axis.

a property of the energy flux operator, which, in principle, has non-zero components for all different pairs of normal modes, but it is a consequence of the narrow Lorentzian functions appearing in the QHGK theory, Eq. (2.17). Taking into account this separation in frequency thanks to the Heaviside step function, let us consider the (resonant part of) energy flux operator, Eq. (2.10), :

$$\begin{aligned}\hat{J} &= \frac{-i\hbar}{V}\sum_{\mu\mu'}\frac{\omega_\mu+\omega_{\mu'}}{2}v_{\mu\mu'}\hat{a}^\dagger_\mu\hat{a}_{\mu'}\Theta(\omega_P-\omega_\mu)\Theta(\omega_P-\omega_{\mu'})\\ &= \frac{-i\hbar}{V}\sum_{\mu\mu'\in P}\frac{\omega_\mu+\omega_{\mu'}}{2}v_{\mu\mu'}\hat{a}^\dagger_\mu\hat{a}_{\mu'}\end{aligned} \tag{B.5}$$

where the P subscript means that only pairs of propagons are involved; The generalized velocity matrix [26, 33] is defined as in Eq. (2.9).

In order to get to $J^{bb'}_{\mathbf{Q}}$, the normal modes eigenvectors are expanded in plane waves

$$\epsilon^\mu_{I\alpha} = \frac{1}{\sqrt{N}}\sum_{\mathbf{Q}b}\langle\mathbf{Q}b|\mu\rangle e^{i\mathbf{Q}\cdot R_I}\varepsilon^b_\alpha(\mathbf{Q}),$$

while observing that for propagons:

$$\begin{aligned}\sum_{\mu}^{P} \omega_\mu \langle \mu|\mathbf{Q}b\rangle \hat{a}_\mu \approx & c_b Q \sum_{\mu}^{P} \langle \mu|\mathbf{Q}b\rangle \hat{a}_\mu \\ \approx & c_b Q \hat{a}_{\mathbf{Q}b}.\end{aligned} \tag{B.6}$$

as a consequence of the observation of the sharp dispersion in the VDSF. This translates into an orthogonality relation of normal modes whose frequency is far from the dispersion line, i.e., $|\langle \mathbf{Q}b|\mu\rangle| \approx 0$ if $|\omega_\mu - c_b Q| \gg \Gamma_b(Q)$. Plugging the last equations into the energy flux operator of the propagons yields:

$$\begin{aligned}\hat{\mathbf{J}} = \frac{-i\hbar}{VN} \sum_{\mathbf{Q}\mathbf{K}bb'} \frac{c_b Q + c_{b'} K}{4\sqrt{c_b c_{b'} QK}} \hat{a}^\dagger_{\mathbf{Q}b} \hat{a}_{\mathbf{K}b'} \varepsilon^{b*}_\alpha(\mathbf{Q}) \varepsilon^{b'}_\beta(\mathbf{K}) \\ \times \sum_{IJ} (\mathbf{R}_I - \mathbf{R}_J) D^{J\beta}_{I\alpha} e^{-i(\mathbf{Q}\cdot\mathbf{R}_I - \mathbf{K}\cdot\mathbf{R}_J)}.\end{aligned}$$

The derivation is analogous to the crystalline case, Sec. A.1, under the two following assumptions. Firstly, the assumption that the material is practically homogeneous above the λ scale, the dynamical matrix can only depend on $\mathbf{R}_I - \mathbf{R}_J$. Secondly that $|Qb\rangle$ are a linear combination of almost degenerate eigenvectors with eigenvalue $\approx c_b^2 Q^2$, an assumption motivated by the sharpness of the VDSF. Using the first one, with a change of variables $(\mathbf{R}_I, \mathbf{R}_J) \mapsto (\mathbf{R}_I + \mathbf{R}_J, \mathbf{R}_I - \mathbf{R}_J)$, one obtains

$$\frac{1}{N} \sum_{\mathbf{R}_I + \mathbf{R}_J} e^{-i(\mathbf{Q}-\mathbf{K})\cdot(\mathbf{R}_I+\mathbf{R}_J)/2} = \delta_{\mathbf{Q}\mathbf{K}}$$

and therefore:

$$\hat{\mathbf{J}} = \frac{\hbar}{V} \sum_{\mathbf{Q}bb'} \frac{c_b + c_{b'}}{4\sqrt{c_b c_{b'}}} \hat{a}^\dagger_{\mathbf{Q}b} \hat{a}_{\mathbf{Q}b'} \varepsilon^{b*}_\alpha(\mathbf{Q}) \varepsilon^{b'}_\beta(\mathbf{Q}) \nabla_{\mathbf{Q}} D^\beta_\alpha(\mathbf{Q}),$$

where the scalar product implies the sum over the cartesian indices and

$$\begin{aligned}\nabla_{\mathbf{Q}} D^\beta_\alpha(\mathbf{Q}) = & \nabla_{\mathbf{Q}} \sum_{\mathbf{R}_I - \mathbf{R}_J} e^{-i\mathbf{Q}\cdot(\mathbf{R}_I - \mathbf{R}_J)} D^\beta_\alpha(\mathbf{R}_I - \mathbf{R}_J) \\ = & \sum_{\mathbf{R}_I - \mathbf{R}_J} -ie^{-i\mathbf{Q}\cdot(\mathbf{R}_I - \mathbf{R}_J)} (\mathbf{R}_I - \mathbf{R}_J) D^\beta_\alpha(\mathbf{R}_I - \mathbf{R}_J).\end{aligned} \tag{B.7}$$

For $b = b'$, if the acoustic waves were exactly eigenvectors one could use the Hellmann-Feynman's theorem. Thus, using the second assumption, one obtains:

$$\sum_{\alpha,\beta} \varepsilon^\alpha_b(\mathbf{Q}) \mathbf{D}^\beta_b(\mathbf{Q}) \nabla_{\mathbf{Q}} \Phi^\beta_\alpha(\mathbf{Q}) \approx 2c_b^2 \mathbf{Q}.$$

Finally, the energy flux becomes

$$\hat{\mathbf{J}} = \frac{\hbar}{V}\sum_{\mathbf{Q},b} c_b^2\,\hat{a}^\dagger_{\mathbf{Q}b}\hat{a}_{\mathbf{Q}b}\mathbf{Q} + \text{mixed-polarization terms}, \tag{B.8}$$

where the mixed-polarization terms do not contribute if the acoustic bands are well-separated in frequency, and therefore they have not been included in our calculations.

B.1.1 *Displacement and normal mode evolution*

While the VDSF is connected through Eq. (3.4) to the Green's function of the creation/annihilation operators, it is common in the literature and in MD simulations to describe the lattice dynamics in the hydrodynamic limit through the displacements or the velocities [58, 99, 171]. Therefore, for the sake of clarity let us outline in the harmonic case the connection between the VDSF and :

$$S^\circ_{u_b}(\mathbf{Q},\omega) = \int d\omega\; e^{i\omega t}\langle \hat{\mathbf{u}}_{\mathbf{Q}b}(t)\hat{\mathbf{u}}_{-\mathbf{Q}b}\rangle,$$

where

$$\begin{aligned}
\hat{u}^\alpha_{\mathbf{Q}b} &= \frac{1}{\sqrt{N}}\sum_i \varepsilon^b_\alpha(\mathbf{Q})e^{i\mathbf{Q}\cdot\mathbf{R}_I}\hat{u}^\alpha_i \\
&= \frac{1}{\sqrt{N}}\sum_{i\mu} \varepsilon^b_\alpha(\mathbf{Q})e^{i\mathbf{Q}\cdot\mathbf{R}_I}\frac{e^{i\alpha}_\mu}{\sqrt{M_i}}\hat{\xi}_\mu \\
&= \frac{1}{\sqrt{N}}\sum_{i\mu} \varepsilon^b_\alpha(\mathbf{Q})e^{i\mathbf{Q}\cdot\mathbf{R}_I}\frac{e^{i\alpha}_\mu}{\sqrt{M_i}}\frac{1}{\sqrt{2\omega_\mu}}(\hat{a}^\dagger_\mu + \hat{a}_\mu)
\end{aligned}$$

and Eq. (2.5) is used between the last two lines. After some algebraic manipulations, one obtains:

$$\begin{aligned}
S^\circ_{u_b}(\mathbf{Q},\omega) = \sum_\mu |\langle \mathbf{Q}b\frac{1}{\sqrt{M}}|\mu\rangle|^2\frac{1}{2\omega_\mu}\times \\
[(n(\omega_\mu)+1)\delta(\omega-\omega_\mu) + n(\omega_\mu)\delta(\omega+\omega_\mu)]
\end{aligned}$$

where the mass term indicates the application of the following diagonal matrix $\left(\frac{1}{\sqrt{M}}\right)_{ij} = \delta_{ij}\frac{1}{\sqrt{M_i}}$. If the glass is monoatomic as aSi, then

$$S^\circ_{u_b}(\mathbf{Q},\omega) = \frac{1}{M}\frac{1}{2|\omega|}[(n(\omega)+1)S^\circ_b(\mathbf{Q},\omega) + n(-\omega)S^\circ_b(\mathbf{Q},-\omega)].$$

However, for a multi-component glass as $aSiO_2$ one could wonder if the sound damping coefficients extracted from the two spectra are different. Yet, in the hydrodynamic limit, one expects the mass density to be practically homogenous. Indeed, Fig. B.2 shows negligible differences between the Γ° computed for $aSiO_2$ using the two vectors, $|\mathbf{Q}b\rangle$ or $|M^{-1/2}\mathbf{Q}b\rangle$,

in Eq. (3.17). Assuming the anharmonic linewidth can be included with Matthiessen's rule [105], we expect experiments to roughly find the same sound damping coefficients whether S_{u_b} or S_b is actually probed. Analogous considerations can be made for the velocities/momenta.

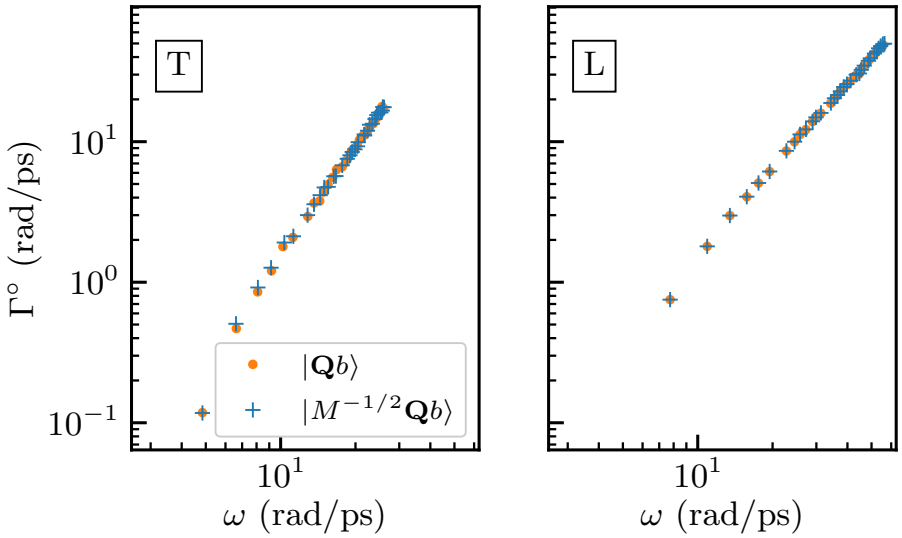

Figure B.2: Harmonic contribution to sound damping coefficients Γ° of $aSiO_2$ using $|\mathbf{Q}b\rangle$ or $|M^{-1/2}\mathbf{Q}b\rangle$ as initial vector of the Haydock's algorithm. Test performed on a $aSiO_2$ configuration with $N = 12288$ from Ref. [25].

B.2 HYDRODYNAMIC FINITE-SIZE SCALING

The following section compares, for different sizes and smearing parameters, the Allen-Feldman propagon contribution to thermal conductivity with the theoretical one computed using Eq. (3.10). The discrete version has been preferred to Eq. (3.11), with proper infrared cutoffs $\omega^b_{min} = c_b 2\pi/L$, since for smaller samples the number of $\mathbf{Q} \in P$ is insufficient to justify the continuous limit. For the largest size of each material, no significant difference has been found. To represent the effect of the Heaviside function of Eq. (3.12) in the numerical data, the contribution of the acoustic sound waves nearest to the border of the propagon region, $c_b Q = \omega_P$, is halved. This contribution will be referred to as the *border* contribution.

Firstly, the method is tested for a range of smearing parameters η, as used in the AF approach, instead of employing $\gamma_\mu(T)$ as in the QHGK method. This choice is motivated by the desire to avoid the QHGK smearing problem, which could effectively alter the minimum angular frequency. As long as γ_μ does not vary significantly for modes within the frequency range between ω_{min} and ω_P, which excludes the vanishing frequency limit where γ approaches zero, the smearing parameter η can be regarded as a rough representation of an average γ_μ.

Fig. B.3 demonstrates good agreement between the AF propagon thermal conductivity and Eq. (3.10), which implicitly depends on the system size through the spacing of the wavevectors. Consistent with Fig. 3.5, the propagon contribution is greatest for aSi, the material least scattered by harmonic disorder, and progressively smaller for aSiC and $a\mathrm{SiO_2}$. The slight shift between the numerical and theoretical data for $a\mathrm{SiO_2}$, even for sufficiently large η, is discussed below.

However, the AF thermal conductivity drastically decreases below a certain value of η, inverting its previously monotonically decreasing trend with the smearing parameter. While $\kappa_P(\eta)$ being a decreasing function can be physically rationalized—since η effectively increases the harmonic sound damping coefficients, $\Gamma^\circ \to \Gamma^\circ + \eta$—the abrupt inversion likely indicates the smearing problem discussed earlier: η becomes much smaller than the average spacing between modes.

After testing our theory for a range of different smearing parameters, the model is further evaluated for varying system sizes using a relatively large fixed η, selected from the results of the previous plot.

The border contribution mentioned earlier, which would be negligible as a surface term in the hydrodynamic limit, becomes significant for smaller system sizes, particularly for the material with the largest Γ°, $a\mathrm{SiO_2}$. Specifically, since the normal modes "associated" with the acoustic sound wave $c_b\mathbf{Q}$ are theoretically distributed around the acoustic pole with a broadening Γ°, it is not straightforward to determine the exact contribution of sound waves with $c_b\mathbf{Q} \approx \omega_P$ to the thermal conductivity. This uncertainty is represented by the error bars in the theoretical data of Fig. B.4, with their value set to half of the surface contribution.

While additional approximations in the derivation of Eq. 3.10—such as the neglected interband contributions between polarizations—may contribute to discrepancies, the surface error alone is sufficient to account for most of the observed differences between the numerical and theoretical data points.

B.3 INTERPOLATION SCHEME FOR THE ANHARMONIC LINEWIDTHS

The computation of third-order anharmonic linewidths in glasses generally constitutes another bottleneck of QHGK calculations [33], as it scales as N^3. Thus, this computation by itself would severely limit our ability to study size effects. It is thus customary to adopt some interpolation scheme for obtaining the linewidths of a large model starting from a smaller one [26, 33, 66]. First, in order to smoothen the data, we apply a Gaussian filter to the computed anharmonic linewidths at each temperature, $\gamma_\mu(T)$:

$$\gamma(\omega, T) = \frac{\sum_\mu \gamma_\mu(T) \frac{1}{\sqrt{2\pi\sigma^2}} \exp\left[\frac{(\omega-\omega_\mu)^2}{2\sigma^2}\right]}{\sum_\mu \frac{1}{\sqrt{2\pi\sigma^2}} \exp\left[\frac{(\omega-\omega_\mu)^2}{2\sigma^2}\right]}. \tag{B.9}$$

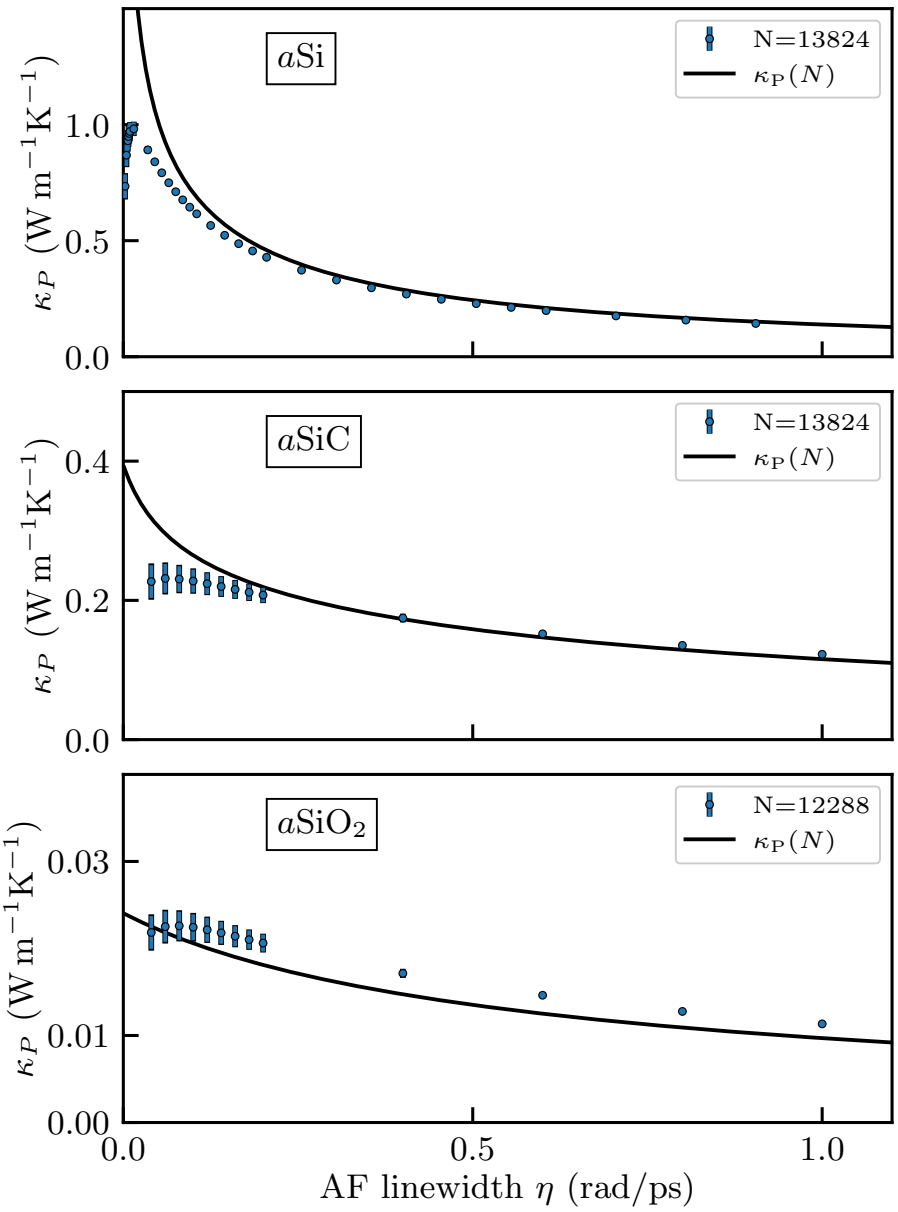

Figure B.3: Allen-Feldman propagon contribution to thermal conductivity as a function of the smearing parameter η for finite samples at $T = 500\,K$. For each of the three glasses, the AF data (markers) is compared with the theoretical results (solid lines) computed using Eq. (3.10).

Then, the smoothed function is spline-interpolated with the condition $\lim_{\omega\to 0}\gamma(\omega, T) = 0\ \forall T$. The $\gamma(\omega, T)$ are averaged over disorder by computing the mean of the interpolated linewidths over different same-size samples of each material. The spline functions are finally evaluated on the frequencies of larger samples in order to obtain their approximated anharmonic linewidths.

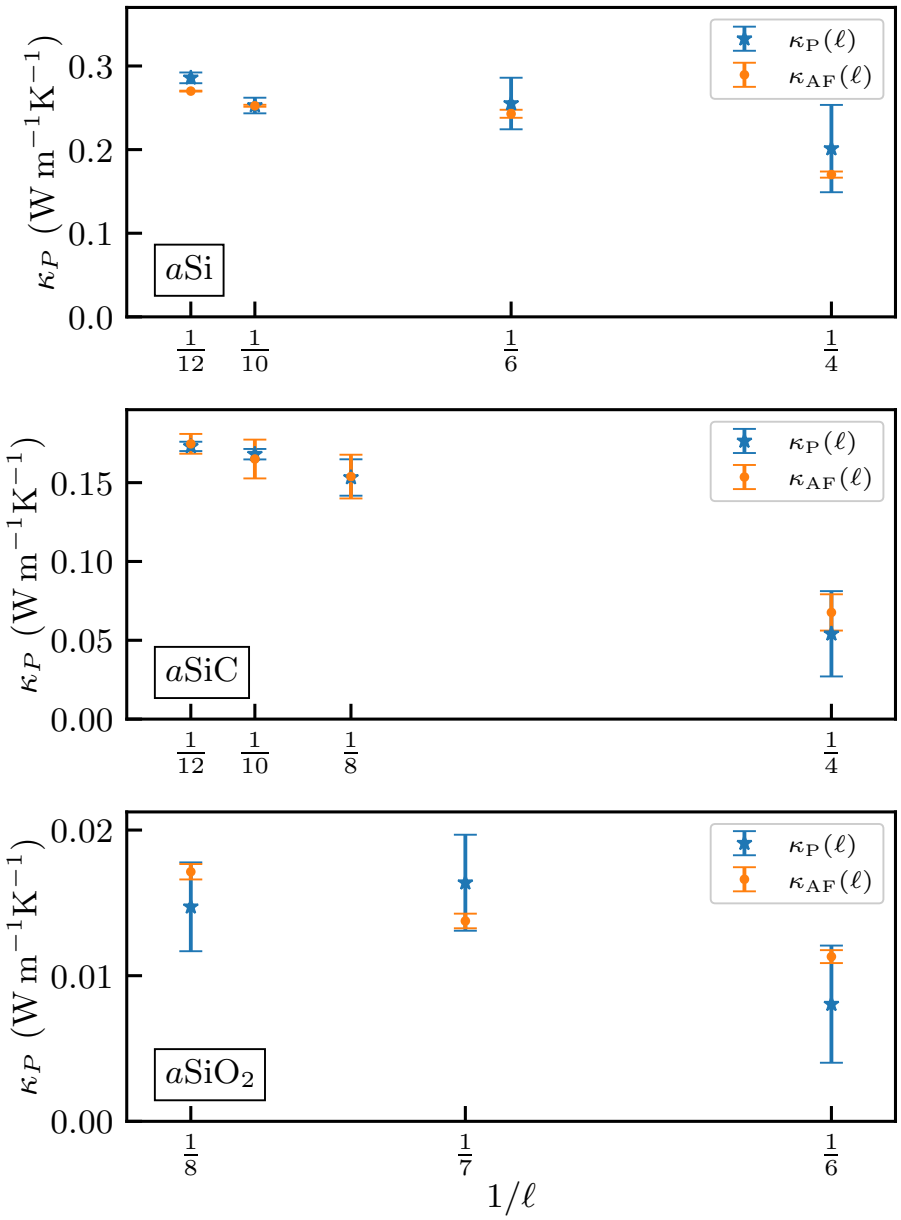

Figure B.4: Allen-Feldman propagon contribution to thermal conductivity for a fixed smearing parameter $\eta = 0.4\,\mathrm{rad/ps}$ at $T = 500\,\mathrm{K}$, shown for different system sizes. The size is indicated by $\ell = L/L_0$, representing the number of times the unit cubic cell is repeated, with each unit cell containing $N_{\mathrm{unit}} = 8, 8, 24$ atoms for aSi, aSiC, $a\mathrm{SiO_2}$, respectively. For each of the three glasses, the AF data (markers) is compared with the theoretical results (solid lines) computed using Eq. (3.10). The error bars for the AF data represent the standard deviation across ten samples of the same size, while the error bars for the theoretical results arise from the discretization of the wavevectors $\mathbf{Q}$, as described in the text.

C

COMPUTATIONAL DETAILS

For all materials, the computation of the thermal conductivity is divided into three parts: the generation of the atomic configuration in mechanical equilibrium, the computation of the IFC, and finally the computation of the lattice thermal conductivity. The first two steps involve different codes depending on the material, while thermal conductivity calculations using lattice-dynamical methods are always performed through the κALDo code [33]. The computation of the VDSF, needed by the hydrodynamic extrapolation technique, is computed through the "hydro-glass" code available on GitHub [172].

C.1 CRYSTALS

The cSi calculations are performed from first principles using DFT, following Ref. [37]. Second- and third-order IFC are obtained from standard [145–147] and third-order [173–175] Density Functional Perturbation Theory, using the `pw.x/ph.x` code in the QUANTUM ESPRESSO™ [176–178] and `D3Q` [179] codes, respectively. In the computation of the lattice thermal conductivity, a dense q-mesh of $[24, 24, 24]$ is used. Due to its computational cost, the inversion of the scattering matrix is performed using the self-consistent algorithm provided by the κALDo code.

The Li_3ClO compound is simulated in a cubic cell with edge $a_0 = 3.875$Å, using the Buckingham potential [180], and the PPPM [181] method to treat the Coulomb interaction. Second- and third-order interatomic force constants were computed with LAMMPS using a finite-difference method in a $[5, 5, 5]$ supercell. Further details on Refs. [18, 57].

C.2 GLASSES

Amorphous samples are obtained through a melt-and-quench procedure starting from a crystalline conventional cubic cell replicated ℓ times along each Cartesian direction. The molecular dynamics simulations are carried out using the Large-scale Atomic/Molecular Massively Parallel Simulator (LAMMPS [182]). The melt-and-quench procedures are performed according to the following recipes:

αSiO_2. The interatomic forces are described with the Vashishta force-field [183]. Simulations are carried out with a timestep of 1 fs. Starting from the β-cristobalite cubic conventional unit cell with a mass density of $2.20\,\mathrm{g\,cm^{-3}}$, the crystal is melted at 7000 K. The molten sample is quenched from 7000 K to 500 K in 10 ns [184, 185]. The sample is then thermalized at 500 K for 400 ps, and finally equi-

librated for 100 ps in the NVE ensemble. For each size, we randomized the seed of the thermostat to obtain ten different samples. The average mass density of the amorphous samples is 2.43 g cm^{-3}, with a standard deviation across sizes of 0.01 g cm^{-3}.

αSiC. The interatomic forces are described with the Vashishta force-field [186, 187]. Simulations are carried out with a timestep of 1 fs. For each size, the starting configuration is a crystalline cubic zinc-blend structure with a mass density of 3.22 g cm^{-3}. Following Ref. [186], the system is gradually heated from 300 K to 4000 K at constant null pressure. The solid/liquid transition is characterized by a sharp increase in the volume between 3000 and 3500 K [186]. Ten different liquid configurations are extracted every 2 ps from an NVE trajectory. The molten configurations are then quenched to 1000 K in 300 ps, and thermalized for 80 ps at constant pressure. The system is further cooled down to 500 K with the same procedure. The average mass density of the amorphous samples is 2.98 g cm^{-3}, with a standard deviation across sizes of 0.01 g cm^{-3}.

αSi. The interatomic forces are described with the Tersoff force-field [121]. Simulations are carried out with a timestep of 0.5 fs. For each size, the starting configuration is a crystalline diamond conventional unit cell replicated ℓ times along each Cartesian direction. Following Ref. [188], the crystal is melted at 6000 K and brought to 3000 K in 2 ns at fixed zero pressure. Then the system is equilibrated at 3000 K for another 2 ns. The molten sample is successively quenched from 3000 K to 2000 K in 10 ns, and finally annealed from 2000 K to 300 K at fixed volume in another 10 ns. Each glassy sample is equilibrated at 300 K for 10 ns. For each size, ten different samples are prepared according to this recipe beginning the quenching procedure from liquid configurations obtained initializing the atomic velocities with different random seeds. The average mass density of the amorphous samples is 2.275 g cm^{-3}, with a standard deviation across sizes of 0.003 g cm^{-3}. For αSi, also GKMD calculations are carried out, using the `GPUMD` code [189], where the energy flux is properly implemented for the Tersoff force-field [190]. Each thermal conductivity value is obtained through the Helfand-Einstein integration [7, 13] of the energy flux autocorrelation function. The flux is sampled every 2 fs from a canonical dynamics controlled by the Bussi-Donadio-Parrinello thermostat [191].

C.3 SIGE ALLOYS

The SiGe alloys are simulated from first principles, using the QUANTUM ESPRESSO™ [176–178] and `D3Q` [179] codes as for the silicon crystal cSi. Starting with norm-conserving pseudopotentials based on the approach of von Barth and Car [192] for both silicon and germanium, the virtual crystal pseudopotentials for intermediate concentrations are generated

using a dedicated tool within the QE distribution [176]. For all concentrations, the self-consistent calculations on the relaxed virtual diamond crystals are performed on a $[6, 6, 6]$ Monkhorst-Pack [193] mesh, with an energy cutoff of 24, Ry for the plane-wave expansion and a convergence threshold of 10^{-12}. The second- and third-order IFC are then computed with a threshold of 10^{-16}, using a $[7, 7, 7]$ and $[5, 5, 5]$ supercell, respectively. The ab initio calculations are conducted for the following set of concentrations: $x = 0, 0.1, 0.3, 0.5, 0.7, 0.9, 1$, while the lattice parameters and IFC for any other concentration are obtained by linear interpolation of the two nearest ab-initio concentrations.

We use these IFC for the vVCA calculations of anharmonic linewidths and thermal conductivity, as well as for the generation of disordered alloys in real space. For the crystalline case, we use a dense q-mesh $[28, 28, 28]$. For the disordered alloys, both in the colored and white case, the thermal conductivity and VDSF calculations are performed on sizes corresponding to $[18, 18, 18]$ and $[28, 28, 28]$ supercells, respectively. To take into account the stochastic noise of the generation of the disordered alloys, for each size the results are averaged over 4 samples.

D

DETAILS ON SPATIALLY CORRELATED SIGE ALLOYS

D.1 GENERATION OF CORRELATED MASS DISORDER

The generation of atomic configurations with correlated mass consists of two steps: firstly, a spatially correlated mass distribution using the standard algorithm from Ref. [143, 169]. The algorithm would suffice if a continuous range of mass values were available, which is not the case here. Therefore, a Monte Carlo minimization is employed to refine the solution and reduce errors arising from the highly discrete set of masses: m_{Ge} and m_{Si}. The Germanium concentration is fixed at $x = 0.5$ for all correlated configurations.

Given a desired correlation function $C(r)$, the goal is to build a residual mass distribution $\delta M(r) = M(r) - N_{atoms}^{-1} \sum_I M_I$ according to Eq. 4.9.

This can be accomplished thanks to the convolution properties of the FT, computed with the Fast Fourier Transform algorithm. In fact, the mass distribution can be obtained by imposing the following condition:

$$\delta\tilde{M}(\mathbf{q}) = \sqrt{|\tilde{C}(\mathbf{q})|} e^{i\varphi(\mathbf{q})} \tag{D.1}$$

where $\varphi(\mathbf{q})$ is an arbitrary phase. Stochastically equivalent configurations can be generated By extracting this arbitrary phase from a uniform distribution $[0, 2\pi]$, with the additional requirement of $\varphi(q) = -\varphi(-q)$ to guarantee a real $\delta M(r)$ for a crystal with inversion symmetry. Since we are interested in correlation on scales larger than the bond length, ≈ 2Å, $\delta M(r)$ is computed on the lattice, and both atoms in the unit cell are assumed to have the same mass.

Then, the $\delta M(r)$ is retrieved, By Inverse FT, and discretized:

$$\delta M^D(r_I) \propto \text{sign}(\delta M(r))$$

while conserving its variance and ensuring a zero average. Assigning m_{Ge} for positive values and m_{Si} for negative ones, or vice versa, would conclude the algorithm from Ref. [143]. Without a finer grid of mass values, e.g. Ref. [143] used 5 values, the discretization introduces noise. In order to find the optimal δM^D, the following loss function is minimized by a Monte Carlo algorithm:

$$\mathcal{L}(t) = \sum_{q \neq 0} |\tilde{C}(q) - |\delta\tilde{M}^D(q,t)|^2|$$

where t indicates the Monte Carlo step. Each Monte Carlo move consists of switching two elements i, j of $M^D(r_I) \rightleftharpoons M^D(r_J)$. $q = (0,0,0)$ is excluded by the loss function since $C(q = (0,0,0)) \propto \sum_{ij} \delta M_I \delta M_J$ cannot

be modified by the Monte Carlo move and it is determined by the average of $\delta M^D(r)$, initially imposed to zero. An example of the effect of this Monte Carlo refining is shown in Fig. D.1.

The above algorithm has been applied with a short-ranged and a long-ranged correlation function, respectively $e^{-r^2/(2\sigma^2 l_0^2)}$ and $e^{-\epsilon r}/r$. Being a the lattice parameter of the diamond crystal, the parameters indicate respectively the cubic root of the unit-cell volume $l_0 = V_0^{1/3} = (a^3/4)^{1/3}$, an adimensional parameter σ to determine the cutoff of the Gaussian, and finally ϵ is a regularization parameter order of magnitudes smaller than the inverse of our largest side L to avoid the non-analytical part of the FT of $1/r$ without significantly altering the $\sim 1/r$ behavior for $r < L$.

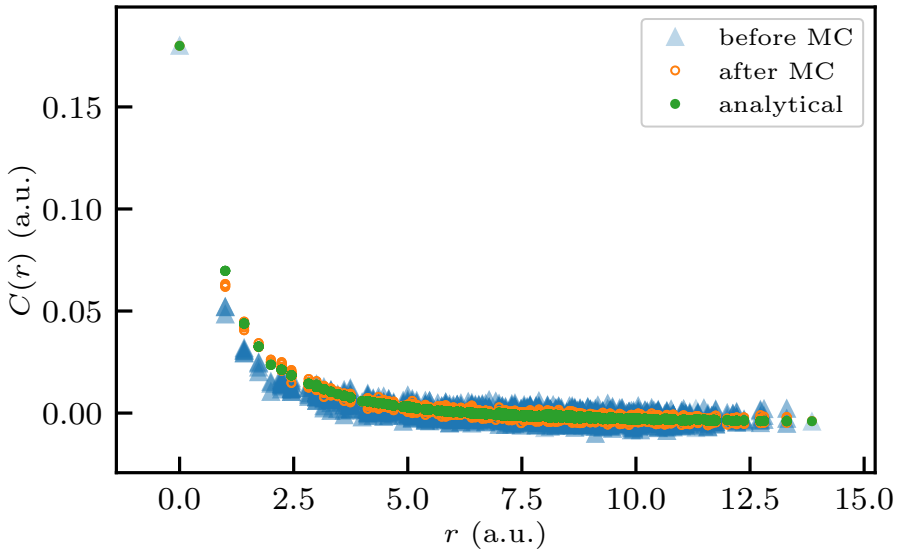

Figure D.1: Example of mass correlation distribution before and after the Monte Carlo refining procedure. All the quantities are computed on a cubic lattice with lattice parameter $a = 1$ and supercell $[16, 16, 16]$ for a desired correlation function $C(r) \propto \frac{e^{-\epsilon r}}{r}$, where $\epsilon = 10^{-4}$. Figure drawn from Ref. [37].

D.2 DETAILS ON THE HYDRODYNAMIC EXTRAPOLATION

As discussed in the previous chapter [35], ω_P plays the role of frequency separator between the acoustic crystalline-like contribution and the "diffusive" contribution computed on the disordered system. While ω_P reminds and is related to the crossover frequency between propagons and diffusons, determined with the Ioffe-Regel criterion [86], it is usually smaller and it allows more versatility of choice. The choice of ω_P is arbitrary as long as it is in a region where the real-space disordered contribution is well-converged and the conditions for the acoustic basis are satisfied, i.e., the VDSF shows well-separated longitudinal and transverse acoustic bands. This is exemplified in Fig. D.2, where the thermal

conductivity is reported as a function of ω_P, relative to the result for $\omega_P/2\pi = 5$ THz. Indeed, between 2 and 7 THz, the relative variation for three different concentrations is less than 1%.

Another key concept for the success of the hydrodynamic extrapolation is the assumption that the diffusive part of thermal conductivity is hardly affected by finite-size effects and therefore it can be computed from a disordered system of moderate size. Such an assumption is empirically verified, as shown in Fig. D.3, where κ_D is studied as a function of ℓ, the number of times the 2-atoms unit cell has been repeated in each direction.

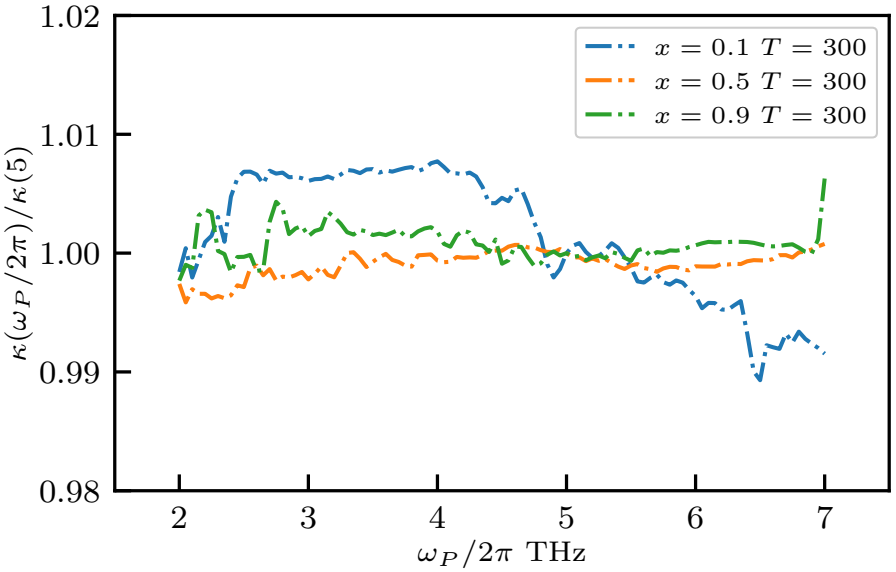

Figure D.2: Bulk lattice thermal conductivity as a function of ω_P divided by its value for $\omega_P/2\pi = 5$THz, for different concentrations at room temperature. Figure drawn from Ref. [37].

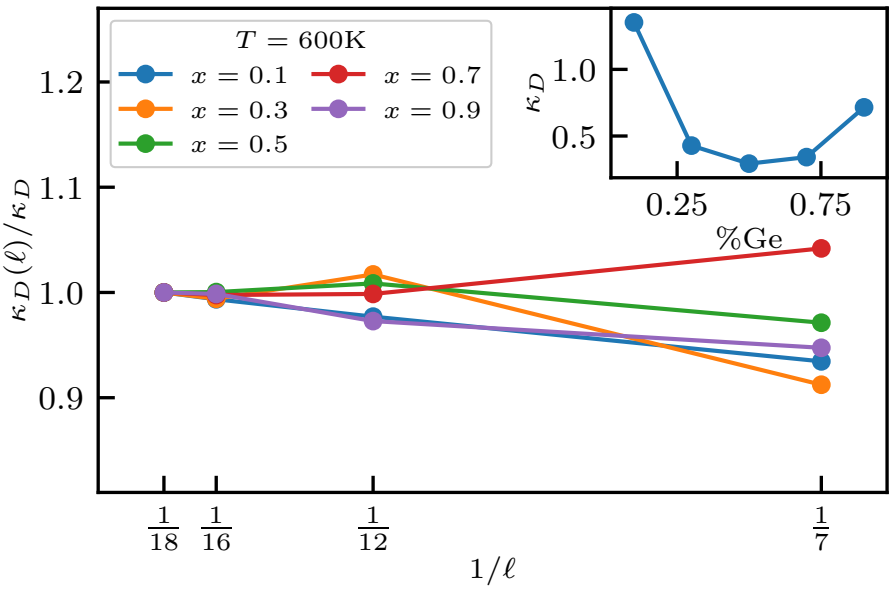

Figure D.3: Main panel: convergence of the diffusive contribution to thermal conductivity as a function of ℓ, relative to $\kappa_D = \kappa_D(\ell_{max})$, for different concentrations. Inset: the value of κ_D as a function of the %Ge concentration, in units of $Wm^{-1}K^{-1}$. $\omega_P/2\pi = 5$THz.

BIBLIOGRAPHY

[1] Lars Onsager. "Reciprocal relations in irreversible processes. I." In: *Physical review* 37.4 (1931), p. 405.

[2] Lars Onsager. "Reciprocal relations in irreversible processes. II." In: *Physical review* 38.12 (1931), p. 2265.

[3] Hendrik Brugt Gerhard Casimir. "On Onsager's principle of microscopic reversibility." In: *Reviews of Modern Physics* 17.2-3 (1945), p. 343.

[4] Melville S Green. "Markoff random processes and the statistical mechanics of time-dependent phenomena. II. Irreversible processes in fluids." In: *The Journal of chemical physics* 22.3 (1954), pp. 398–413.

[5] Ryogo Kubo. "Statistical-mechanical theory of irreversible processes. I. General theory and simple applications to magnetic and conduction problems." In: *Journal of the physical society of Japan* 12.6 (1957), pp. 570–586.

[6] Ryogo Kubo, Mario Yokota, and Sadao Nakajima. "Statistical-mechanical theory of irreversible processes. II. Response to thermal disturbance." In: *Journal of the Physical Society of Japan* 12.11 (1957), pp. 1203–1211.

[7] Stefano Baroni, Riccardo Bertossa, Loris Ercole, Federico Grasselli, and Aris Marcolongo. "Heat transport in insulators from ab initio Green-Kubo theory." In: *Handbook of materials modeling: Applications: Current and emerging materials* (2020), pp. 809–844.

[8] Sybren Ruurds De Groot and Peter Mazur. *Non-equilibrium thermodynamics*. Courier Corporation, 2013.

[9] Pablo G Debenedetti. "Fluctuation-based computer calculation of partial molar properties. I. Molecular dynamics simulation of constant volume fluctuations." In: *The Journal of chemical physics* 86.12 (1987), pp. 7126–7137. DOI: 10.1103/PhysRevLett.122.255901. URL: https://link.aps.org/doi/10.1103/PhysRevLett.122.255901.

[10] R Vogelsang and C Hoheisel. "Thermal conductivity of a binary-liquid mixture studied by molecular dynamics with use of Lennard-Jones potentials." In: *Physical Review A* 35.8 (1987), p. 3487. DOI: 10.1103/PhysRevA.35.3487. URL: https://link.aps.org/doi/10.1103/PhysRevA.35.3487.

[11] P Sindzingre, C Massobrio, G Ciccotti, and D Frenkel. "Calculation of partial enthalpies of an argon-krypton mixture by NPT molecular dynamics." In: *Chemical physics* 129.2 (1989), pp. 213–224. DOI: https://doi.org/10.1016/0301-0104(89)80007-2. URL: https://www.sciencedirect.com/science/article/pii/0301010489800072.

[12] Riccardo Bertossa, Federico Grasselli, Loris Ercole, and Stefano Baroni. "Theory and numerical simulation of heat transport in multicomponent systems." In: *Physical Review Letters* 122.25 (2019), p. 255901. DOI: 10.1103/PhysRevLett.122.255901. URL: https://link.aps.org/doi/10.1103/PhysRevLett.122.255901.

[13] Federico Grasselli and Stefano Baroni. "Invariance principles in the theory and computation of transport coefficients." In: *The European Physical Journal B* 94 (2021), pp. 1–14.

[14] Stephen Stackhouse, Lars Stixrude, and Bijaya B Karki. "Thermal conductivity of periclase (MgO) from first principles." In: *Physical review letters* 104.20 (2010), p. 208501. DOI: 10.1103/PhysRevLett.104.208501. URL: https://link.aps.org/doi/10.1103/PhysRevLett.104.208501.

[15] Loris Ercole, Aris Marcolongo, Paolo Umari, and Stefano Baroni. "Gauge invariance of thermal transport coefficients." In: *Journal of Low Temperature Physics* 185 (2016), pp. 79–86. DOI: 10.1007/s10909-016-1617-6. URL: https://doi.org/10.1007/s10909-016-1617-6.

[16] Aris Marcolongo, Loris Ercole, and Stefano Baroni. "Gauge fixing for heat-transport simulations." In: *Journal of Chemical Theory and Computation* 16.5 (2020), pp. 3352–3362.

[17] Giovanni Caldarelli, Michele Simoncelli, Nicola Marzari, Francesco Mauri, and Lara Benfatto. "Many-body Green's function approach to lattice thermal transport." In: *Phys. Rev. B* 106 (2 2022), p. 024312. DOI: 10.1103/PhysRevB.106.024312. URL: https://link.aps.org/doi/10.1103/PhysRevB.106.024312.

[18] Alfredo Fiorentino and Stefano Baroni. "From Green-Kubo to the full Boltzmann kinetic approach to heat transport in crystals and glasses." In: *Phys. Rev. B* 107 (5 2023), p. 054311. DOI: 10.1103/PhysRevB.107.054311.

[19] Giorgia Fugallo and Luciano Colombo. "Calculating lattice thermal conductivity: a synopsis." In: *Physica Scripta* 93.4 (2018), p. 043002.

[20] Loris Ercole, Riccardo Bertossa, Sebastiano Bisacchi, and Stefano Baroni. "SporTran: A code to estimate transport coefficients from the cepstral analysis of (multivariate) current time series." In: *Computer Physics Communications* 280 (2022), p. 108470.

[21] R. Peierls. "Zur kinetischen Theorie der Wärmeleitung in Kristallen." German. In: *Annalen der Physik* 395.8 (1929), pp. 1055–1101. DOI: 10.1002/andp.19293950803. URL: https://doi.org/10.1002/andp.19293950803.

[22] John M Ziman. *Electrons and phonons: the theory of transport phenomena in solids*. Oxford university press, 2001. Chap. VII.

[23] Philip B. Allen and Joseph L. Feldman. "Thermal Conductivity of Glasses: Theory and Application to Amorphous Si." In: *Phys. Rev. Lett.* 62 (6 1989), pp. 645–648. DOI: 10.1103/PhysRevLett.62.645. URL: https://link.aps.org/doi/10.1103/PhysRevLett.62.645.

[24] Philip B. Allen and Joseph L. Feldman. "Thermal conductivity of disordered harmonic solids." In: *Phys. Rev. B* 48 (17 1993), pp. 12581–12588. DOI: 10.1103/PhysRevB.48.12581. URL: https://link.aps.org/doi/10.1103/PhysRevB.48.12581.

[25] Alfredo Fiorentino, Enrico Drigo, Stefano Baroni, and Paolo Pegolo. "Unearthing the foundational role of anharmonicity in heat transport in glasses." In: *Physical Review B* 109.22 (2024), p. 224202. DOI: 10.1103/PhysRevB.109.224202.

[26] Leyla Isaeva, Giuseppe Barbalinardo, Davide Donadio, and Stefano Baroni. "Modeling heat transport in crystals and glasses from a unified lattice-dynamical approach." In: *Nat. Commun.* 10.1 (2019), p. 3853. ISSN: 2041-1723. DOI: 10.1038/s41467-019-11572-4.

[27] Michele Simoncelli, Nicola Marzari, and Francesco Mauri. "Unified theory of thermal transport in crystals and glasses." In: *Nature Physics* 15.8 (2019), pp. 809–813. DOI: 10.1038/s41567-019-0520-x. URL: https://doi.org/10.1038/s41567-019-0520-x.

[28] Michele Simoncelli, Nicola Marzari, and Francesco Mauri. "Wigner Formulation of Thermal Transport in Solids." In: *Phys. Rev. X* 12 (4 2022), p. 041011. DOI: 10.1103/PhysRevX.12.041011. URL: https://link.aps.org/doi/10.1103/PhysRevX.12.041011.

[29] Eugene Wigner. "On the quantum correction for thermodynamic equilibrium." In: *Physical review* 40.5 (1932), p. 749. DOI: 10.1103/PhysRev.40.749. URL: https://link.aps.org/doi/10.1103/PhysRev.40.749.

[30] Robert J Hardy. "Energy-flux operator for a lattice." In: *Physical Review* 132.1 (1963), p. 168. DOI: 10.1103/PhysRev.132.168. URL: https://link.aps.org/doi/10.1103/PhysRev.132.168.

[31] John W Negele. *Quantum many-particle systems*. CRC Press, 2018. DOI: https://doi.org/10.1201/9780429497926.

[32] Đorđe Dangić, Olle Hellman, Stephen Fahy, and Ivana Savić. "The origin of the lattice thermal conductivity enhancement at the ferroelectric phase transition in GeTe." In: *npj Computational Materials* 7.1 (2021), p. 57. DOI: https://doi.org/10.1038/s41524-021-00523-7.

[33] Giuseppe Barbalinardo, Zekun Chen, Nicholas W. Lundgren, and Davide Donadio. "Efficient anharmonic lattice dynamics calculations of thermal transport in crystalline and disordered solids." In: *J. Appl. Phys.* 128.13 (2020), p. 135104. DOI: 10.1063/5.0020443. URL: https://doi.org/10.1063/5.0020443.

[34] Gyaneshwar P Srivastava. *The physics of phonons*. CRC press, 2022. DOI: https://doi.org/10.1201/9781003141273.

[35] Alfredo Fiorentino, Paolo Pegolo, and Stefano Baroni. "Hydrodynamic finite-size scaling of the thermal conductivity in glasses." In: *npj Computational Materials* 9.1 (2023). ISSN: 2057-3960. DOI: 10.1038/s41524-023-01116-2.

[36] Balázs Póta, Paramvir Ahlawat, Gábor Csányi, and Michele Simoncelli. *Thermal Conductivity Predictions with Foundation Atomistic Models*. 2024. arXiv: 2408.00755 [cond-mat.mtrl-sci]. URL: https://arxiv.org/abs/2408.00755.

[37] Alfredo Fiorentino, Paolo Pegolo, Stefano Baroni, and Davide Donadio. "Effects of colored disorder on the heat conductivity of SiGe alloys from first principles." In: *arXiv preprint arXiv:2408.05155* (2024). URL: https://arxiv.org/abs/2408.05155.

[38] J. Tersoff. "Empirical interatomic potential for silicon with improved elastic properties." In: *Phys. Rev. B* 38 (14 1988), pp. 9902–9905. DOI: 10.1103/PhysRevB.38.9902. URL: https://link.aps.org/doi/10.1103/PhysRevB.38.9902.

[39] Jaroslav Fabian and Philip B Allen. "Anharmonic decay of vibrational states in amorphous silicon." In: *Physical review letters* 77.18 (1996), p. 3839. DOI: 10.1103/PhysRevLett.77.3839. URL: https://link.aps.org/doi/10.1103/PhysRevLett.77.3839.

[40] Charles Kittel. "Interpretation of the Thermal Conductivity of Glasses." In: *Phys. Rev.* 75 (6 1949), pp. 972–974. DOI: 10.1103/PhysRev.75.972. URL: https://link.aps.org/doi/10.1103/PhysRev.75.972.

[41] C Yu Clare and JJ Freeman. "Thermal conductivity and specific heat of glasses." In: *Physical Review B* 36.14 (1987), p. 7620. DOI: 10.1103/PhysRevB.36.7620. URL: https://link.aps.org/doi/10.1103/PhysRevB.36.7620.

[42] David G. Cahill, M. Katiyar, and J. R. Abelson. "Thermal conductivity of a-Si:H thin films." In: *Phys. Rev. B* 50 (9 1994), pp. 6077–6081. DOI: 10.1103/PhysRevB.50.6077. URL: https://link.aps.org/doi/10.1103/PhysRevB.50.6077.

[43] Andrea Cepellotti, Giorgia Fugallo, Lorenzo Paulatto, Michele Lazzeri, Francesco Mauri, and Nicola Marzari. "Phonon hydrodynamics in two-dimensional materials." In: *Nature communications* 6.1 (2015), p. 6400. DOI: 10.1038/ncomms7400. URL: https://doi.org/10.1038/ncomms7400.

[44] Robert Zwanzig. "Ensemble method in the theory of irreversibility." In: *The Journal of Chemical Physics* 33.5 (1960), pp. 1338–1341. DOI: 10.1063/1.1731409. URL: https://doi.org/10.1063/1.1731409.

[45] Hazime Mori. "Transport, collective motion, and Brownian motion." In: *Progress of theoretical physics* 33.3 (1965), pp. 423–455. DOI: 10.1143/PTP.33.423. URL: https://doi.org/10.1143/PTP.33.423.

[46] Rep Kubo. "The fluctuation-dissipation theorem." In: *Reports on progress in physics* 29.1 (1966), p. 255. DOI: 10.1088/0034-4885/29/1/306. URL: https://doi.org/10.1088%2F0034-4885%2F29%2F1%2F306.

[47] Dieter Forster. *Hydrodynamic fluctuations, broken symmetry, and correlation functions*. CRC Press, 2018.

[48] Ugo Fano. "Description of states in quantum mechanics by density matrix and operator techniques." In: *Reviews of modern physics* 29.1 (1957), p. 74. DOI: 10.1103/RevModPhys.29.74.

[49] Qiang Shi and Eitan Geva. "A new approach to calculating the memory kernel of the generalized quantum master equation for an arbitrary system–bath coupling." In: *The Journal of chemical physics* 119.23 (2003), pp. 12063–12076. DOI: 10.1063/1.1624830. URL: https://doi.org/10.1063/1.1624830.

[50] Ming-Liang Zhang, Being J Ka, and Eitan Geva. "Nonequilibrium quantum dynamics in the condensed phase via the generalized quantum master equation." In: *The Journal of chemical physics* 125.4 (2006). DOI: 10.1063/1.2218342. URL: https://doi.org/10.1063/1.2218342.

[51] Andrés Montoya-Castillo and David R Reichman. "Approximate but accurate quantum dynamics from the Mori formalism: I. Nonequilibrium dynamics." In: *The Journal of Chemical Physics* 144.18 (2016). DOI: 10.1063/1.4948408. URL: https://doi.org/10.1063/1.4948408.

[52] Andrés Montoya-Castillo and David R Reichman. "Approximate but accurate quantum dynamics from the Mori formalism. II. Equilibrium time correlation functions." In: *The Journal of chemical physics* 146.8 (2017). DOI: 10.1063/1.4975388. URL: https://doi.org/10.1063/1.4975388.

[53] Lorenzo Monacelli, Raffaello Bianco, Marco Cherubini, Matteo Calandra, Ion Errea, and Francesco Mauri. "The stochastic self-consistent harmonic approximation: calculating vibrational properties of materials with full quantum and anharmonic effects." In: *Journal of Physics: Condensed Matter* 33.36 (2021), p. 363001. DOI: 10.1088/1361-648X/ac066b. URL: https://dx.doi.org/10.1088/1361-648X/ac066b.

[54] Đorđe Dangić, Giovanni Caldarelli, Raffaello Bianco, Ivana Savić, and Ion Errea. "Lattice thermal conductivity in the anharmonic overdamped regime." In: *arXiv preprint arXiv:2410.13485* (2024). URL: https://arxiv.org/abs/2410.13485.

[55] Michele Simoncelli. *Thermal transport beyond Fourier, and beyond Boltzmann*. Tech. rep. EPFL, 2021. DOI: 10.5075/epfl-thesis-8158. URL: https://infoscience.epfl.ch/handle/20.500.14299/178378.

[56] Gerald D Mahan. *Many-particle physics*. Springer Science & Business Media, 2013.

[57] Paolo Pegolo, Stefano Baroni, and Federico Grasselli. "Temperature-and vacancy-concentration-dependence of heat transport in Li3ClO from multi-method numerical simulations." In: *npj Computational Materials* 8.1 (2022), p. 24. DOI: 10.1038/s41524-021-00693-4. URL: https://doi.org/10.1038/s41524-021-00693-4.

[58] Allan Griffin. "Brillouin Light Scattering from Crystals in the Hydrodynamic Region." In: *Rev. Mod. Phys.* 40 (1 1968), pp. 167–205. DOI: 10.1103/RevModPhys.40.167. URL: https://link.aps.org/doi/10.1103/RevModPhys.40.167.

[59] Y. M. Beltukov, V. I. Kozub, and D. A. Parshin. "Ioffe-Regel criterion and diffusion of vibrations in random lattices." In: *Phys. Rev. B* 87 (13 2013), p. 134203. DOI: 10.1103/PhysRevB.87.134203. URL: https://link.aps.org/doi/10.1103/PhysRevB.87.134203.

[60] W A Phillips. "Two-level states in glasses." In: *Rep. Progr. Phys.* 50.12 (1987), p. 1657. DOI: 10.1088/0034-4885/50/12/003.

[61] U. Buchenau et al. "Interaction of soft modes and sound waves in glasses." In: *Phys. Rev. B* 46 (5 1992), pp. 2798–2808. DOI: 10.1103/PhysRevB.46.2798. URL: https://link.aps.org/doi/10.1103/PhysRevB.46.2798.

[62] Vassiliy Lubchenko and Peter G Wolynes. "The origin of the boson peak and thermal conductivity plateau in low-temperature glasses." In: *PNAS* 100.4 (2003), pp. 1515–1518. DOI: 10.1073/pnas.252786999.

[63] Walter Schirmacher. "Thermal conductivity of glassy materials and the "boson peak"." In: *Europhys. Lett.* 73.6 (2006), p. 892. DOI: 10.1209/epl/i2005-10471-9.

[64] Joseph L. Feldman, Mark D. Kluge, Philip B. Allen, and Frederick Wooten. "Thermal conductivity and localization in glasses: Numerical study of a model of amorphous silicon." In: *Phys. Rev. B* 48 (17 1993), pp. 12589–12602. DOI: 10.1103/PhysRevB.48.12589. URL: https://link.aps.org/doi/10.1103/PhysRevB.48.12589.

[65] Sergei Shenogin, Arun Bodapati, Pawel Keblinski, and Alan JH McGaughey. "Predicting the thermal conductivity of inorganic and polymeric glasses: The role of anharmonicity." In: *J. Appl. Phys.* 105.3 (2009), p. 034906. DOI: 10.1063/1.3073954.

[66] Michele Simoncelli, Francesco Mauri, and Nicola Marzari. "Thermal conductivity of glasses: first-principles theory and applications." In: *NPJ Comput. Mater.* 9.1 (2023), p. 106. URL: https://doi.org/10.1038/s41524-023-01033-4.

[67] Yuping He, Davide Donadio, and Giulia Galli. "Heat transport in amorphous silicon: Interplay between morphology and disorder." In: *Appl. Phys. Lett.* 98.14 (2011), p. 144101. ISSN: 0003-6951. DOI: 10.1063/1.3574366.

[68] Jaeyun Moon, Benoit Latour, and Austin J. Minnich. "Propagating elastic vibrations dominate thermal conduction in amorphous silicon." In: *Phys. Rev. B* 97 (2 2018), p. 024201. DOI: 10.1103/PhysRevB.97.024201. URL: https://link.aps.org/doi/10.1103/PhysRevB.97.024201.

[69] Philip B Allen, Joseph L Feldman, Jaroslav Fabian, and Frederick Wooten. "Diffusons, locons and propagons: Character of atomic vibrations in amorphous Si." In: *Phil. Mag. B* 79.11-12 (1999), pp. 1715–1731. DOI: 10.1080/13642819908223054. URL: https://doi.org/10.1080/13642819908223054.

[70] Jeffrey Goldstone. "Field theories with Superconductor solutions." In: *Riv. del Nuovo Cim.(1955-1965)* 19 (1961), pp. 154–164. DOI: 10.1007/BF02812722.

[71] Joseph L. Feldman, Philip B. Allen, and Scott R. Bickham. "Numerical study of low-frequency vibrations in amorphous silicon." In: *Phys. Rev. B* 59 (5 1999), pp. 3551–3559. DOI: 10.1103/PhysRevB.59.3551. URL: https://link.aps.org/doi/10.1103/PhysRevB.59.3551.

[72] Roger Haydock. "The Recursive Solution of the Schrödinger Equation." In: ed. by Henry Ehrenreich, Frederick Seitz, and David Turnbull. Vol. 35. Solid State Physics. Academic Press, 1980, pp. 215–294. DOI: https://doi.org/10.1016/S0081-1947(08)60505-6. URL: https://www.sciencedirect.com/science/article/pii/S0081194708605056.

[73] Nathalie Vast and Stefano Baroni. "Effects of isotopic disorder on the Raman spectra of crystals: Theory and ab initio calculations for diamond and germanium." In: *Phys. Rev. B* 61 (14 2000), pp. 9387–9392. DOI: 10.1103/PhysRevB.61.9387. URL: https://link.aps.org/doi/10.1103/PhysRevB.61.9387.

[74] Josef Jäckle. "On the ultrasonic attenuation in glasses at low temperatures." In: *Z. Phys.* 257.3 (1972), pp. 212–223. DOI: 10.1007/BF01401204.

[75] Ping Sheng and Minyao Zhou. "Heat conductivity of amorphous solids: Simulation results on model structures." In: *Science* 253.5019 (1991), pp. 539–542. DOI: 10.1126/science.253.5019.539.

[76] U. Buchenau, Yu. M. Galperin, V. L. Gurevich, D. A. Parshin, M. A. Ramos, and H. R. Schober. "Interaction of soft modes and sound waves in glasses." In: *Phys. Rev. B* 46 (5 1992), pp. 2798–2808. DOI: 10.1103/PhysRevB.46.2798. URL: https://link.aps.org/doi/10.1103/PhysRevB.46.2798.

[77] Anthony J. Leggett and Dervis C. Vural. ""Tunneling Two-Level Systems" Model of the Low-Temperature Properties of Glasses: Are "Smoking-Gun" Tests Possible?" In: *J. Phys. Chem. B* 117.42 (2013), pp. 12966–12971. DOI: 10.1021/jp402222g.

[78] Vassiliy Lubchenko and Peter G. Wolynes. "The origin of the boson peak and thermal conductivity plateau in low-temperature glasses." In: *Proc. Natl. Acad. Sci. U.S.A.* 100.4 (2003), pp. 1515–1518. DOI: 10.1073/pnas.252786999.

[79] Carl Ganter and Walter Schirmacher. "Rayleigh scattering, long-time tails, and the harmonic spectrum of topologically disordered systems." In: *Phys. Rev. B* 82 (9 2010), p. 094205. DOI: 10.1103/PhysRevB.82.094205. URL: https://link.aps.org/doi/10.1103/PhysRevB.82.094205.

[80] Hideyuki Mizuno, Giancarlo Ruocco, and Stefano Mossa. "Sound damping in glasses: Interplay between anharmonicities and elastic heterogeneities." In: *Phys. Rev. B* 101 (17 2020), p. 174206. DOI: 10.1103/PhysRevB.101.174206. URL: https://link.aps.org/doi/10.1103/PhysRevB.101.174206.

[81] S.-M. Lee and David G. Cahill. "Heat transport in thin dielectric films." In: *Journal of Applied Physics* 81.6 (1997), pp. 2590–2595. ISSN: 0021-8979. DOI: 10.1063/1.363923. URL: https://doi.org/10.1063/1.363923.

[82] B. L. Zink, R. Pietri, and F. Hellman. "Thermal Conductivity and Specific Heat of Thin-Film Amorphous Silicon." In: *Phys. Rev. Lett.* 96 (5 2006), p. 055902. DOI: 10.1103/PhysRevLett.96.055902. URL: https://link.aps.org/doi/10.1103/PhysRevLett.96.055902.

[83] Ho-Soon Yang, David G. Cahill, X. Liu, J. L. Feldman, R. S. Crandall, B. A. Sperling, and J. R. Abelson. "Anomalously high thermal conductivity of amorphous Si deposited by hot-wire chemical vapor deposition." In: *Phys. Rev. B* 81 (10 2010), p. 104203. DOI: 10.1103/PhysRevB.81.104203. URL: https://link.aps.org/doi/10.1103/PhysRevB.81.104203.

[84] Jeffrey L. Braun, Christopher H. Baker, Ashutosh Giri, Mirza Elahi, Kateryna Artyushkova, Thomas E. Beechem, Pamela M. Norris, Zayd C. Leseman, John T. Gaskins, and Patrick E. Hopkins. "Size effects on the thermal conductivity of amorphous silicon thin films." In: *Phys. Rev. B* 93 (14 2016), p. 140201. DOI: 10.1103/PhysRevB.93.140201. URL: https://link.aps.org/doi/10.1103/PhysRevB.93.140201.

[85] SN Taraskin and SR Elliott. "Propagation of plane-wave vibrational excitations in disordered systems." In: *Phys. Rev. B* 61.18 (2000), p. 12017. DOI: 10.1103/PhysRevB.61.12017.

[86] A. F. Ioffe and A. R. Regel. In: *Progresses in Semiconductors*. Ed. by A. F. Gibson. Vol. 4. Heywood, London, 1960, p. 237.

[87] C Masciovecchio, G Baldi, S Caponi, L Comez, S Di Fonzo, D Fioretto, A Fontana, A Gessini, SC Santucci, F Sette, et al. "Evidence for a crossover in the frequency dependence of the acoustic attenuation in vitreous silica." In: *Physical review letters* 97.3 (2006), p. 035501.

[88] Giacomo Baldi, Valentina M Giordano, and Giulio Monaco. "Elastic anomalies at terahertz frequencies and excess density of vibrational states in silica glass." In: *Phys. Rev. B* 83.17 (2011), p. 174203. DOI: 10.1103/PhysRevB.83.174203.

[89] L. D. Landau, E. M. Lifshitz, J. B. Sykes, W. H. Reid, and Ellis H. Dill. *Theory of Elasticity: Vol. 7 of Course of Theoretical Physics*. Vol. 13. 7. AIP Publishing, 1960, pp. 44–46. DOI: 10.1063/1.3057037.

[90] Matteo Baggioli and Alessio Zaccone. "Theory of sound attenuation in amorphous solids from nonaffine motions." In: *Journal of Physics: Condensed Matter* 34.21 (2022), p. 215401.

[91] Leo P Kadanoff and Paul C Martin. "Hydrodynamic equations and correlation functions." In: *Ann. Phys.* 24 (1963), pp. 419–469. DOI: 10.1006/aphy.2000.6023.

[92] A Akhieser. "On the absorption of sound in solids." In: *J. Phys.(Ussr)* 1 (1939), p. 277.

[93] TO Woodruff and H Ehrenreich. "Absorption of sound in insulators." In: *Physical Review* 123.5 (1961), p. 1553. DOI: 10.1103/PhysRev.123.1553. URL: https://link.aps.org/doi/10.1103/PhysRev.123.1553.

[94] Maria G Izzo, Giancarlo Ruocco, and Stefano Cazzato. "The mixing of polarizations in the acoustic excitations of disordered media with local isotropy." In: *Front. Phys.* 6 (2018), p. 108. DOI: 10.3389/fphy.2018.00108.

[95] M. G. Izzo, B. Wehinger, S. Cazzato, A. Matic, C. Masciovecchio, A. Gessini, and G. Ruocco. "Rayleigh scattering and disorder-induced mixing of polarizations in amorphous solids at the nanoscale: 1-octyl-3-methylimidazolium chloride glass." In: *Phys. Rev. B* 102 (21 2020), p. 214309. DOI: 10.1103/PhysRevB.102.214309. URL: https://link.aps.org/doi/10.1103/PhysRevB.102.214309.

[96] Jivtesh Garg, Nicola Bonini, Boris Kozinsky, and Nicola Marzari. "Role of Disorder and Anharmonicity in the Thermal Conductivity of Silicon-Germanium Alloys: A First-Principles Study." In: *Phys. Rev. Lett.* 106 (4 2011), p. 045901. DOI: 10.1103/PhysRevLett.106.045901. URL: https://link.aps.org/doi/10.1103/PhysRevLett.106.045901.

[97] GD Mahan. "Effect of atomic isotopes on phonon modes." In: *Phys. Rev. B* 100.2 (2019), p. 024307. DOI: 10.1103/PhysRevB.100.024307.

[98] Philip B Allen and Jonathan Kelner. "Evolution of a vibrational wave packet on a disordered chain." In: *Am. J. Phys.* 66.6 (1998), pp. 497–506. DOI: 10.1119/1.18890.

[99] Hideyuki Mizuno, Stefano Mossa, and Jean-Louis Barrat. "Acoustic excitations and elastic heterogeneities in disordered solids." In: *Proceedings of the National Academy of Sciences* 111.33 (2014), pp. 11949–11954. DOI: 10.1073/pnas.1409490111. URL: https://www.pnas.org/doi/abs/10.1073/pnas.1409490111.

[100] Constantin Tomaras, Bernhard Schmid, and Walter Schirmacher. "Anharmonic elasticity theory for sound attenuation in disordered solids with fluctuating elastic constants." In: *Phys. Rev. B* 81 (10 2010), p. 104206. DOI: 10.1103/PhysRevB.81.104206. URL: https://link.aps.org/doi/10.1103/PhysRevB.81.104206.

[101] Conyers Herring. "Role of Low-Energy Phonons in Thermal Conduction." In: *Phys. Rev.* 95 (4 1954), pp. 954–965. DOI: 10.1103/PhysRev.95.954. URL: https://link.aps.org/doi/10.1103/PhysRev.95.954.

[102] C.C. Paige. "Accuracy and effectiveness of the Lanczos algorithm for the symmetric eigenproblem." In: *Linear Algebra Appl.* 34 (1980), pp. 235–258. DOI: 10.1016/0024-3795(80)90167-6.

[103] Jason M. Larkin and Alan J. H. McGaughey. "Thermal conductivity accumulation in amorphous silica and amorphous silicon." In: *Phys. Rev. B* 89 (14 2014), p. 144303. DOI: 10.1103/PhysRevB.89.144303.

[104] Jaeyun Moon, Raphaël P. Hermann, Michael E. Manley, Ahmet Alatas, Ayman H. Said, and Austin J. Minnich. "Thermal acoustic excitations with atomic-scale wavelengths in amorphous silicon." In: *Phys. Rev. Mater.* 3 (6 2019), p. 065601. DOI: 10.1103/PhysRevMaterials.3.065601. URL: https://link.aps.org/doi/10.1103/PhysRevMaterials.3.065601.

[105] Augustus Matthiessen and Moritz von Bose. "On the influence of temperature on the electric conducting power of metals." In: *Philos. Trans. R. Soc.* 152 (1862), pp. 1–27. DOI: 10.1098/rstl.1862.0001.

[106] ET Swartz and RO Pohl. "Thermal resistance at interfaces." In: *Appl. Phys. Lett.* 51.26 (1987), pp. 2200–2202.

[107] Xiao Liu, J. L. Feldman, D. G. Cahill, R. S. Crandall, N. Bernstein, D. M. Photiadis, M. J. Mehl, and D. A. Papaconstantopoulos. "High Thermal Conductivity of a Hydrogenated Amorphous Silicon Film." In: *Phys. Rev. Lett.* 102 (3 2009), p. 035901. DOI: 10.1103/PhysRevLett.102.035901. URL: https://link.aps.org/doi/10.1103/PhysRevLett.102.035901.

[108] P. G. Klemens. "The thermal conductivity of dielectric solids at low temperatures (theoretical)." In: *Proceedings of the Royal Society of London. Series A. Mathematical and Physical Sciences* 208.1092 (1951), pp. 108–133.

[109] Ludovic Berthier and Giulio Biroli. "Theoretical perspective on the glass transition and amorphous materials." In: *Rev. Mod. Phys.* 83 (2 2011), pp. 587–645. DOI: 10.1103/RevModPhys.83.587. URL: https://link.aps.org/doi/10.1103/RevModPhys.83.587.

[110] J. Jäckle. "On the glass transition and the residual entropy of glasses." In: *Phil. Mag. B* 44.5 (1981), pp. 533–545. DOI: 10.1080/01418638108224037.

[111] Pablo G. Debenedetti and Frank H. Stillinger. "Supercooled liquids and the glass transition." In: *Nature* 410.6825 (2001), pp. 259–267. ISSN: 1476-4687. DOI: 10.1038/35065704. URL: https://doi.org/10.1038/35065704.

[112] Ting Liang, Penghua Ying, Ke Xu, Zhenqiang Ye, Chao Ling, Zheyong Fan, and Jianbin Xu. "Mechanisms of temperature-dependent thermal transport in amorphous silica from machine-learning molecular dynamics." In: *Physical Review B* 108.18 (2023), p. 184203.

[113] Paolo Pegolo and Federico Grasselli. "Thermal transport of glasses via machine learning driven simulations." In: *Frontiers in Materials* 11 (2024). ISSN: 2296-8016. DOI: 10.3389/fmats.2024.1369034. URL: https://www.frontiersin.org/articles/10.3389/fmats.2024.1369034.

[114] Han Wang, Linfeng Zhang, Jiequn Han, and E Weinan. "DeePMD-kit: A deep learning package for many-body potential energy representation and molecular dynamics." In: *Computer Physics Communications* 228 (2018), pp. 178–184. DOI: 10.1016/j.cpc.2018.03.016. URL: https://doi.org/10.1016/j.cpc.2018.03.016.

[115] Denghui Lu, Han Wang, Mohan Chen, Lin Lin, Roberto Car, E Weinan, Weile Jia, and Linfeng Zhang. "86 PFLOPS deep potential molecular dynamics simulation of 100 million atoms with ab initio accuracy." In: *Computer Physics Communications* 259 (2021), p. 107624. DOI: https://doi.org/10.1016/j.cpc.2020.107624. URL: https://www.sciencedirect.com/science/article/pii/S001046552030299X.

[116] Jinzhe Zeng, Duo Zhang, Denghui Lu, Pinghui Mo, Zeyu Li, Yixiao Chen, Marián Rynik, Li'ang Huang, Ziyao Li, Shaochen Shi, et al. "DeePMD-kit v2: A software package for deep potential models." In: *The Journal of Chemical Physics* 159.5 (2023). DOI: 10.1063/5.0155600. URL: https://doi.org/10.1063/5.0155600.

[117] Linfeng Zhang, Jiequn Han, Han Wang, Wissam Saidi, Roberto Car, et al. "End-to-end symmetry preserving inter-atomic potential energy model for finite and extended systems." In: *Advances in neural information processing systems* 31 (2018).

[118] Zheyong Fan, Zezhu Zeng, Cunzhi Zhang, Yanzhou Wang, Keke Song, Haikuan Dong, Yue Chen, and Tapio Ala-Nissila. "Neuroevolution machine learning potentials: Combining high accuracy and low cost in atomistic simulations and application to heat transport." In: *Physical Review B* 104.10 (2021), p. 104309. DOI: 10.1103/PhysRevB.104.104309. URL: https://link.aps.org/doi/10.1103/PhysRevB.104.104309.

[119] Shinji Munetoh, Teruaki Motooka, Koji Moriguchi, and Akira Shintani. "Interatomic potential for Si–O systems using Tersoff parameterization." In: *Computational Materials Science* 39.2 (2007), pp. 334–339.

[120] Albert P Bartók, James Kermode, Noam Bernstein, and Gábor Csányi. "Machine learning a general-purpose interatomic potential for silicon." In: *Physical Review X* 8.4 (2018), p. 041048. DOI: 10.1103/PhysRevX.8.041048. URL: https://link.aps.org/doi/10.1103/PhysRevX.8.041048.

[121] Jerry Tersoff. "Empirical interatomic potential for silicon with improved elastic properties." In: *Phys. Rev. B* 38.14 (1988), p. 9902. DOI: 10.1103/PhysRevB.38.9902.

[122] Sasaank Bandi, Chao Jiang, and Chris A Marianetti. "Benchmarking machine learning interatomic potentials via phonon anharmonicity." In: *Machine Learning: Science and Technology* 5.3 (2024), p. 030502. DOI: 10.1088/2632-2153/ad674a. URL: https://dx.doi.org/10.1088/2632-2153/ad674a.

[123] G. Jeffrey Snyder and Eric S. Toberer. "Complex thermoelectric materials." In: *Nature Mater* 7.2 (2008), pp. 105–114. ISSN: 1476-4660. DOI: 10.1038/nmat2090. URL: https://www.nature.com/articles/nmat2090 (visited on 01/24/2023).

[124] Davide Beretta, Neophytos Neophytou, James M. Hodges, Mercouri G. Kanatzidis, Dario Narducci, Marisol Martin-Gonzalez, Matt Beekman, Benjamin Balke, Giacomo Cerretti, Wolfgang Tremel, et al. "Thermoelectrics: From history, a window to the future." In: *Materials Science and Engineering: R: Reports* 138 (2019), p. 100501. ISSN: 0927796X. DOI: 10.1016/j.mser.2018.09.001. URL: https://linkinghub.elsevier.com/retrieve/pii/S0927796X18301566 (visited on 09/08/2021).

[125] Vincenzo Pecunia, S. Ravi P. Silva, Jamie D. Phillips, Elisa Artegiani, Alessandro Romeo, Hongjae Shim, Jongsung Park, Jin Hyeok Kim, Jae Sung Yun, Gregory C. Welch, et al. "Roadmap on energy harvesting materials." In: *J. Phys. Mater.* 6.4 (2023). Publisher: IOP Publishing, p. 042501. ISSN: 2515-7639. DOI: 10.1088/2515-7639/acc550. URL: https://dx.doi.org/10.1088/2515-7639/acc550 (visited on 02/17/2024).

[126] MC Steele and FD Rosi. "Thermal conductivity and thermoelectric power of Germanium-Silicon alloys." In: *Journal of Applied Physics* 29.11 (1958), pp. 1517–1520.

[127] JP Dismukes, L Ekstrom, EF Steigmeier, I Kudman, and DS Beers. "Thermal and electrical properties of heavily doped Ge-Si alloys up to 1300 K." In: *Journal of Applied Physics* 35.10 (1964), pp. 2899–2907.

[128] A. Stranz, J. Kähler, A. Waag, and E. Peiner. "Thermoelectric Properties of High-Doped Silicon from Room Temperature to 900K." In: *J. Electron. Mater.* 42.7 (2013), pp. 2381–2387. ISSN: 1543-186X. DOI: 10.1007/s11664-013-2508-0. URL: https://doi.org/10.1007/s11664-013-2508-0 (visited on 07/26/2024).

[129] Konstanze R Hahn, Claudio Melis, Fabio Bernardini, and Luciano Colombo. "Intrinsic thermoelectric figure of merit of bulk compositional SiGe alloys: A first-principles study." In: *Physical Review Materials* 5.6 (2021), p. 065403.

[130] RK Kremer, K Graf, M Cardona, GG Devyatykh, AV Gusev, AM Gibin, AV Inyushkin, AN Taldenkov, and H-J Pohl. "Thermal conductivity of isotopically enriched 28Si: revisited." In: *Solid state communications* 131.8 (2004), pp. 499–503.

[131] Yuping He, Ivana Savić, Davide Donadio, and Giulia Galli. "Lattice thermal conductivity of semiconducting bulk materials: atomistic simulations." In: *Phys. Chem. Chem. Phys.* 14.47 (2012), p. 16209. ISSN: 1463-9076, 1463-9084. DOI: 10.1039/c2cp42394d. URL: http://xlink.rsc.org/?DOI=c2cp42394d (visited on 09/15/2021).

[132] Konstanze R Hahn, Claudio Melis, Fabio Bernardini, and Luciano Colombo. "Engineering the thermal conductivity of doped SiGe by mass variance: a first-principles proof of concept." In: *Frontiers in Mechanical Engineering* 7 (2021), p. 712989.

[133] Bruno Lorenzi, Riccardo Dettori, Marc T. Dunham, Claudio Melis, Rita Tonini, Luciano Colombo, Aditya Sood, Kenneth E. Goodson, and Dario Narducci. "Phonon Scattering in Silicon by Multiple Morphological Defects: A Multiscale Analysis." In: *Journal of Elec Materi* 47.9 (2018), pp. 5148–5157. ISSN: 0361-5235, 1543-186X. DOI: 10.1007/s11664-018-6337-z. URL: http://link.springer.com/10.1007/s11664-018-6337-z (visited on 09/12/2021).

[134] Shiyun Xiong, Daniele Selli, Sanghamitra Neogi, and Davide Donadio. "Native surface oxide turns alloyed silicon membranes into nanophononic metamaterials with ultralow thermal conductivity." In: *Phys. Rev. B* 95.18 (2017), p. 180301. DOI: 10.1103/PhysRevB.95.180301. URL: http://link.aps.org/doi/10.1103/PhysRevB.95.180301 (visited on 09/08/2021).

[135] Stefano De Gironcoli, Paolo Giannozzi, and Stefano Baroni. "Structure and thermodynamics of Si x Ge 1- x alloys from ab initio Monte Carlo simulations." In: *Physical review letters* 66.16 (1991), p. 2116.

[136] Nicola Marzari, Stefano de Gironcoli, and Stefano Baroni. "Structure and phase stability of Ga x In 1- x P solid solutions from computational alchemy." In: *Physical review letters* 72.25 (1994), p. 4001.

[137] X. W. Wang, H. Lee, Y. C. Lan, G. H. Zhu, G. Joshi, D. Z. Wang, J. Yang, A. J. Muto, M. Y. Tang, J. Klatsky, et al. "Enhanced thermoelectric figure of merit in nanostructured n-type silicon germanium bulk alloy." In: *Applied Physics Letters* 93.19 (2008). ISSN: 0003-6951. DOI: 10.1063/1.3027060. URL: https://doi.org/10.1063/1.3027060 (visited on 06/17/2024).

[138] Davide Donadio. "Advances in the optimization of silicon-based thermoelectrics: a theory perspective." In: *Current Opinion in Green and Sustainable Chemistry* 17 (2019), pp. 35–41.

[139] Sivaiah Bathula, M Jayasimhadri, Nidhi Singh, AK Srivastava, Jiji Pulikkotil, Ajay Dhar, and RC Budhani. "Enhanced thermoelectric figure-of-merit in spark plasma sintered nanostructured n-type SiGe alloys." In: *Applied Physics Letters* 101.21 (2012), p. 213902.

[140] Ivana Savić, Davide Donadio, François Gygi, and Giulia Galli. "Dimensionality and heat transport in Si-Ge superlattices." In: *Applied Physics Letters* 102.7 (2013), p. 073113.

[141] Pablo Ferrando-Villalba, Aitor F. Lopeandía, Francesc Xavier Alvarez, Biplab Paul, Carla de Tomás, Maria Isabel Alonso, Miquel Garriga, Alejandro R. Goñi, Jose Santiso, Gemma Garcia, et al. "Tailoring thermal conductivity by engineering compositional gradients in Si1-x Ge x superlattices." In: *Nano Res.* 8.9 (2015),

pp. 2833–2841. ISSN: 1998-0124, 1998-0000. DOI: 10.1007/s12274-015-0788-9. URL: http://link.springer.com/10.1007/s12274-015-0788-9 (visited on 09/08/2021).

[142] P. Ferrando-Villalba, Shunda Chen, A. F. Lopeandía, F. X. Alvarez, M. I. Alonso, M. Garriga, J. Santiso, G. Garcia, A. R. Goñi, D. Donadio, et al. "Beating the Thermal Conductivity Alloy Limit Using Long-Period Compositionally Graded Si $_{1-x}$ Ge $_x$ Superlattices." In: *J. Phys. Chem. C* 124.36 (2020), pp. 19864–19872. ISSN: 1932-7447, 1932-7455. DOI: 10.1021/acs.jpcc.0c06410. URL: https://pubs.acs.org/doi/10.1021/acs.jpcc.0c06410 (visited on 09/10/2021).

[143] Simon Thébaud, Lucas Lindsay, and Tom Berlijn. "Breaking Rayleigh's law with spatially correlated disorder to control phonon transport." In: *Physical Review Letters* 131.2 (2023), p. 026301.

[144] D Chaney, A Castellano, A Bosak, J Bouchet, F Bottin, B Dorado, L Paolasini, S Rennie, Christopher Bell, R Springell, et al. "Tuneable correlated disorder in alloys." In: *Physical Review Materials* 5.3 (2021), p. 035004.

[145] S Baroni, P Giannozzi, and A Testa. "Green's-Function Approach to Linear Response in Solids." In: *Phys. Rev. Lett.* 58.18 (1987), pp. 1861–1864. DOI: 10.1103/PhysRevLett.58.1861.

[146] P Giannozzi, S de Gironcoli, P Pavone, and S Baroni. "Ab Initio Calculation of Phonon Dispersions in Semiconductors." In: *Phys. Rev. B* 43.9 (1991), pp. 7231–7242. DOI: 10.1103/PhysRevB.43.7231.

[147] Stefano Baroni, Stefano De Gironcoli, Andrea Dal Corso, and Paolo Giannozzi. "Phonons and related crystal properties from density-functional perturbation theory." In: *Reviews of modern Physics* 73.2 (2001), p. 515.

[148] Mi I Alonso and K Winer. "Raman spectra of c-Si 1- x Ge x alloys." In: *Physical Review B* 39.14 (1989), p. 10056.

[149] Peter Brüesch. *Phonons: Theory and Experiments II: Experiments and Interpretation of Experimental Results*. Springer Berlin Heidelberg, 1986. ISBN: 9783642522635. DOI: 10.1007/978-3-642-52263-5. URL: http://dx.doi.org/10.1007/978-3-642-52263-5.

[150] Michele Lazzeri and Francesco Mauri. "First-Principles Calculation of Vibrational Raman Spectra in Large Systems: Signature of Small Rings in Crystalline S i O 2." In: *Physical review letters* 90.3 (2003), p. 036401.

[151] SA Prosandeev, U Waghmare, Igor Levin, and J Maslar. "First-order Raman spectra of A B 1/ 2′ B 1/ 2 ″O 3 double perovskites." In: *Physical Review B* 71.21 (2005), p. 214307.

[152] PM Mooney, FH Dacol, JC Tsang, and JO Chu. "Raman scattering analysis of relaxed Ge x Si1- x alloy layers." In: *Applied Physics Letters* 62.17 (1993), pp. 2069–2071.

[153] D Rouchon, M Mermoux, F Bertin, and JM Hartmann. "Germanium content and strain in Si1- xGex alloys characterized by Raman spectroscopy." In: *Journal of crystal growth* 392 (2014), pp. 66–73.

[154] Stefano de Gironcoli and Stefano Baroni. "Effects of disorder on the vibrational properties of SiGe alloys: failure of mean-field approximations." In: *Physical review letters* 69.13 (1992), p. 1959.

[155] B Schrader, A Hoffmann, A Simon, R Podschadlowski, and M Tischer. "NIR-FT-Raman-spectroscopy, state of the art." In: *Journal of molecular structure* 217 (1990), pp. 207–220.

[156] Ewen Smith and Geoffrey Dent. *Modern Raman spectroscopy: a practical approach*. John Wiley & Sons, 2019.

[157] Shin-ichiro Tamura. "Isotope scattering of dispersive phonons in Ge." In: *Physical Review B* 27.2 (1983), p. 858.

[158] B Abeles, DS Beers, G Dr Cody, and JP Dismukes. "Thermal conductivity of Ge-Si alloys at high temperatures." In: *Physical review* 125.1 (1962), p. 44.

[159] Nicholas W Lundgren, Giuseppe Barbalinardo, and Davide Donadio. "Mode localization and suppressed heat transport in amorphous alloys." In: *Physical Review B* 103.2 (2021), p. 024204.

[160] Jason M. Larkin and Alan J. H. McGaughey. "Predicting alloy vibrational mode properties using lattice dynamics calculations, molecular dynamics simulations, and the virtual crystal approximation." In: *J. Appl. Phys.* 114.2 (2013), p. 023507. DOI: 10.1063/1.4812737. eprint: https://doi.org/10.1063/1.4812737. URL: https://doi.org/10.1063/1.4812737.

[161] Alexander Stukowski. "Visualization and analysis of atomistic simulation data with OVITO–the Open Visualization Tool." In: *Modelling and simulation in materials science and engineering* 18.1 (2009), p. 015012. DOI: {10.1088/0965-0393/18/1/015012}.

[162] Hohyun Lee, Daryoosh Vashaee, D. Z. Wang, Mildred S. Dresselhaus, Z. F. Ren, and Gang Chen. "Effects of nanoscale porosity on thermoelectric properties of SiGe." In: *Journal of Applied Physics* 107.9 (May 2010), p. 094308. ISSN: 0021-8979, 1089-7550. DOI: 10.1063/1.3388076. URL: http://aip.scitation.org/doi/10.1063/1.3388076 (visited on 09/15/2021).

[163] Giri Joshi et al. "Enhanced Thermoelectric Figure-of-Merit in Nanostructured p-type Silicon Germanium Bulk Alloys." In: *Nano Lett.* 8.12 (2008), pp. 4670–4674. ISSN: 1530-6984, 1530-6992. DOI: 10.1021/nl8026795. URL: https://pubs.acs.org/doi/10.1021/nl8026795 (visited on 09/15/2021).

[164] G. H. Zhu et al. "Increased Phonon Scattering by Nanograins and Point Defects in Nanostructured Silicon with a Low Concentration of Germanium." In: *Phys. Rev. Lett.* 102.19 (May 2009), p. 196803. ISSN: 0031-9007, 1079-7114. DOI: 10.1103/PhysRevLett.102.196803. URL: https://link.aps.org/doi/10.1103/PhysRevLett.102.196803 (visited on 09/09/2021).

[165] G. Pernot et al. "Precise control of thermal conductivity at the nanoscale through individual phonon-scattering barriers." In: *Nature Mater* 9.6 (June 2010), pp. 491–495. ISSN: 1476-1122, 1476-4660. DOI: 10.1038/nmat2752. URL: http://www.nature.com/articles/nmat2752 (visited on 09/15/2021).

[166] Abhishek Chaudhuri, Anupam Kundu, Dibyendu Roy, Abhishek Dhar, Joel L. Lebowitz, and Herbert Spohn. "Heat transport and phonon localization in mass-disordered harmonic crystals." In: *Phys. Rev. B* 81 (6 2010), p. 064301. DOI: 10.1103/PhysRevB.81.064301. URL: https://link.aps.org/doi/10.1103/PhysRevB.81.064301.

[167] Walter Schirmacher, Matteo Paoluzzi, Felix Cosmin Mocanu, Dmytro Khomenko, Grzegorz Szamel, Francesco Zamponi, and Giancarlo Ruocco. "The nature of non-phononic excitations in disordered systems." In: *Nature Communications* 15.1 (2024), p. 3107.

[168] Simon Thebaud, Carlos A Polanco, Lucas Lindsay, and Tom Berlijn. "Success and breakdown of the T-matrix approximation for phonon-disorder scattering." In: *Physical Review B* 102.9 (2020), p. 094206.

[169] Claudio Buran, Marco G Pala, Marc Bescond, Mathieu Dubois, and Mireille Mouis. "Three-dimensional real-space simulation of surface roughness in silicon nanowire FETs." In: *IEEE Transactions on Electron Devices* 56.10 (2009), pp. 2186–2192. DOI: 10.1109/TED.2009.2028382.

[170] Cronin B Vining, William Laskow, Jack O Hanson, Roland R Van der Beck, and Paul D Gorsuch. "Thermoelectric properties of pressure-sintered Sio. 8Geo. 2 thermoelectric alloys." In: *Journal of applied physics* 69.8 (1991), pp. 4333–4340. DOI: 10.1063/1.348408. URL: https://doi.org/10.1063/1.348408.

[171] Erik Fransson, Mattias Slabanja, Paul Erhart, and Göran Wahnström. "Dynasor—a tool for extracting dynamical structure factors and current correlation functions from molecular dynamics simulations." In: *Advanced Theory and Simulations* 4.2 (2021), p. 2000240. DOI: https://doi.org/10.1002/adts.202000240. URL: https://onlinelibrary.wiley.com/doi/abs/10.1002/adts.202000240.

[172] Alfredo Fiorentino, Paolo Pegolo, and Enrico Drigo. *hydro_glasses*. Version 0.1. 2023. URL: https://github.com/afiorent/hydro_glasses.

[173] X Gonze and J Vigneron. "Density-Functional Approach to Nonlinear-Response Coefficients of Solids." In: *Phys. Rev. B* 39.18 (1989), pp. 13120–13128.

[174] A Debernardi A and S Baroni. "3rd-Order Density-Functional Perturbation Theory - a Practical Implementation with Applications to Anharmonic Couplings in Si." In: *Sol. St. Comm.* 91.10 (1994), pp. 813–816. DOI: 10.1016/0038-1098(94)90654-8.

[175] A Debernardi, S Baroni, and E Molinari. "Anharmonic Phonon Lifetimes in Semiconductors from Density-Functional Perturbation Theory." In: *Phys. Rev. Lett.* 75.9 (1995), pp. 1819–1822. DOI: 10.1103/PhysRevLett.75.1819.

[176] Paolo Giannozzi, Stefano Baroni, Nicola Bonini, Matteo Calandra, Roberto Car, Carlo Cavazzoni, Davide Ceresoli, Guido L Chiarotti, Matteo Cococcioni, Ismaila Dabo, et al. "QUANTUM ESPRESSO: a modular and open-source software project for quantum simulations of materials." In: *Journal of physics: Condensed matter* 21.39 (2009), p. 395502.

[177] Paolo Giannozzi, Oliviero Andreussi, Thomas Brumme, Oana Bunau, M Buongiorno Nardelli, Matteo Calandra, Roberto Car, Carlo Cavazzoni, Davide Ceresoli, Matteo Cococcioni, et al. "Advanced capabilities for materials modelling with Quantum ESPRESSO." In: *Journal of physics: Condensed matter* 29.46 (2017), p. 465901.

[178] Paolo Giannozzi, Oscar Baseggio, Pietro Bonfà, Davide Brunato, Roberto Car, Ivan Carnimeo, Carlo Cavazzoni, Stefano De Gironcoli, Pietro Delugas, Fabrizio Ferrari Ruffino, et al. "Quantum ESPRESSO toward the exascale." In: *The Journal of chemical physics* 152.15 (2020).

[179] Lorenzo Paulatto, Francesco Mauri, and Michele Lazzeri. "Anharmonic properties from a generalized third-order ab initio approach: Theory and applications to graphite and graphene." In: *Physical Review B* 87.21 (2013), p. 214303.

[180] Sergey A Khrapak and Gregor E Morfill. "Accurate freezing and melting equations for the Lennard-Jones system." In: *The Journal of chemical physics* 134.9 (2011).

[181] Roger W Hockney and James W Eastwood. *Computer simulation using particles*. crc Press, 2021.

[182] A. P. Thompson et al. "LAMMPS - a flexible simulation tool for particle-based materials modeling at the atomic, meso, and continuum scales." In: *Comp. Phys. Comm.* 271 (2022), p. 108171. DOI: 10.1016/j.cpc.2021.108171.

[183] P Vashishta, Rajiv K Kalia, José P Rino, and Ingvar Ebbsjö. "Interaction potential for SiO_2: A molecular-dynamics study of structural correlations." In: *Phys. Rev. B* 41.17 (1990), p. 12197. DOI: 10.1103/PhysRevB.41.12197.

[184] Loris Ercole, Aris Marcolongo, and Stefano Baroni. "Accurate thermal conductivities from optimally short molecular dynamics simulations." In: *Sci. Rep.* 7.1 (2017), pp. 1–11. DOI: 10.1038/s41598-017-15843-2.

[185] Loris Ercole. "Ab Initio Simulation of Heat Transport in Silica Glass." PhD thesis. SISSA, 2018.

[186] Priya Vashishta, Rajiv K Kalia, Aiichiro Nakano, and José Pedro Rino. "Interaction potential for silicon carbide: A molecular dynamics study of elastic constants and vibrational density of states for crystalline and amorphous silicon carbide." In: *J. Appl. Phys.* 101.10 (2007), p. 103515. DOI: 10.1063/1.2724570.

[187] José P Rino et al. "Short-and intermediate-range structural correlations in amorphous silicon carbide: A molecular dynamics study." In: *Phys. Rev. B* 70.4 (2004), p. 045207. DOI: 10.1103/PhysRevB.70.045207.

[188] Volker L Deringer et al. "Realistic atomistic structure of amorphous silicon from machine-learning-driven molecular dynamics." In: *J. Phys. Chem. Lett.* 9.11 (2018), pp. 2879–2885. DOI: 10.1021/acs.jpclett.8b00902.

[189] Zheyong Fan, Yanzhou Wang, Penghua Ying, Keke Song, Junjie Wang, Yong Wang, Zezhu Zeng, Ke Xu, Eric Lindgren, J Magnus Rahm, et al. "GPUMD: A package for constructing accurate machine-learned potentials and performing highly efficient atomistic simulations." In: *J. Chem. Phys.* 157.11 (2022), p. 114801. DOI: 10.1063/5.0106617.

[190] Zheyong Fan, Luiz Felipe C Pereira, Hui-Qiong Wang, Jin-Cheng Zheng, Davide Donadio, and Ari Harju. "Force and heat current formulas for many-body potentials in molecular dynamics simulations with applications to thermal conductivity calculations." In: *Phys. Rev. B* 92.9 (2015), p. 094301. DOI: 10.1103/PhysRevB.92.094301.

[191] Giovanni Bussi, Davide Donadio, and Michele Parrinello. "Canonical sampling through velocity rescaling." In: *J. Chem. Phys.* 126.1 (2007), p. 014101. DOI: 10.1063/1.2408420.

[192] Andrea Dal Corso, Stefano Baroni, Raffaele Resta, and Stefano de Gironcoli. "Ab initio calculation of phonon dispersions in II-VI semiconductors." In: *Physical Review B* 47.7 (1993), p. 3588.

[193] Hendrik J Monkhorst and James D Pack. "Special points for Brillouin-zone integrations." In: *Physical review B* 13.12 (1976), p. 5188.

ACKNOWLEDGMENTS

COLOPHON

This document was typeset using the typographical look-and-feel `classicthesis` developed by André Miede. Most of the graphics in this thesis are generated using the python package `matplotlib`. The bibliography is typeset using `biblatex`.

Final Version as of December 18, 2024 (`classicthesis` version 4.2).